IMPACT RESISTANCE OF FIBER COMPOSITE
BLADES USED IN AIRCRAFT TURBINE ENGINES

by

L. A. Friedrich
J. L. Preston, Jr.

APR 16 1974

PRATT & WHITNEY AIRCRAFT
DIVISION OF UNITED AIRCRAFT CORPORATION

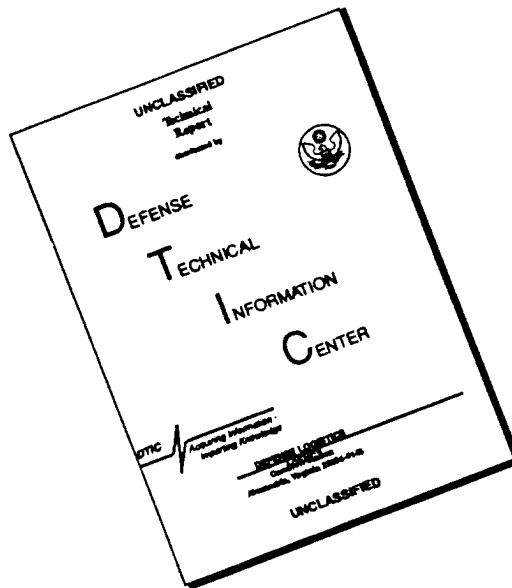Prepared for

NATIONAL AERONAUTICS AND SPACE ADMINISTRATION

NASA LEWIS RESEARCH CENTER

CONTRACT NAS 3-15568

19960418 094

DISCLAIMER NOTICE

THIS DOCUMENT IS BEST QUALITY AVAILABLE. THE COPY FURNISHED TO DTIC CONTAINED A SIGNIFICANT NUMBER OF PAGES WHICH DO NOT REPRODUCE LEGIBLY.

1. Report No. NASA CR - 134502	2. Government Accession No.	3. Recipient's Catalog No.
4. Title and Subtitle IMPACT RESISTANCE OF FIBER COMPOSITE BLADES USED IN AIRCRAFT TURBINE ENGINES		5. Report Date May 1973
		6. Performing Organization Code
7. Author(s) L. A. Friedrich J. L. Preston, Jr.		8. Performing Organization Report No. PWA^{TM}-4727
		10. Work Unit No.
9. Performing Organization Name and Address Pratt & Whitney Aircraft Division of United Aircraft Corporation East Hartford, Connecticut		11. Contract or Grant No. NAS3-15568
		13. Type of Report and Period Covered Contractor Report
12. Sponsoring Agency Name and Address National Aeronautics and Space Administration Washington, D. C. 20546		
		14. Sponsoring Agency Code

15. Supplementary Notes
Project Manager, Robert H. Johns, Materials and Structures Division NASA Lewis Research Center, Cleveland, Ohio

16. Abstract

Resistance of advanced fiber reinforced epoxy matrix composite materials to ballistic impact was investigated as a function of impacting projectile characteristics, and composite material properties. Ballistic impact damage due to normal impacts, was classified as transverse (stress wave delamination and splitting), penetrative, or structural (gross failure). Steel projectiles were found to be >gelatin >ice projectiles in causing penetrative damage leading to reduced tensile strength. Gelatin and ice projectiles caused either transverse or structural damage, depending upon projectile mass and velocity. Improved composite transverse tensile strength, use of dispersed ply lay-ups, and inclusion of PRD-49-1 or S-Glass fibers correlated with improved resistance of composite materials to transverse damage. In non-normal impacts against simulated blade shapes, the normal velocity component of the impact was used to correlate damage results with normal impact results. Stiffening the leading edge of simulated blade specimens led to reduced ballistic damage, while addition of a metallic leading edge provided nearly complete protection against 0.64 cm diameter steel, and 1.27 cm diameter ice and gelatin projectiles, and partial protection against 2.54 cm diameter projectiles of ice and gelatin.

17. Key Words (Suggested by Author(s)) Ballistic Impact Loadings, Composite Properties, Fiber Composite Blades, Impact Angle and Location, Ply Configuration, Projectile Characteristics	18. Distribution Statement Unclassified — Unlimited		
19. Security Classif. (of this report) Unclassified	20. Security Classif. (of this page) Unclassified	21. No. of Pages 150	22. Price* 3.00

FOREWORD

This report describes the work accomplished on contract NAS 3-15568 by the Pratt & Whitney Aircraft Division of United Aircraft Corporation for the Lewis Research Center of the National Aeronautics and Space Administration. The work was initiated 7 July 1971 and completed on 6 April 1973.

Robert H. Johns of the National Aeronautics and Space Administration Materials and Structures Division was Project Manager and Leonard W. Schopen, NASA Lewis Research Center, was the Contracting Officer.

Leonard A. Friedrich was the Pratt & Whitney Aircraft program manager and Mr. J. L. Preston, Jr. was the principal investigator. Mr. Richard Novak of the United Aircraft Research Laboratories prepared the flat panel impact specimens conducted, the mechanical property evaluation, and contributed to the analysis of the test results. Mr. E. H. Richards and Mr. L. A. Davis of P&WA conducted the ballistic testing. Dr. T. S. Cook of P&WA conducted the analytical effort and assisted in the analysis of the test results. Mr. H. I. Rulnick fabricated the simulated blade specimens and conducted the metallographic analysis. Mr. A. Janus was responsible for specimen instrumentation and the electronic data reduction described in the report. Mr. J. Graff of the Hamilton Standard Division of United Aircraft conducted the spin impact testing reported.

iii

TABLE OF CONTENTS

TABLE OF CONTENTS (Cont'd)

LIST OF ILLUSTRATIONS

LIST OF ILLUSTRATIONS (Cont'd)

LIST OF ILLUSTRATIONS (Cont'd)

LIST OF ILLUSTRATIONS (Cont'd)

LIST OF ILLUSTRATIONS (Cont'd)

LIST OF TABLES

LIST OF TABLES

I. SUMMARY

Impact damage due to normal impacts on flat panel specimens is characterized by transverse fractures (longitudinal in-plane cracking and interply delaminations) or by projectile penetration. Transverse damage, caused primarily by ice and gelatin projectiles, was most easily detected by ultrasonic C-scan inspection and by decreases in torsional natural frequency in multidirectionally reinforced composite laminates and by visual inspection of undirectionally reinforced laminates. The effect of transverse damage on the natural bending frequencies and residual tensile strength was not consistent. Penetration damage, caused by steel projectiles and gelatin projectiles impacting at velocities above 274 m/sec, caused measurable decreases in residual tensile strength and bending frequencies.

For a given impact energy level, steel projectiles > gelatin > ice in imparting impact damage as measured by the ability of the projectile to penetrate the composite and lower its residual tensile strength. High velocity 1.27 cm diameter ice and gelatin projectiles caused extensive delamination in multidirectionally reinforced specimens causing significant reduction in the torsional rigidity of the target specimens.

Tests using different fiber reinforcements indicated that increased composite transverse tensile strength was the most important factor in improving resistance to splitting and de-lamination type damage. Ranking of reinforcement fibers on this basis is: S-Glass > Boron > Modmor II graphite > T-75-S graphite > Modmor I graphite. Unidirectionally hybrid composites using T-75-S graphite fiber with addition of either PRD-49-1 or S-Glass exhibited impact resistance superior to T-75-S composite material.

The addition of angle plies to Modmor II graphite - epoxy laminates reduced the longitudinal cracking found in unidirectional laminates, but led to a greater incidence of delamination damage. Layups utilizing dispersed plies, including pseudo-isotropic and $[(0|+30|0|-30|0)_2]_s$, exhibited the greatest degree of impact resistance in tests using 1.27 cm ice at 274 m/sec.

Increased specimen thickness correlated with decreased impact damage, while volume fraction of fiber was not found to be a significant variable in the range tested.

Using cantilevered double tapered simulated fan blade specimens in impact testing with 1.27 cm diameter ice and gelatin projectiles demonstrated a correlation between increased damage and increased impact angle on graphite epoxy specimens. Altering the ply layup to stiffen the leading edge was found to reduce impact damage. Steel projectiles caused damage at all impact angles and locations tested.

Impact testing of specimens mounted in a whirling arm rig indicated damage similar to that caused by bench testing using a gas cannon. Metallic leading edge shields afforded protection to the graphite epoxy specimen in leading edge impacts with 0.64 cm diameter steel and 1.27 cm diameter ice and gelatin projectiles. The shields also provided substantial protection against 2.54 cm diameter ice projectiles impacting at a 30° angle to the leading edge while gelatin projectiles caused more severe damage.

1

The results of the ballistic analysis showed that the mechanical behavior of the projectile and the bending response of the target during impact are important variables effecting the degree of impact damage to composite materials. A method of damage classification is presented for normal impacts in Task I, and a means of relating this classification is presented for predicting types of damage resulting from non-normal ballistic impacts to Task II simulated blade specimens and to fan blades at typical operating conditions.

II. INTRODUCTION

The overall objective of this program is to provide the technology base needed for the design of polymeric matrix fiber reinforced composite turbine engine fan and compressor blades which will operate safely when subjected to impact by foreign objects. The micromechanical and macromechanical response of polymeric matrix composite specimens to ballistic impact loadings has been investigated initially under flat panel, normal impact conditions with various projectile materials (Task I). Extensive nondestructive and destructive testing has been used to characterize the nature and extent of damage and the resultant changes in mechanical properties. The response of simulated blade specimens to ballistic impact was then determined in an investigation of more complex configurational effects (Task II). Some of these tests were conducted using a rotating arm test rig. Evaluation after impact included both destructive and nondestructive techniques. Finally, an analytical effort was conducted to correlate all test results by developing a model for system response to impact and by analyzing the effect of damage on the strength and elastic properties of the remaining material (Task III).

The Modmor II graphite/PR-286 epoxy system received principal emphasis in this program. However, the Modmor I graphite/epoxy, T-75-S graphite/epoxy, boron/epoxy, S-glass/epoxy, PRD-49-1/epoxy, and Modmor II graphite/polyimide composite systems were also investigated.

The Task I flat panel investigation determined the effects of the following parameters on impact response:

- projectile characteristics,
- composite properties,
- ply configuration,
- fiber content,
- thickness, and
- constituent properties.

The Task II simulated blade specimen studies defined the following effects:

- stacking sequence, and fiber orientation,
- impact location and angle, projectile characteristics, and
- applied stress and protection schemes.

3

III. TEST PROGRAM

A. TASK I - COMPOSITE MATERIAL SCREENING

The objectives of Task I were to measure the relative impact behavior of several resin composite materials, and to relate the observed damage to the mechanical properties of the materials and to the characteristics of the impacting object.

1. Mechanical Property Characterization

The purpose of the mechanical property testing was to generate data which could be used in the program in analyzing the response of materials to ballistic impact loading. The data on unidirectional composites also served as a check on the quality of the material to ensure that acceptable minimum property levels were met. Shear, tensile, and Charpy impact properties were measured on unidirectional composites of each fiber/resin system. Multidirectional composites of the primary system, Modmor II/PR-286 graphite/epoxy were tested in tension and Charpy impact.

a. Unidirectional Laminate Testing

Test results for the 47, 55, and 65 volume percent Modmor II/PR-286, and the Modmor I/PR-286, T-75-S/PR-286, boron/PR-286, S-glass/PR-286, PRD-49-1/PR-286, S-glass + T-75-S/PR-286, and PRD-49-1 + T-75-S/PR-286 composites are summarized in Table I. Results for Modmor II/P13N polyimide composite system are listed in Table II. Figures 1 through 6 show representative stress-strain curves for longitudinal tension, transverse tension, and torsion of composites containing each fiber and fiber combination. Test specimens used in measuring the properties were as follows:

- Longitudinal tension: Straight-sided rectangular bar, 20.3 cm long x 0.635 cm wide x 0.127 cm thick (8.0 in. long x 0.25 in. wide x 0.05 in. thick); aluminum doublers bonded on each end.

- Transverse tension: Straight-sided rectangular bar, 10.2 cm long x 1.27 cm wide x 0.127 cm thick (4.0 in. long x 0.50 in. wide x 0.05 in. thick); no doublers.

- Beam shear: 1.27 cm long x 0.635 cm wide x 0.254 cm thick (0.50 in. long x 0.25 in. wide x 0.10 in. thick); span-to-depth ratio of 4:1.

- Charpy impact: Square bar 1.0 cm x 1.0 cm x 5.5 cm (0.394 in. x 0.394 in. x 2.165 in.) with a 45° V-notch.

- Torsion rod shear: 0.635 cm dia. x 3.82 cm long (0.25 in. dia. x 1.50 in. long) rod.

The hybrid S-glass plus T-75-S/PR-286 and PRD-49-1 plus T-75-S/PR-286 laminates were designed to have an equivalent longitudinal modulus and superior impact resistance to unidirectional Modmor II/PR-286 composite. The data in Table I indicates that these goals were achieved, and that inclusion of the S-glass into the T-75-S laminates yields a significant

4

improvement in the notched Charpy impact strength over the inclusion of PRD-49-1. Average notched Charpy impact strengths of the S-glass + T-75-S/PR-286 and PRD-49-1 + T-75-S/PR-286 laminates are 17.0 joules (12.5 ft-lbs), and 11.2 joules (8.2 ft-lbs), respectively, compared to 8.8 joules (6.5 ft-lbs) for the Modmor II/PR-286. The S-glass + T-75-S/PR-286 laminate also exhibits higher longitudinal and transverse tensile properties than the PRD-49-1 + T-75-S/PR-286 laminates.

Typical longitudinal tensile stress-strain curves are plotted in Figures 1 and 2 for unidirectional composites. The Modmor I/PR-286, S-glass + T-75-S/PR-286, T-75-S/PR-286, and boron/PR-286 systems display linear elastic behavior to fracture, while the S-glass/PR-286, PRD-49-1/PR-286, and the T-75-S + PRD-49-1/PR-286 systems exhibit initial linear behavior followed by nonlinear behavior prior to failure. The nonlinear behavior of the T-75-S + PRD-49-1/PR-286 is probably a result of fracture of the strain-limited T-75-S fiber prior to specimen ultimate failure.

Typical transverse tensile stress-strain curves are shown in Figures 3 and 4 for unidirectional composites. The 55 percent and 65 percent Modmor II, Modmor I, T-75-S, S-glass + T-75-S and PRD-49-1 reinforced PR-286 epoxy composites and the Modmor II/P13N polyimide composite system are all linear to failure. The 47 percent Modmor II, boron, S-glass and T-75-S + PRD-49-1 reinforced PR-286 epoxy composites are initially linear but show nonlinear behavior prior to failure. The addition of the T-75-S graphite to the S-glass reduces both the modulus and the ultimate strain in transverse tension, as seen in Figure 4.

Typical torsion rod torque versus shear-strain curves are shown in Figures 5 and 6 for unidirectionally reinforced composites. Except for the Modmor II/P13N composite system, all curves show yielding prior to fracture. Ultimate shear strains vary from approximately 0.90 percent in Modmor II/P13N to 5 percent in S-glass/PR-286. The Modmor II composite containing PR-286 epoxy resin exhibits twice the ultimate shear strain of the Modmor II composite containing P13N polyimide resin.

b.   Multidirectional Laminates Testing

Test results from multidirectional Modmor II/PR-286 laminates are presented in Table III. The results for the ±45, 0, ±45 and ±30, 0, ±30 laminates are within the expected range based upon the all-unidirectional, ±45, and ±30 results obtained. Longitudinal notched Charpy impact testing shows that the pure ±45 and ±30 angle-ply laminates have superior impact strengths compared to the multidirectional laminates containing the same angle-plies reinforced with unidirectional layers.

2.   Impact Specimen Testing and Evaluation

The impact specimen utilized in Task I consisted of a 5.1 cm x 23 cm x 0.25 (2 inch x 9 inch x 0.1 inch) flat plate gripped at one end and impacted normally at midchord, 11.4 cm (4.5 inch) from the gripped end. Projectiles consisted of 1 and 8 gram spheres of ice, steel, and gelatin, while composite variables consisted of fiber type, ply configuration, fiber content, and specimen thickness. Evaluation of impact damage consisted of visual and ultrasonic inspection, frequency determinations, residual tensile strength determinations, and selected holographic, metallographic and scanning electron microscope examinations.

5

Impact damage due to the normal impacts conducted in Task I can be characterized as transverse failures (longitudinal in-plane cracking and interlaminar delaminations) or longitudinal failures (penetration and fiber breakage). Transverse damage, caused predominantly by the ice and gelatin projectiles, was most easily detectable by ultrasonic C-scan, holography, and first torsional frequency determinations in multidirectionally reinforced composite laminates, and by visual inspection in cases of splitting of unidirectionally reinforced composite laminates. The effect of transverse damage upon longitudinal bending frequencies and residual tensile strength was scattered. Penetration and fiber damage, caused chiefly by steel impacts and by gelatin impacts above 274 m/sec (900 ft/sec) had the greatest effect upon the residual tensile strength and bending frequencies of the specimens.

For a given impact energy level, the steel > gelatin > ice in impact damage severity as measured by the ability of the projectile to penetrate the composite and lower its residual tensile strength. High velocity 1.27 cm diameter ice and gelatin impacts caused extensive delaminations in multidirectionally reinforced specimens causing significant reductions in torsional rigidity. The 2.54 cm (8 gram) ice and gelatin impacts caused structural failure of specimens at a velocity of 152 m/sec (500 ft/sec).

Tests using a variety of fiber reinforcements indicated that increased composite transverse tensile strength was the most important factor in improved resistance to splitting and delamination damage caused by high speed 1.27 cm (0.5 inch) diameter ice impacts, where penetration is not a factor. Ranking of fibers on this basis is: S-Glass > Boron > Modmor II > T-75-S and Modmor I. The PRD-49-1 reinforced laminates, with the lowest transverse strength, exhibited a greater tendency towards localization of damage about the impacted region through multiple cracking and indentation, and were superior to Modmor II in unidirectionally reinforced specimens but inferior in multidirectional layups. Unidirectional composites made using T-75-S plus either PRD-49-1 or S-Glass exhibited impact resistance between that of pure T-75-S and Modmor II.

The composite variables of ply configuration, fiber content, and specimen thickness were investigated using Modmor II/PR-286, graphite epoxy impacted with 1.27 cm (0.5 inch) ice at 274 m/sec (900 ft/sec). The presence of angle-plies in the layup reduced the longitudinal cracking found in unidirectional composites, but promoted delamination, especially in the $[(\pm 45)_2 \mid 0_{12} \mid (\mp 45)_2]_T$ "core-and shell" type laminates. Layups utilizing dispersed plies, such as pseudo-isotropic and $[(0 \mid +30 \mid 0 \mid -30 \mid 0)_2]_S$ exhibited the best impact resistance, showing little or no damage. Increased thickness correlated with decreased impact damage, and volume fraction fiber was not found to be a significant variable.

a. **Part A "Effect of Projectile Characteristics"**

Ballistic impact testing of the 36 test specimens in Task I, Part A "Effects of Projectile Characteristics", was conducted with spherical steel, ice, and gelatin projectiles, using two different masses of each (approximately 1 gram and 8 grams), at three velocity levels. The test conditions are summarized as follows:

Projectile Type	Diameter (cm)	Average Mass (g)	Velocities (m/sec)		
			V_1	V_2	V_3
Steel	0.64	1.06	61	91	122
	1.19	6.88	31	61	91
Ice	1.27	0.98	213	274	305
	2.54	7.95	61	107	152
Gelatin	1.27	1.08	152	213	274
	2.54	8.62	61	107	152

The velocities were selected to provide a wide range of specimen damage within each projectile/mass combination in order to provide both damage threshold and structural failure energy levels. All specimens were Modmor II/PR-286 graphite-epoxy composite constructed in a $[(\pm 45)_2 | 0_{12} | (\mp 45)_2]_T$ simulated blade layup.

Impact parameters plus visual and ultrasonic inspection results of the Task I Part A testing are shown in Table IV. The ultrasonic through transmission results are tabulated as percent of specimen area exhibiting less than 20 percent transmission of signal. This is an indication of the extent of ply separation and delamination damage to the specimen. The results of the specimen examinations are discussed in more detail below.

Damage due to steel impacts was detected at the lowest energy levels of the three projectile types. Visual damage on both front and back faces was visible at an impact velocity of 51.5 m/sec (1.4 joules of impact energy) with the 0.64 cm (0.25 inch) diameter steel and a velocity of 24 m/sec (2.0 joules of impact energy) using the 1.19 cm (0.47 inch) diameter steel. Increasing impact velocity with the 0.64 cm diameter steel resulted in increasing depth of penetration, with no widening of the impact-damaged zone. The extent of the damaged area, as determined using ultrasonic through transmission, revealed no trend with increasing impact velocity, averaging 6 percent for all six tests. Near penetration of the Modmor II/PR-286 specimens was achieved in three instances, at 95.4 m/sec (4.8 joules of impact energy), 122 m/sec (7.9 joules) and 130 m/sec (9.0 joules). Front and back views of a nearly penetrated specimen are shown in Figure 7.

Increasing the velocity of the 1.19 cm (0.47 inch) diameter steel projectiles resulted in both increased depth of penetration and more widespread damage. The extent of the damaged area determined by ultrasonic through transmission increased sharply from 3 to 5 percent at impact velocities of 24 to 33 m/sec (2.0 to 3.7 joules of impact energy) to between 17 and 37 percent at velocities ranging from 59 to 100 m/sec (12.0 to 34.2 joules), where either penetration or near penetration had occurred. This increased damage is visible as extensive lifting and delamination in the specimen back face. These delaminated plies closed back over the hole left by the 1.19 cm steel projectiles after penetration at the two highest velocities of 82 m/sec and 100 m/sec (23.0 and 34.2 joules).

Ice impacts caused the least visible damage to the specimens and required the highest impact energies to produce detectable damage either visibly or ultrasonically. Specimens impacted

with 1.27 cm (0.5 inch) diameter ice revealed no visible damage at velocities of 213 m/sec and 226 m/sec (21.3 joules and 25.2 joules of impact energy), and no visible damage to the front impacted faces up to the highest velocity of 317 m/sec (49.7 joules). Single delamination planes were visible in two specimens along the edges after being impacted at 274 m/sec and 317 m/sec (37.1 joules and 49.7 joules). These delaminations were located in the back face ±45° plies at or near the interface between these plies and the unidirectional plies. The locations of these delaminations at the edges coincide well with the areas of these specimens transmitting less than 20 percent during the post-test ultrasonic inspections. Thus the ultrasonic technique is a good indication of internal delaminations located within the other specimens impacted with the 1.27 cm diameter ice. The extent of damage determined by ultrasonic inspection for these specimens varies from 0 percent at 226 m/sec (25.6 joules) and 7 percent at 213 m/sec (21.3 joules) to 31 percent at 317 m/sec (49.7 joules). In general, the extent of these delaminated areas (as determined ultrasonically) progressed more in the specimen longitudinal direction than in the widthwise direction. The delaminations are most likely caused by shock waves reflected as tensile waves from the free back surface of the specimen.

Specimens impacted with the 2.54 cm (1 inch) diameter ice exhibited no damage visibly or ultrasonically at velocities from 64 m/sec to 111 m/sec (16.1 joules to 49.2 joules of impact energy). A specimen impacted at 145 m/sec (83.3 joules) fractured behind the point of impact, with both pieces revealing multiple delaminations in the unidirectional and ±45° crossplies. The specimen impacted at 154 m/sec (94.6 joules) did not fracture but did lose the tip segment of its back face ±45° plies and revealed similar multiple delamination planes in the unidirectional and ±45° crossplies. Ultrasonic inspection of these specimens revealed 74 and 100 percent, respectively, of the total specimen area to be damaged. Significantly, both damaged specimens revealed signs of penetration by the ice in the form of cracking at the point of impact on the front face and fractured unidirectional plies visible behind the point of impact on the back faces. The overall delamination of these specimens appears to be a flexural failure where the interlaminar shear strength of the material was exceeded due to the bending imposed by the impact. Consequently, the thickness and strength of the impacted beam could be an important factor in determining the extent of delamination damage in these cases.

Ballistic impacts with gelatin projectiles caused damage similar to that observed with ice, but the damage levels at a given impact energy were more severe. Impacts with 1.27 cm (0.5 inch) diameter gelatin caused no damage detectable either visually or ultrasonically up to 166 m/sec (14.9 joules of impact energy). Impacts on three specimens at velocities between 208 m/sec and 274 m/sec (23.4 joules to 38.3 joules) caused delamination in the back face ±45° plies visible along the specimen edges at or near the interface with the unidirectional plies. The specimen impacted at 283 m/sec (43.2 joules) revealed signs of penetration: broken fibers, cracks, and delaminations in both front and back faces, with split and fractured unidirectional plies visible and slightly protruding at the back face.

Specimens impacted with 2.54 cm (1 inch) diameter gelatin revealed no detectable damage at velocities of 64 to 68 m/sec (17.5 to 19.9 joules of impact energy). At 107 m/sec (49 joules) the specimen revealed damage over 89 percent of its area as a delamination in the unidirectional plies. At velocities of 147 m/sec and 154 m/sec (93.4 and 104 joules) the specimens exhibited complete flexural failure, with both specimens exhibiting multiple delaminations, and one fracturing completely. The large deflections imposed upon a test speci-

8

men can be seen in the third frame of Figure 8, which shows a high speed strobe photograph of specimen 1025-1 being impacted by a 2.54 cm diameter gelatin ball at 154 m/sec.

Steel, with the highest stiffness and strength of the three projectile types, does not deform appreciably during the impact with the relatively soft composite material. This results in very high impact pressures being generated over a small contact area even at relatively low impact velocities, with the result that the damage threshold for steel impacts (<1.4 joules for 0.64 cm diameter, and <2 joules for 1.19 cm diameter) is lower by more than an order of magnitude than that for the ice (21-25 joules for 1.27 cm diameter, >49 joules for 2.54 cm diameter) and gelatin (>15 joules for 1.27 cm diameter, >20 joules for 2.54 cm diameter). A second effect is that the steel projectiles require relatively low energies to penetrate the composite. The 1.19 cm (0.47 inch) diameter steel penetrates the Modmor II/PR-286 composite at an impact energy of only 23 joules which corresponds approximately to the damage threshold levels for the 1.27 cm (0.50 inch) diameter ice and gelatin projectiles.

The lower modulus, low strength ice and gelatin projectiles distribute their impact energies over a larger area, thereby causing less local deformation or specimen penetration. Ice, which fractures into a spray of crystals upon contact, showed no tendency towards penetration at velocities up to 317 m/sec with the 1.27 cm diameter projectiles, and limited penetration only at 145 and 154 m/sec with the more massive 2.54 cm diameter projectiles. A high speed strobe photograph sequence of three separate 2.54 cm diameter ice ball shots (Figure 9) reveals the break up of the ice ball upon contact with the trial specimen. The initial photograph reveals the intact ice ball followed immediately by the hollow plastic sabot, but some spray and the presence of a flat spot on the ice ball indicates probable weight loss prior to the impact. The second photograph reveals partial shattering of the ice ball at the point of contact with the trial specimen, with part of the ball still intact and visible just ahead of the sabot. Blurring of the trial specimen tip indicates that sufficient time has elapsed for specimen structural response to occur. In the last photograph a fully fragmented ice ball is shown. The somewhat lower damage extents noted for the ice ball impacts in comparison to gelatin impacts at approximately the same energy level may be a result of weight loss of the ice balls prior to impact. Present precautions to minimize this problem include packing the loading end of the barrel in dry ice prior to shooting. Another potential problem was revealed during several strobe photographs of trial 1.27 cm diameter ice shots, when one photograph revealed that the ice ball had broken into two segments prior to impact. As a result of this, subsequent test specimens to be impacted with the 1.27 cm diameter ice were sprayed with a blue lacquer which erodes from the specimen upon impact by the ice. Examination of the spray pattern thus produced indicates the condition of the ice ball at the time of impact.

Gelatin, with the lowest elastic modulus of the three projectiles, deforms elastically upon impact and shows no tendency toward penetration at velocities up to 274 m/sec. (Perfectly spherical 1.27 cm diameter gelatin projectiles have been found intact after rebounding off test specimens at velocities up to 213 m/sec.) The 1.27 cm diameter projectile at 283 m/sec did show partial penetration. At the higher velocities the impact strain rates will begin to exceed the viscoelastic relaxation times of the gelatin material with the result that the effective modulus of the material upon impact is much greater than the modulus determined via ordinary mechanical testing at low strain rates.

The specimen failures caused by the 2.54 cm (1 inch) diameter ice (at 83-95 joules) and gela-
tin (93-104 joules) appear to have resulted more from a structural overloading of the test
specimen in bending (Figure 8), rather than localized impact damage. Stronger test specimens
able to absorb the projectile momentum could possibly have survived structurally with only
some localized damage at the point of impact.

b. Part B "Effect of Composite Properties"

The visual and ultrasonic inspection results of the Task I, Part B "Effect of Composite Prop-
erties" is presented in Table V. All specimens were impacted with 1.27 cm (½ inch) diameter
ice at approximately 274 m/sec (900 ft/sec), with impact energies from 32.6 to 43.4 joules.
The primary variable investigated in this part of Task I was the effect of different fiber rein-
forcements upon the ballistic impact resistance of both unidirectional and multidirectional
laminates. The results of this testing revealed significant differences due to fiber reinforce-
ments. High notched Charpy impact strengths and high transverse tensile strengths were
both found to correlate with improved impact resistance for both unidirectionally and multi-
directionally reinforced composites. The unidirectionally reinforced boron and S-glass lami-
nates were superior to all graphite specimens tested. The multidirectionally reinforced com-
posites revealed less damage than the unidirectionally reinforced composites utilizing the
same fiber, with the multidirectional S-glass laminate revealing no visible damage. The mono-
lithic titanium-6Al-4V specimens revealed no visual or ultrasonic damage.

The unidirectionally reinforced laminates revealed three types of damage: longitudinal in-
plane cracking and splitting; interlaminar delaminations; and local yielding and depression at
the point of impact. The high-modulus Modmor I and Thornel-75-S composites (Charpy im-
pact energies of 3.5 joules and 4.1 joules, respectively) split longitudinally in two or more
segments revealed interlaminar delaminations, and exhibited additional cracks plus depression
of the impacted area. The extent of damage was 42 percent for the Modmor I/PR-286 and
32 percent for the Thornel-75-S/PR-286. The Modmor II/PR-286 (8.8 joules Charpy) was
also split, but revealed no interlaminar delaminations and had only 16 percent extent of dam-
age. The Modmor II/P13N (8.7 joules Charpy) did not split, but revealed a 49 percent extent
of damage. The PRD-49-1/PR-286 specimen (17.6 joules Charpy) revealed longitudinal crack-
ing and depression of the impact point. The damaged area covered 10 percent of the specimen
area and was more localized about the point of impact than any of the other unidirectional
specimens. Impact damage to the boron and S-glass specimens (11.5 joules and 47.5 joules
Charpy impact strength) was minimal and consisted only of a single longitudinal in-plane crack
in each. Ultrasonic inspection, which is generally insensitive to in-plane cracking, revealed
only 1.2 percent damaged area on the boron/PR-286 and 0.6 percent in the S-glass/PR-286.

These tests demonstrate the weakness of the all-unidirectional graphite/resin matrix composites
in the transverse direction. The fractures observed in the graphite reinforced specimens are
predominantly longitudinal (interlaminar or in-plane) with few filament fractures, and are
therefore occurring either in the matrix or at the fiber-matrix interface. Examination of the
transverse tensile strengths of the unidirectionally reinforced laminates reveals the highest
strengths in the S-glass and boron laminates, which suffered the least impact damage. These
strengths are 94.6 MN/m^2 (13.0 ksi) for S-glass and 56.8 MN/m^2 (8.25 ksi) for boron.

The PRD-49-1/PR-286 laminate, which revealed more damage than expected based upon Charpy impact considerations alone, had the lowest transverse tensile strength, 21.0 MN/m² (3.05 ksi) of any of the specimens tested. Since all but one of the tested specimens utilized the same PR-286 epoxy matrix, it is evident that the strength of the fiber-matrix interface is an important factor in determining ballistic impact damage.

In multidirectionally reinforced "core-and-shell" type impact specimens, the PRD-49-1 laminates revealed indentation at the impacted face plus internal delamination which was similar to that observed in several Modmor II/PR-286 laminates in Task I, Part A. These delaminations were visible when the specimens were viewed from the back face, and where they intersected the free edges they corresponded with edge cracks which were visible at the interface between the back face ±45° plies and unidirectional core plies. The previously discussed low transverse strength of the PRD-49-1 laminates renders them easily fractured by reflected tensile waves off the free back face, and further shows the importance of the 90° strength during impact. The boron reinforced specimens revealed some fiber fracture and lifting of the back face ±45° plies, and the S-glass reinforced laminates revealed no damage. Both of these materials exhibited superior impact in the unidirectional layup as well.

c.   Part C "Effect of Ply Configuration, Fiber Content, and Thickness"

The testing in Part C was aimed at defining the effects of fiber content, composite thickness, and ply orientation on impact behavior. All testing was conducted using specimens fabricated of Modmor II/PR-286 composite, and all specimens were impacted with 1.27 cm (½ inch) diameter ice balls at approximately 274 m/sec (900 ft/sec).

(1)   Fiber Content - The visual and ultrasonic inspection results from the 47 and 65 volume percent unidirectional Modmor II/PR-286 specimens are described in Table V. Based upon these results, variation in fiber content does not alter the ballistic impact response greatly. Both of the 47 volume percent and the 65 volume percent specimens remained intact after impact, and all exhibited one major longitudinal in-plane crack. Extent of damage varied from 1.1 percent with the two 47 volume percent specimens and one of the 65 volume percent specimens to 16 percent for the second 65 volume percent specimen. These specimens, in general, reveal less damage than the single 57 volume percent specimen tested in Task I, Part B, which was split into two segments in addition to showing a 16 volume percent extent of damage.

(2)   Ply Configuration - The visual and ultrasonic inspection results of tests to determine effects of ply configuration and specimen thickness are also presented in Table VI. Impact of the multidirectionally reinforced specimens is characterized by lack of damage to the impacted face, and prevention of longitudinal cracking and splitting evident in the unidirectionally reinforced specimens. Damage instead appears as cracks and delaminations visible at either the back face or edges, and appears to be caused by shock wave propagation within the specimen. The specific ply configurations investigated consist of all angle-ply (±30° and ±45°), "core-and-shell" designs utilizing a unidirectional core with both ±30° shells and ±45° shells, and two dispersed ply designs, $[(0 | +30 | 0 | -30 | 0)_2]_S$ and "pseudo-isotropic" $[(\pm72 | \pm36 | 0)_2]_S$.

11

Comparison of the ±30° angle-ply to the ±45° angle-ply revealed significantly less damage in the ±45° specimens. The ±30° specimens revealed visual cracking damage at the back face, and damage extents of 12.5 percent and 16 percent, while the ±45° specimens revealed no visual damage and damage extents of 0.5 percent and 0 percent. (The condition of the ice ball was questionable on the first ±45° shot, however.)

Comparison of the two core-and-shell layups is uncertain due to the questionable condition of the ice balls in three out of four tests, including both specimens utilizing the ±30° shell plies. Both layups exhibited low damage extents (from 1.4 percent to 4.8 percent) and little or no visual damage in impacts with fragmented ice balls, while the ±45° core-and-shell layup impacted with an intact ice ball revealed a 30 percent extent of damage. Two other ±45° core-and-shell layups impacted in Task I, Part A, revealed damage extents of 9 percent and 20 percent when impacted at 274 m/sec (900 ft/sec) with 1.27 cm diameter ice. A comparison of damage levels between the ±45° angle-ply and ±45° core-and-shell layups does indicate that the abrupt change in the ply angle between the unidirectional core and the ±45° shell may serve as a site for shock-induced damage. Shear stresses already exist at the interface between the 0° plies and the ±45° plies due to differential thermal contraction of these plies upon cooling from fabrication temperatures. Visual inspection of Task I, Part A, core-and-shell specimens revealed delaminations predominantly at or near the interface between the back face ±45° plies and the unidirectional plies.

Examination of the dispersed ply test specimens indicated that these layups were successful in resisting impact damage. None of the [(0| +30| -30|0)$_2$]$_s$ laminates or pseudo-isotropic laminates revealed any visual damage, and damage extents varied from 0 percent to 1 percent. The dispersed 0°, 30° specimens revealed less damage than either the ±30° angle-ply or core-and-shell layups. This indicates that ply dispersion is a possible means of reducing shock wave damage in laminates where 0° plies are necessary for axial properties.

Two ±45° core-and-shell layups of double thickness impacted to determine effects of thickness upon impact damage revealed somewhat lower damage levels than the normal thickness specimens of identical layup. The test utilizing an intact ice ball caused a 4.2 percent extent of damage with no visual damage. This specimen has been examined metallographically and the ultrasonic indications attributed to internal cracking caused by the ice ball impact. A second specimen impacted with a fragmented ice ball revealed no damage.

d.   Part D "Materials Impact Improvement Evaluation"

The results of the visual and ultrasonic inspections of the specimens impacted in the "Materials Impact Improvement Evaluation" section are described in Table VII. All specimens in this evaluation were impacted using 1.27 cm (½ inch) diameter ice at approximately 274 m/sec (900 ft/sec), in the same manner as the specimens tested in Task I, Parts B and C. The objective in Part D was to evaluate the ballistic impact resistance of hybrid graphite composites made with improved Charpy impact strengths by including high strength, low modulus fibers. The objective in fabrication was to achieve a composite with stiffness comparable to the lower modulus graphite laminates, but with superior impact resistance. The graphite fiber selected was the T-75-S, which exhibited the highest longitudinal tensile modulus plus poor impact resistance in unidirectionally reinforced Charpy and ice ball impact tests. The S-glass and PRD-

12

49-1 fibers were utilized to increase the impact resistance of the T-75-S graphite. Inclusion of these fibers resulted in increases in the notched Charpy impact strength as previously discussed. Comparison of damage levels in the five unidirectional hybrid impact specimens revealed measurable improvement in the impact resistance compared with damage levels in the two unidirectional T-75-S specimens in Task I, Part B. Inclusion of the PRD-49-1 reduced the incidence of longitudinal splitting, and reduced damage extents to a range of 2.9 percent to 29 percent compared to 32 percent and 49 percent in the T-75-S specimens. Use of the S-glass resulted in further reduction of damage extents to 10 percent and 22 percent (questionable ice ball), and eliminated the longitudinal splitting. The damage extents in the impacted hybrid specimens were generally higher than those of the unidirectional Modmor II/PR-286 specimens in Task I, Parts B and C, and testing of multidirectionally reinforced hybrid specimens would be necessary to determine the true value of these composites in resisting ballistic impact damage.

e.   Instrumented Specimen Testing

The response during the impact event of a number of specimens described in the preceding sections was monitored utilizing an array of 8 to 10 dynamic strain gages. The positioning of the gages is shown in Figure 10.

The strain recording system utilizes Micro-Measurements EA-06-125AC-350 strain gages inserted into potentiometric bridge circuits, strain gage translator operational amplifiers, and a 12-channel Precision Instrument PI 2100 recorder which operates at 60 ips in the direct mode. Frequency response of this overall system is 300 Hz to 50 kHz (±3 db), being limited at the low end by the recorder and at the high end by the operational amplifiers in the strain gage translator. Square wave tests with the 50 kHz direct mode system indicate a rise time capability of approximately 5 μsec and appears to be adequate for testing requirements.

Data reduction was conducted through oscilloscope photography of tape playbacks. This method, though time consuming, was selected because of the superior accuracy, signal-to-noise ratio and flexibility compared to oscillograph playback. The oscilloscope, with 1 MHz frequency response, has a rise time of less than 1 μsec, and use of varying time expansion on the same channel yields information on both long term bending response and short time shock pulses. The standard procedure consisted of: (1) photographing each channel at 2000 μsec/cm sweep rate to determine reliability of the gages after the impact and to assure that the proper vertical sensitivity was being used; and (2) photographing each channel at a sweep rate of 20 to 50 μsec/cm to measure rise time, amplitude, and pulse width of the initial pulse after proper vertical sensitivity has been determined from the first photograph.

Comparisons of the electronic data system accuracy as a function of limiting frequency response are shown in Figure 11. This data was collected by measuring the response of one selected channel from each specimen using an on-line oscilloscope, in addition to the conventional playback techniques. Oscilloscope measurements at 1000 kHz limiting frequency were determined by photographing the impact strain signal time history directly from the strain gage bridge, prior to its passage through any operational amplifier. The second channel of the dual-beam scope measured the same gage response directly after passing through the strain gage translator operational amplifier, which is limited to 50 kHz. As an additional check, the oscilloscope photographs of tape playbacks were compared to the on-line re-

sults to evaluate the alignment and calibrations of the tape recorder. Figure 11 shows two on-line comparisons, with the 1000 kHz traces on the top, and the 50 kHz traces on the bottom. The photograph at the left shows the strain history of channel 3 on specimen 984-4, which revealed the fastest initial rise time recorded on an on-line scope after being impacted with 1.27 cm diameter gelatin at 161 m/sec. Visual inspection of the two traces reveals excellent comparison, and measurement of the initial compressive peak (rise time of approximately 5 μsec) reveals an attenuation of 9 percent in the 50 kHz peak compared to the 1000 kHz peak. The photograph at the right shows the strain history of channel 1 on specimen 982-2, which was impacted with 2.54 cm diameter gelatin at 68 m/sec. Visual comparison of the 1000 kHz and 50 kHz traces again reveals excellent agreement. Comparison of the amplitude of the first small peak (200 μsec from point of impact) reveals a 7 percent amplification of the 50 kHz peak compared to the 1000 kHz peak. The initial peak strain results are presented in Tables VIII and IX.

Data reduction was taken from oscilloscope playbacks of the tape records at time expansions of 2000 μsec/cm (to determine bending response) and 10 to 50 μsec/cm (to determine initial peak amplitudes). All impacts were with 1.27 cm (0.5 inch) diameter ice at approximately 274 m/sec (900 ft/sec).

These strain histories revealed:

- An initial strain pulse, usually compressive with a fast rise time. The highest absolute strain was usually achieved during this or the pulse immediately following.

- An intermediate period (2000 to 4000 μsec) during which superpositions of several high frequency oscillations were visible. The highest peak strain was occasionally achieved during this time.

- A decay period during which the second bending response alone persisted and decayed. The first bending response was also visible in specimens where the first bending frequency is $\geqslant$ 100 Hz. (This is due to the fact that the 300 Hz to 50 KHz tape system does have some response down to this frequency.)

Examination of the tabulated peak strain results in Table IX reveals higher maximum strain in the unidirectionally reinforced specimens. Maximum strains ranged up to 1.48 percent in the case of unidirectional S-glass/PR-286, and strains in excess of 1.0 percent were measured in unidirectional laminates reinforced with PRD-49-1, Modmor II, Modmor I, T-75-S, and PRD-49-1 + T-75-S. None of the multidirectionally reinforced laminates from Task I, Part C, exhibited strain levels in excess of 1.0 percent with the highest recorded strain of 0.784 percent occurring at gage No. 7 in the $[(0| +30| 0| -30|0_2]_s$ Modmor II/PR-286 specimen. These multidirectionally reinforced specimens in general exhibited lower damage extents than the unidirectionally reinforced specimens in Parts B and D. Among the unidirectional specimens in Part B there is no clear correlation between maximum strain level and extent of damage as the maximum strain of 1.48 percent occurs in the S-glass laminate which revealed only 0.1 percent extent of damage. A standard titanium reference specimen was also impacted with the 1.27 cm diameter ice and exhibited peak strains of from 0.303 percent to 0.553 percent.

14

f.   Holographic Inspection

Holographic inspection was found to be a useful technique for the determination of the extent of impact damage in the $[(\pm 45)_2 |0_{1\,2} |(\mp 45)_2]_T$ Modmor II/PR-286 specimens investigated. Comparison of damage extents determined ultrasonically and holographically are in good agreement except in two specimens where the severity of the damage interfered with the holographic measurements. The standing wave technique was found to be the most convenient for determining holographic damage extent, because the entire damaged area is visible in a single reconstruction.

Specimens with minimal visual damage and known ultrasonic indications, such as low velocity steel impacts and 1.27 cm diameter ice and gelatin impacts, were selected for holographic inspection. In this way, the holographic damage extents could be checked against ultrasonic C-scans of the same identical specimens in cases where visual inspections alone would be inadequate. Ultrasonic damage extents varied from 0 percent to 52 percent on the specimens inspected via holography. Good agreement was found between the two methods, with the holographic damage extents consistently revealing from 0.5 percent to 3 percent smaller damage extents than the ultrasonic C-scan except for two specimens which were severely damaged by 1.27 cm diameter gelatin impacts at velocities $\geqslant 274$ m/sec (900 ft/sec). It appears that the damage in these specimens interfered with the establishment of a standing wave pattern on the specimen surface, such that only damage on the side of the impact nearest the excitation transducer was visible. This problem could be rectified by making a second hologram with the transducer placed at the opposite side of the impacted specimen.

Two holographic techniques were utilized during the inspection. Both techniques utilized a 50 KHz transducer to excite a point on the specimen impacted face. In the propagating wave technique, the hologram is taken of the specimen back face within 30 to 80 microseconds of the time when the 50 KHz transducer is triggered. The holographic reconstruction then reveals the concentric light-and-dark rings of the first several wave fronts propagating from the point of excitation. Since the wave propagation velocity is proportional to the square root of the section thickness, delaminations occurring near the back face cause retardation of the propagating wave fronts. This retardation disrupts the concentric ring pattern and indicates the boundary of the defective area. In the case where the probable location of the delamination plane is known relative to the specimen thickness, as in the 1.27 cm ($\frac{1}{2}$ inch) diameter ice and gelatin impacts (near the back face $\pm 45°$ ply to unidirectional ply interface), it is possible to estimate the defect boundary more precisely. The wave velocity through defect-free material is determined by measuring the distance between two concentric wave fronts and dividing this by 20 microseconds, the time for one cycle. The velocity across the delaminated region is then determined by multiplying the defect-free velocity by the square root of the delaminated zone thickness (measured to the back face) divided by the whole specimen thickness. Knowing the relative velocities, the distance between normal and retarded rings can be translated into time, and this time multipled by the delaminated zone velocity to extrapolate the retarded ring backwards to the actual defect boundary. For the case where the delaminated thickness is approximately one-fourth the whole specimen thickness, as noted visually in several 1.27 cm diameter ice and gelatin impacts, the distance extrapolated back toward the origin is equal to the difference in distance between the normal wave and the retarded wave at any instant. This allows quick determination of accurate defect boundaries by visual means.

The standing wave technique also utilized the 50 kHz transducer to excite the specimen, but the hologram was usually taken of the back face 300 microseconds or longer after the transducer was triggered. At this time, the entire specimen is oscillating, and a standing wave pattern has developed. Material defects show up as regions of irregular standing wave patterns. This technique is somewhat less accurate, but is advantageous in that an overall view of the defective area is visible in a single holographic reconstruction, while two or more reconstructions are necessary from different point sources to outline a defect using the propagating wave technique.

g.   Frequency Determinations

Determinations of pre-impact and post-impact first bending, second bending, and first torsion frequencies for all Task I specimens are presented in Tables X, XI, XII, and XIII. The first and second bending frequencies do not show a consistent correlation with either the extent of damage or impact energy, although projectiles causing indentation and fiber breakage did lower the bending frequencies more than projectiles causing only delamination damage. The torsional frequencies show a correlation between the extent of damage and decreasing torsional frequency, especially with the $[(\pm 45)_2 |0_{12}|(\mp 45)_2]_T$ "core-and-shell" Modmor II/PR-286 specimens impacted in Task I, Part A.

All frequency determinations were made using the same clamping technique utilized during the actual impact tests. Specimens were gripped at the same end which was clamped during impact testing so that 20 cm (8.0 inches) of specimen length extended out of the clamps. Constant torque was used on the clamping fixture bolts for all tests. Frequencies were taken at controlled double-tip amplitudes of 1.5 cm (0.6 inch) in first bending, 0.15 cm (0.06 inch) in second bending, and 0.03 cm (0.01 inch) in first torsion. All frequencies were first identified prior to measurement by using either strobe lights or locating the position of the antinodal areas on the specimen. Difficulty was experienced in inducing the relatively long and narrow Task I specimens to go into first torsion. A small clamp extending a short distance beyond the width was thus attached at the free end of each specimen during the torsion tests to increase the moment about the longitudinal centerline of the specimen. This technique allowed first torsion measurements on a limited number of specimens.

Actual post-test frequencies of nearly all Task I specimens, and in particular Part A specimens, were found to be higher than the pre-test frequencies. The post-test frequencies of eleven Task I Part A specimens which exhibited no visual or ultrasonic damage increased by 11 percent in first and second bending and by 3 percent in first torsion. The reason for this is presently unexplained in specimens where no damage has occurred to cause changes in dimensions or mass, as no mechanism is known by which the composite material modulus could change to cause such an increase in frequency. Analytical modeling of the effect of impact damage upon beam frequencies has predicted decreases in the natural bending frequencies, as would be expected.

The apparent frequency increases are therefore assumed to be the result of a systematic error in the frequency determinations. Consequently, the post-test frequency results in Task I, Part A, (Table X) were compensated by -11 percent in first and second bending and -3 percent in first torsion to reduce the average frequency changes in the undamaged specimens to zero,

16

and to make relative frequency changes in the remaining damaged specimens easier to assess. The post-test frequencies of the Task I, Parts B, C, and D, tests also exhibited increases ranging from approximately +2 percent to +5 percent. These have been left uncompensated, as there were not sufficient undamaged specimens from which to select a baseline.

The compensated percent frequency change results from Task I, Part A, are summarized in Table X. Impacts causing indentation and fiber breakage decreased bending frequencies more than impacts causing only delamination damage. The compensated first and second bending frequencies exhibit changes resulting from steel projectile impacts ranging from +1 percent to -16 percent in first bending, and from no change to -12 percent in second bending. No correlation is evident however between the impact energy or the extent of damage and the magnitude of the frequency change. Impacts with 1.27 cm diameter gelatin and ice resulted in lesser bending frequency changes from zero to -4 percent for most specimens. Two specimens impacted with the 1.27 cm diameter gelatin at approximately 274 m/sec (900 ft/sec) did exhibit frequency losses of -14 percent and -9 percent in first bending, and -11 percent and -6 percent in second bending. Examination of these two specimens after impact revealed broken fibers at the impact face in addition to the delamination damage noted in most other 1.27 cm diameter ice and gelatin impacts. Frequency change results in most specimens impacted with 2.54 cm diameter ice and gelatin were either approximately zero for the case of the undamaged specimens (which were used in the frequency compensation baseline), or else not available due to widespread delamination or specimen fracture.

Comparison of the eighteen Task I, Part A, first torsional frequency results in Table X revealed an excellent correlation between the ultrasonically determined extent of damage and the drop in frequency, independent of the projectile type. The correlation between decreasing first torsion frequency and increasing extent of damage reflects the importance of the $\pm 45^\circ$ shell plies in maintaining torsional stiffness in the "core-and-shell" layup test specimens. The torsional frequency was affected both by direct damage to these plies in the case of the steel projectiles, and by the separation which occurs between the $\pm 45^\circ$ plies and unidirectional plies as a result of the ice and gelatin impacts.

The percent frequency change results after impact for Task I, Part B "Effect of Composite Properties", are shown in Table XI. The majority of the most severely damaged unidirectional specimens were split due to impact with the 1.27 cm diameter ice at 274 m/sec (900 ft/sec), and were therefore unsuitable for post-test frequency testing. Six specimens, with damage extents from 16 percent to 49 percent were in this category. The remaining specimens suitable for testing exhibited damage ranging from 0 percent to 26 percent, and revealed no correlation between the first and second bending or torsional frequencies and the composite specimen variables of fiber type, layup or damage extent. Percent changes in first bending varied from -2 percent to +5 percent and for second bending from no change to +4 percent. Two torsional frequencies exhibited no change. The range of actual post-test frequencies in this group of specimens varied from 39 Hz to 108 Hz in first bending and from 240 Hz to 688 Hz in second bending for the $[(\pm 45)_3 \,|\, 0_6 \,|\, 0]_S$ S-glass/PR-286 and unidirectional boron/PR-286 specimens, respectively.

The percent frequency change results after impact for Task I, Part C "Effect of Ply Configuration, Fiber Content and Thickness", are presented in Table XII. No correlation is evident between ply layup, fiber content or thickness and the effect of the 1.27 cm diameter ice impacts upon the first and second bending response of the specimens. All but two of the post-impact first bending frequencies increased from 0 percent to +4 percent, while all but three of the second bending frequencies increased from +1 percent to +4 percent. The torsional frequencies exhibited a uniform increase of 2 to 4 percent, except for a ±30° angle ply specimen with 16 percent extent of damage which showed only a 1 percent increase, and a $[(\pm 45)_2 \mid 0_6]_S$ core-and-shell specimen with 30 percent extent of damage, which exhibited a 3 percent decrease in first torsion.

The percent frequency change results for the Task I, Part D "Materials Impact Improvement Evaluation", are presented in Table XIII. The first and second bending frequencies were not degraded by the impact damage to the specimens. The single first torsion result does show a 3 percent decrease after impact in a PRD-49-1 +T-75-S/PR-286 specimen with a 24 percent extent of damage. This is the largest torsional frequency decrease noted for any unidirectional test specimen.

h.   Residual Tensile Strength

The completed residual tensile strength determinations for Task I are presented in Tables XIV, XV, XVI, and XVII. The following observations can be made from these results:

- For a given impact energy level, steel > gelatin > ice in reducing the residual tensile strength.

- At speeds $\geq$ 274 m/sec, the 1.27 cm diameter gelatin projectiles caused penetration and fiber breakage with reductions in tensile strength approaching those for steel.

- Decreased residual tensile strengths correlated with increasing ballistic impact energy for most steel, ice, and gelatin impacts above their damage thresholds.

- Zero extent of damage (determined by ultrasonic C-scan) correlated with high residual tensile strengths. Otherwise, extent of damage was not a reliable indicator for predicting the extent of reduction in residual tensile strengths.

- Damage due to ice and gelatin impacts was insufficient to cause tensile failure at the point of impact in many cases. Apparent residual strength losses in specimens where tensile failure initiated away from the point of impact could not be reliably attributed to impact damage.

These findings are discussed in more detail below.

The residual tensile strength results from Task I, Part A "Effect of Projectile Characteristics", are presented in Table XIV.   All specimens impacted were $[(\pm 45)_2 \mid 0_{12} \mid (\mp 45)_2]_T$ Modmor II/ PR-286 graphite-epoxy. Steel projectiles at all velocities caused these specimens to fail in the impacted zone when subjected to tensile loads. An impact using 0.64 cm (0.25 inch) diameter

steel with 1.4 joules of impact energy reduced the ratio of the residual tensile strength divided by the undamaged strength to 0.89. Increasing the impact energy of the 0.64 cm diameter steel projectile to 2.3 joules caused a further reduction of the residual tensile strength ratio to 0.65. Impacts using 0.64 cm diameter steel with energies from 4.8 to 9.0 joules resulted in residual tensile strength ratios between 0.61 and 0.74, with little decrease in the residual strength apparent with increasing impact energy after near penetration of the specimens has been achieved at 4.8 joules. This is a result of the localized nature of the steel impacts. Use of the larger 1.19 cm (0.47 inch) diameter steel caused significantly more damage to the specimens. The residual strength ratios varied from 0.79 with a 2.0 joule impact to 0.38 from a 34.2 joule impact which penetrated the test specimen.

The 1.27 cm (0.5 inch) diameter ice and gelatin impacts in Part A caused less of a reduction in tensile strength for a given impact energy than the steel impacts, with the ice being less severe than the gelatin. The ice impacts reduced the residual tensile strength ratio from 0.91 with a 21.3 joule impact, to 0.61 from a 49.7 joule impact. All specimens failed in the impacted zone. Two specimens impacted with 1.27 cm diameter gelatin at energies of 14.0 joules and 14.9 joules revealed no visible or ultrasonic damage, and failed in tension outside of the impact affected zone and under the bonded fiberglass tabs. The indicated residual tensile strengths for these specimens, 0.97 and 0.76 respectively, are therefore not valid indicators of any impact damage that might have occurred to these specimens. Specimens impacted with gelatin at 23.4 and 25.6 joules did exhibit tensile failures in the impacted zone. The residual strength ratios of these specimens were 0.60 and 0.81 respectively. Damage to the Modmor II/PR-286 specimens resulting from 1.27 cm diameter gelatin impacts at 38.3 joules and 43.2 joules (approximately 274 m/sec velocity) was much more severe, reducing the residual strength ratios to 0.56 and 0.39 respectively. This decrease in residual strength correlates with the onset of projectile penetration noted earlier in the visual examination of these specimens, as opposed to the delamination type damage observed on all 1.27 cm diameter ice impacts and on the lower velocity gelatin impacts. The presence of penetration damage in the specimen implies that the material transverse (through-thickness) compressive strength is being exceeded at the impact specimen/projectile interface due to contact pressures generated at this interface, while the internal delamination damage implies that the transverse (through-thickness) tensile strength is being exceeded internally due to reflected stress waves.

Residual tensile strengths of specimens impacted with 2.54 cm (1.0 inch) diameter ice and gelatin projectiles fell into two groups, specimens exhibiting little or no damage, and those exhibiting severe damage. Impacted specimens exhibiting no ultrasonic or visual damage exhibited residual strength ratios of 0.77 to 0.83 after impact with 2.54 cm diameter ice at energies up to 49.2 joules, and ratios of 0.84 to 0.94 after impact with 2.54 cm diameter gelatin at impact energies up to 19.9 joules. All but one of these specimens failed outside of the impacted zone, and the one failure in the gage area was at a ratio of 0.92. Specimens revealing ultrasonic damage revealed much lower residual strength ratios: from failure in impact at 83.3 joules to 0.48 at 94.6 joules using ice projectiles; and from 0.62 at 49.0 joules to failure in impact at 93.4 joules using gelatin.

The residual tensile strength results from Task I, Part B "Effect of Composite Properties", are summarized in Table XV. Post-impact tensile tests of the unidirectionally reinforced specimens proved to be inconclusive due to the nature of the impact damage sustained by

these specimens. The Modmor I/PR-286 and T-75-S/PR-286 specimens plus one each of the Modmor II/PR-286 and Modmor II/P13N specimens were split into two or more segments and were therefore unsuitable for tensile testing. Damage to the remaining unidirectional specimens was limited chiefly to longitudinal in-plane cracking, with little or no fiber breakage. All but one of these specimens failed away from the impacted area at residual strength ratios of 0.67 to 0.82, or failed to break as was the case with the fiberglass specimens which exceeded the load rating of the tensile fixtures. The tensile failures away from the impacted area occurred under one of the 8.9 cm (3.5 inch) long fiberglass tabs bonded to the ends of the specimens for gripping. The single Modmor II/P13N specimen which did fail through the impacted region exhibited a residual strength ratio of 0.83.

Comparison of residual tensile strengths in the $\pm 45°$ "core-and-shell" layups using PRD-49-1/PR-286, boron/PR-286, and S-glass/PR-286 was not possible because of lack of baseline undamaged tensile strength data for these layups. Estimated residual strength ratios of 0.92 and 0.97 for the boron laminates were determined based upon an estimated undamaged tensile strength for the $[(\pm 45)_2 |0_6]_S$ laminate, and indicate little damage resulting from the 1.27 cm diameter ice impact.

The residual tensile strength results from Task I, Part C "Effect of Ply Configuration, Fiber Content, and Thickness", are presented in Table XV. The comparison of residual strengths of unidirectional Modmor II/PR-286 composites reveals higher residual strengths for the 65 percent by volume specimens (> 1.00 and 0.95) compared to the 47 percent by volume fiber specimens (0.77 and 0.88). Comparison of the angle ply laminates revealed much higher residual strength ratios in the $\pm 45°$ specimens (1.55, 1.47), when compared to the $\pm 30°$ specimens (0.37 and 0.53). The high post-impact tensile strengths in the $\pm 45°$ specimens are unexplained, although one possibility is that the increase gage width of the impact specimens, 5.1 cm (2.0 inch) compared to the 1.9 cm (0.75 inch) gage section in the tensile specimens, may have some effect.

The "core-and-shell" laminates using $0°$ plies with outer "shells" of $\pm 45°$ plies and $\pm 30°$ plies revealed nearly equal residual strength ratios of 0.67 and 0.93 (gage failures), after being impacted with questionable ice balls. The $[(\pm 45)_2 |0_{12} |\mp 45)_2]_T$ specimens exhibited residual strength ratios of 0.83 (failure under tab) and 0.94 (gage failure). These results, when compared with ratios of 0.69 and 0.72 for similar ice impacts with the $\pm 45°$ shell specimens in Part A, indicate that residual strengths for these laminates are nearly equal within the scatter in the tensile tests.

The dispersed ply $[(0| +30|0| - 30|0)_2]_S$ specimens exhibited residual strength ratios of 0.72 and 0.86, with both failures occurring away from the impacted zone, therefore making the effect of the ice impact upon these strengths questionable. The dispersed ply pseudo-isotropic laminates exhibited residual strength ratios of 1.09 and 1.15, indicating no damage from the ice impacts.

The double thickness $[(\pm 45)_4 |0_{12}]_S$ specimens were not weakened sufficiently by impact to allow tensile testing. Attempts to fail one specimen resulted in interlaminar failure under the fiberglass tabs, both in the adhesive and in the test specimen.

20

The residual tensile strength results from Task I, Part D "Materials Impact Improvement Evaluation", are presented in Table XVII. The longitudinal cracking apparent in the PRD-49-1 + T-75-S/PR-286 and the S-glass + T-75-S/PR-286 do not appear to have affected the tensile strength of these unidirectional laminates. The single PRD-49-1 + T-75-S/PR-286 specimen revealed a residual strength ratio of 0.93. The two S-glass +T-75-S/PR-286 specimens exhibited ratios of 1.34 and > 1.04.

i.   Metallographic Inspection

Metallographic inspection of Task I impact specimens was performed to determine the effect of impact type, material, and ply configuration variables upon the location and type of separations observed in the specimens. The location and extent of damage determined metallographically revealed good correlation with post-impact ultrasonic inspection results, and inspection of one specimen through a region showing no ultrasonic damage was found to be defect-free. Inspection of a series of $[(\pm45)_2 |0_{12} |(\mp45)_2]_T$ type Modmor II/PR-286 specimens subjected to different impacts (2.54 cm diameter gelatin at 107 m/sec, 1.27 cm diameter gelatin at 274 m/sec, 1.27 cm diameter ice at 274 m/sec and 282 m/sec, and 0.64 cm diameter steel at 65.8 m/sec) revealed interlaminar delaminations and inplane cracking separations limited chiefly to the unidirectional core plies in all specimens. Major interlaminar delamination planes occurred preferentially near the interface between the back face $\pm45°$ plies and the unidirectional plies, but were also noted at the interface with the impact face $\pm45°$ plies and the unidirectional plies. Additional smaller and more numerous interlaminar and inplane separations were noted within the unidirectional plies of specimens impacted with the 1.27 cm and 0.64 cm diameter projectiles. Cracks angled towards the impact point were evident within the $0°$ plies in specimens impacted with the 1.27 cm diameter ice and 0.64 cm diameter steel. Comparison of unidirectionally reinforced Modmor II/PR-286 and T-75-S/PR-286 composites subjected to 274 m/sec ice impacts revealed multiple separations in the T-75-S, including back face delamination and numerous cracks inclined towards the point of impact. The Modmor II specimen revealed two inplane cracks and limited delamination. Comparison of Modmor II/PR-286 unidirectional, $[(\pm45)_2 | 0_{12} |(\mp45)_2]_T$, and pseudo-isotropic layups subjected to 1.27 cm diameter ice impacts at approximately 274 m/sec shows that addition of $(\pm45°)$ plies limits inplane separations to within the $0°$ unidirectional "core" plies and promotes interlaminar separations in comparison to a $0°$ unidirectional layup. The pseudo-isotropic layup eliminates all interlaminar separations, while reducing inplane separations to microcrack indications limited to within one ply. The specific examples are discussed in more detail below.

Transverse sections were made in nine post-impact specimens and were mounted and polished. The locations of these transverse sections and of the photomicrographs taken of them are shown relative to half-scale ultrasonic C-scan maps in Figures 12 through 19. These C-scan maps also show the point of impact and the extent of damage found after impact. Since six of these specimens were tensile tested prior to metallographic inspection, a transverse section was taken through a specimen exhibiting negligible extent of damage to determine if tensile testing had cuased damage to the specimen after impact. A typical photomicrograph of this specimen in Figure 12 shows no damage. Comparisons of damage with C-scans in subsequent photomicrographs has revealed good correlation with the post-impact C-scans taken prior to tensile testing, indicating that tensile test after impact had little effect upon the observed microstructure.

21

Damage to $[(\pm 45)_2 |0_{12}|(\mp 45)_2]_T$ Modmor II/PR-286 specimen 980-1 due to 0.64 cm diameter steel impact at 65.8 m/sec is shown in Figure 17. Damage is centered near the point of impact, where a zone of cracked and delaminated material is bounded on either side by vertical cracks angled towards the impacted face. A major delamination is also visible near the back-face $\pm 45°$ plies. The high density of separations in 980-1 impacted at 65.8 m/sec is similar in appearance to the microstructure of specimen 976-2 impacted with 1.27 diameter gelatin at 274 m/sec. In both instances, penetration damage had just commenced at the impact face.

Variations in damage as a function of material type are demonstrated by comparison of two unidirectional composites impacted with 1.27 cm diameter ice at approximately 274 m/sec. The transverse cross section of Modmor II/PR-286 specimen, shown in Figure 18, reveals a longitudinal inplane separation with a single delamination branching from one side, in good agreement with the C-scan also shown in the figure. A transverse cross section view of T-75-S/ PR-286 specimen 1005-1 in Figure 19 reveals a large number of cracks angled diagonally pointing towards the impacted face. The impacted face is depressed, and two segments of the back face are separated from the specimen near the back face. Several smaller cracks appear to have propagated preferentially through void defects in this specimen.

The effect of ply layup on Modmor II/PR-286 laminates impacted with 1.27 cm diameter ice at approximately 274 m/sec can be seen by comparison of the unidirectional laminate in Figure 18, the $[(\pm 45)_2 |0_{12}|(\mp 45)_2]_T$ laminate in Figure 15, and the pseudo-isotropic laminate Figure 12. The unidirectional laminate splits completely accompanied with limited delamination. The "core-shell" layup prevents splitting, as the cracking of the $0°$ plies is arrested at the $\pm 45°$ ply "shells", but delamination is promoted at the interfaces between the $0°$ and $\pm 45°$ plies. The dispersed pseudo-isotropic layup shows no delaminations or cracks, and only microcrack indications within individual plies.

j. Scanning Electron Microscope Inspection

Scanning electron microscope studies were conducted with several impacted specimens to characterize their fracture surfaces. All inplane and interlaminar separations were found to occur at the fiber-matrix interface, and in the resin matrix, as shown in Figure 20. Comparison of the impact fractured specimens with transverse tensile specimen and short beam interlaminar shear test specimen fracture surfaces, shown in Figures 21 and 22, indicates that the impact separations are more similar to the transverse tensile failures.

The test specimen fractures both revealed regions of matrix-matrix and fiber-matrix interfacial failures when examined with the scanning electron microscope. The transverse tensile specimen fracture, however, exhibited clusters of totally unbonded fibers which had been dislodged from the fracture surfaces, as shown in Figure 21. A larger number of broken fiber ends and regions of matrix tensile fracture were also visible in the transverse tensile specimen. The short beam interlaminar shear specimen revealed regions where the epoxy matrix surface was relatively smooth, indicative of a clean fiber-matrix interfacial debonding, as shown in Figure 22. Examination of delamination separations from two Modmor II/PR-286 impact specimens, shown in Figure 20, reveals a ragged matrix failure more indicative of tensile fracture.

22

To examine effects of differing impact types, a series of $[(\pm45)_2 \mid 0_{12} \mid (\mp45)_2]_T$ Modmor II/PR-286 specimens were examined. Conditions included 2.54 cm diameter gelatin at 107 m/sec, 1.27 cm diameter gelatin at 274 m/sec, 1.27 cm diameter ice at 274 m/sec and 282 m/sec, and 0.64 cm diameter steel at 65.8 m/sec.

Specimen 984-2 impacted with 2.54 cm diameter gelatin at 107 m/sec, was sectioned just below the impact point through a damaged region as shown by the ultrasonic C-scan in Figgure 13. Examination of the entire transverse section revealed a major delamination plane extending the full specimen width at or near the interface with the back face $\pm45°$ plies and the $0°$ plies. A smaller delamination was visible extending part way across the specimen width at or near the interface with the impact face $\pm45°$ plies and the $0°$ plies. Several longitudinal inplane separations can also be seen connecting the two delaminations, as shown in the cross section view in Figure 13.

A transverse cross section view and C-scan of specimen 976-2, impacted with 1.27 cm diameter gelatin at 274 m/sec, is shown in Figure 14. This specimen exhibited partial penetration damage after impact with major delamination damage visible along both edges at or near the interface between the back face $\pm45°$ plies. Examination of the specimen cross section revealed a large delamination visible externally at the edge. Closer to the specimen center and the point of impact this delamination branched into three or more delaminations, with numerous small cracks and separations visible, as shown in the photomicrograph in Figure 14.

Figure 15 shows the full cross section of specimen 982-4 after impact with a 1.27 cm diameter ice ball at 274 m/sec. The delamination which was visible along the right edge of the specimen near the back face $\pm45°$ plies after impact is clearly visible at the right in Figure 15. This main delamination continues near the back face for 3.3 cm, then angles upward at $63°$ with respect to the horizontal and continues as a delamination for 0.8 cm near the impact face $\pm45°$ plies. Additional delaminations and cracks are also visible along the right half of the specimen, in the indicated damage area shown in the C-scan insert in Figure 15. The front face delamination also continues farther towards the left edge than would be indicated by the C-scan, and may be a result of tensile testing or preparation of the specimen.

A $[(\pm45)_4 \mid 0_{24} \mid (\mp45)_4]_T$ Modmor II/PR-286 specimen (No. 1011-2) was sectioned transversely into six segments and prepared metallographically instead of being tensile tested. Ultrasonic inspection of this specimen after impact with 1.27 cm (0.5 inch) diameter ice at 282 m/sec (926 ft/sec) revealed a damage extent of 4.2 percent in the form of two separate ellipitcal damage indications oriented longitudinally along both sides of the impact point as shown in Figure 16. No visible damage was noted on the specimen. Inspection of the polished section on faces shown in Figure 16 revealed a pair of longitudinal inplane cracks extending through the entire unidirectional ply thickness, and down the full length of the specimen. Three additional shorter cracks were noted in the immediate vicinity of the ice impact. The cracks are perpendicular to the specimen surface at both ends, but the angle decreases to as low as $41°$ with respect to the surface as the cracks approach the impact point from either end. Starting from the back face $0°$ plies, the cracks incline towards the impact point along both sides. The ultrasonic indications correlate with the projection of these cracks onto the specimen surface. The orientation of the cracks near the point of impact suggests an interaction between the tensile waves reflected from the specimen back face, and the existent transverse residual thermal strains which exist in "core-and-shell" type laminates.

B. TASK II SIMULATED BLADE IMPACT TESTS

The objectives of Task II are to determine the damage imposed on simulated blades by controlled impact tests. Specific variables to be investigated include the effect of laminate design, projectile characteristics, impact angle and location to be determined in bench tests, and the effects of applied stress and protection schemes on structural integrity after impact in a spinning arm rig. The test specimen for this task is a cantilevered double-tapered simulated blade of constant cross section with a 7.6 cm (3 inch) chord, 20 cm (8 inch) span, and edge diameter of approximately 0.025 cm (0.010 inch).

Bench tests using 1 gram ice and gelatin projectiles have shown a correlation between increased damage and increasing impact angle in leading edge impacts on graphite-epoxy specimens, and that altering the ply layup to stiffen the leading edge reduces this damage. Impacts using 1 gram steel projectiles caused damage at all impact locations and angles in both graphite-epoxy and titanium-6Al-4V, with the titanium exhibiting less damage than the graphite-epoxy.

1. Specimen Fabrication and Inspection

All graphite-epoxy specimens were molded at 411-422°K (280-300°F) for two hours, followed by a 16 hour oven post cure at 422°K (300°F). The mold was pressed to stops to achieve an average cured ply thickness of 0.013 cm (0.0053 inch) per ply, and thus insure dimensional accuracy at the leading and trailing edges, and also insure the desired 57 volume percent fiber content. The Modmor II/PR-286 specimens exhibited good uniformity, with densities varying from 1.49 g/cc to 1.53 g/cc. The average edge thicknesses of all the graphite-epoxy specimens were within the desired range of thickness, and forty-seven of the fifty specimens fabricated were found to be either "good" or "acceptable" by ultrasonic inspection.

The ultrasonic inspections of the diamond shaped Task II specimens were conducted in similar fashion to those in Task I, but the rating of quality was more complex due to the shape of the parts. All specimens were supported horizontally in an ultrasonic inspection tank such that the longitudinal centerline of each specimen was normal to the incident ultrasonic beam, and the normal vector to both sides made an angle of 2.5° to the beam. Ultrasonic energy was passed down through the specimen, reflected off a reflector plate at the bottom of the tank and passed back through the specimen where it was received and the signal attenuation measured. As the scan is passed to either side of the longitudinal centerline, the degree of attenuation is a function of three variables: (1) material quality, (2) material thickness, and (3) the angle of incidence between the ultrasonic beam and the surface normal of the part. All areas to either side of the specimen longitudinal centerline exhibit a constant and artifically higher degree of attentuation due to higher reflection from the non-normal angle of incidence between the ultrasonic beam and the specimen surface. As the scan progresses towards the thinner edge portions of each specimen, this higher attenuation is offset by the decrease in material thickness. A specimen of uniform quality thus exhibits a narrow region of intermediate attenuation along the longitudinal centerline where the specimen is thickest, and where maximum energy is transmitted due to the normal angle of incidence. Immediately to either side of this region the attenuation increases due to the higher reflectance losses, and gradually decreases as the scan approaches the leading and trailing edges. A sperry Graph-Gate scanner

24

which records changes in attenuation in continuous tones from white to grey was therefore employed with the Task II specimens to detect these expected variations in attenuation. Non-uniformities in the white-to-grey pattern therefore represented non-uniformities in the material. Determination of specimen quality was based upon uniformity of the grey-to-white gradations as the scan progressed from centerline to edge, and upon the minimum distance from the leading edge at which attenuation was discernible. Specimens revealing no attenuation within 1.0 cm (0.4 inch) of the leading edge were rated "good" if visual condition of the leading edge was also superior. Specimens rated "acceptable" required no attenuation within 0.6 cm (0.2 inch). Specimens revealing poorly bonded leading edges or delaminations were rated "not acceptable".

2. Impact Testing and Post Test Inspection

Impact testing and ultrasonic inspection results of all simulated blade specimens in Task II, Part A "Effect of Ply Configuration" and Task II, Part B "Effect of Projectile Characteristics, and Impact Location and Angle", are summarized in Tables XVIII and XIX and Figures 23 through 27. The purpose of these tests was to relate variables of projectile type, impact location and angle, and ply configuration to damage in a simulated blade leading edge structure. Dimensions of the simulated blade specimens utilized in these tests were 7.62 ±0.05 cm (3.00 ± 0.02 inch) chord; and 20.32 ± 0.13 cm (8.00 ± 0.05 inch) span; 0.381 ± 0.013 cm (0.150 ± 0.005 inch) maximum thickness; and a leading edge radius of 0.023 to 0.030 cm (0.008 to 0.012 inch). All specimens were cantilevered with one end gripped over a 6.3 cm (2.5 inch) long by 7.6 cm (3 inch) wide area using specially tapered fiberglass doublers and a vise fixture. Impacts were located 11.4 cm (4.5 inch) from the gripped end, at both leading edge and quarter-chord. Impact angles were 0°, 15°, and 30° with respect to the chordwise centerplane of the specimens. Impact projectiles were 1.27 cm (0.5 inch) diameter for ice and gelatin, and 0.64 cm (0.25 inch) diameter for steel, with all projectiles weighing approximately 1 gram. Velocity was constant at approximately 274 m/sec (900 ft/sec).

The parameters of projectile type, impact location and angle, and ply configuration were all significant in determining the extent of damage to the Task II simulated blade specimens. The 0.64 cm diameter steel projectiles caused measurable damage to both Modmor II/PR-286 and Ti-6Al-4V specimens at all impact angles and locations, and generally caused the most severe damage among the three projectile types in leading edge impacts at 0° and quarter chord impacts at 15°. The 1.37 cm diameter ice and gelatin projectiles caused no damage to Ti-6Al-4V specimens, and caused approximately equal damage extents in impacts with Modmor II/PR-286 specimens, where ice and gelatin impacts were more severe than steel at 30° on the leading edge. Damage to the 0°, ±45° configuration graphite-epoxy specimens appears to have been caused by bending failure at the leading edge due to the momentum component of the impact acting normal to the specimen chord. Damage extents for ice and gelatin varied from no damage in the leading edge impacts at 0°, to 0.6-2.6 percent at 15°, and 4.3-6.0 percent at 30°. The 0°, 90° Modmor II/specimens which employed 90° plies to increase chordwise bending stiffness exhibited no damage after impact by 1.27 cm diameter gelatin at 15° on the leading edge. Impacts at 15° at the quarter-chord location caused no damage to either 0°, ±45° or 0°, 90° Modmor II/PR-286 specimens. These results are discussed in more detail below.

Ultrasonic C-scans of the post-impacted specimens were conducted to determine the extent of specimen area which was effected by the impact. These results are presented as damage extent percentages by dividing the measured damaged area by the total area of the specimens. Areas where the entire thickness of a specimen was removed by impact were also measured and are expressed as percentage of material removal.

The results from Task II, Part A "Effect of Ply Configuration", are summarized in Table XVIII and Figure 23. All impacts were conducted using 1.27 cm diameter gelatin at approximately 274 m/sec (900 ft/sec). The two ply configurations used were the standard $[(\pm 45)_2 |0_{10}]_S$ and a chordwise-stiffened $[(90, 0)_4 |0_6]_S$ layup. The purpose of this testing was to determine the effect of 90° (chordwise) stiffening plies on the performance of the Modmor II/PR-286 composite material in a simulated blade configuration. Comparison of the results for 15° leading edge impacts in Table XVIII and Figure 23 reveals a significant improvement in the impact resistance of the 0°, 90° layup. The 0°, ±45 layup revealed loss of material at the leading edge and damage extents of 1.1 percent and 1.2 percent, compared with no damage in the 0°, 90° layup. Impacts at 15° quarter-chord failed to cause damage in either layup, and two Ti-6Al-4V reference alloy specimens were also undamaged in leading edge impacts at 15°.

Comparison of the two ply layups from the chordwise direction reveals the relative stiffness advantage of the $[(90, 0)_4 |0_6]_S$ layup over the $[(\pm45)_2 |0_{10}]_S$ layup for resisting impact loads applied at the leading edge and normal to the specimen thickness. The first 0.61 cm (0.24 inch) of the leading edge in the chordwise direction consists of only the four outer "shell" plies, which are oriented at 0°, 90°, 90°, 0° relative to the chordwise direction in the $[90, 0)_4 |0_6]_S$ layup and at −45°, +45°, +45°, −45° relative to the chordwise direction in the $[(\pm45)_2 |0_{10}]_S$ layup. Using tensile modulus values from Task I for 0°, 90°, and ±45° Modmor II/PR-286 of 135 GN/m² (19.6 x 10⁶ psi), 9.24 GN/m₂ (1.34 x 10⁶ psi) and 17.2 GN/m² (2.48 x 10⁶ psi) respectively, plus a simple rule-of-mixtures modulus approximation yields a chordwise modulus at the leading edge of 72.4 GN/m² (10.5 x 10⁶ psi) for the $[90, 0)_4 |0_6]_S$ layup versus 17.2 GN/m² (2.48 x 10⁶ psi) for the $[(\pm 45)_2 |0_{10}]_S$ layup. The relative stiffness advantage in bending is therefore greater than 4:1 for the $[(90, 0)_4 |0_6]_S$ layup since the chordwise plies lie on the outer skin. This stiffness advantage enables the $[(90, 0)_4 |0_6]_S$ layup specimens to withstand a greater force without exceeding the fracture strain of the material.

The results from Task II, Part B "Effect of Projectile Characteristics, and Impact Location and Angle", are summarized in Table XIX and Figures 24 through 27. All specimens were (0°, ±45°) Modmor II/PR-286 graphite-epoxy or Ti-6Al-4V reference alloy of the same dimensions. The 0.64 cm diameter steel projectiles caused measurable damage in both the Modmor II/PR-286 and Ti-6Al-4V specimens in all cases. Figure 24 shows typical damage to Modmor II/PR-286 specimens resulting from 0.64 cm steel impact as a function of impact angle and location. The 0.64 cm diameter steel projectiles penetrated the composite specimens, causing higher damage and material loss extents for quarter-chord impacts at 15° and leading edge impacts at 0° than in either the 15° or 30° impacts on the leading edge. Delamination of the back face plies was usually evident, and is prominent in the leading edge and quarter-chord impact back face views in Figure 24. Damage extents averaged 6.3 percent for 15° impacts at quarter chord, 3.0 percent for 0° impacts on leading edge, 0.9 percent for 30° impacts on the leading edge, and 0.6 percent for 15° impacts on the leading edge.

26

Impact damage due to 0.64 cm diameter steel impacts on Ti-6Al-4V simulated blade specimens was less severe than that for the composite specimens. The steel projectile impacts did not penetrate the titanium alloy, but were sufficient to cause considerable bending deformation of the leading edge, as seen in Figure 25. The deformation due to the 15° impact on the leading edge is more severe than at 0° due to the momentum component normal to the specimen edge in the 15° impact. Impacts at 15° quarter-chord caused only minor indentation. Average ultrasonic damage extents as a function of location and angle were 0.6 percent at 0° on the leading edge, 1.1 percent at 15° on the leading edge, and 0.2 percent at 15° quarter-chord.

The effect of impact location and angle upon damage to 0°, ±45° Modmor II/PR-286 simulated blade specimens impacted with 1.27 cm diameter gelatin is shown in Figure 26. The gelatin projectiles show no evidence of penetration of the graphite composite on 0° impacts at the leading edge. Impacts at 15° and 30° on the leading edge cause bending failures with delamination at the back face. Damage is more widespread at the 30° angle, as would be expected due to the momentum component to the impact normal to the chordwise centerplane of the specimen which increases as the sine of the impact angle. The momentum component normal to the chordwise centerplane increases from zero at 0°, to 7.66×10^{-2} Kgm/sec (0.553 ft-lb/sec) at 15°, and 14.8×10^{-2} Kgm/sec (1.07 ft-lb/sec) at 30°. Ultrasonic damage extents for gelatin from Tables XVIII and XIX averaged 1.2 percent at 15° on the leading edge, and 5.8 percent at 30° on the leading edge. No damage was observed due to 15° quarter-chord impacts, probably due to the greater thickness of the composite at the quarter-chord location.

The effect of impact location and angle on damage to 0°, ±45° Modmor II/PR-286 simulated blade specimens impacted with 1.27 cm diameter ice is shown in Figure 27. The variations of damage extent due to ice impacts are similar to those observed with gelatin projectiles. No damage is observed in either 0° impacts at the leading edge of 15° quarter chord impacts. Average damage extents from Table XIX for 15° and 30° impacts at the leading edge are 1.6 percent and 4.6 percent, respectively.

Ice and gelatin projectiles caused no measurable damage extents in impacts with Ti-6Al-4V specimens at 0° and 15° on the leading edge, and at 15° quarter-chord.

3.   Instrumented Specimen Impact Results

The initial peak strain results are summarized in Table XX for the seventeen instrumented specimens tested in Task II, Parts A and B. The magnitudes of these strains correlated with variations of specimen material, projectile type, impact angle, and impact location. Each specimen was instrumented with four Micro-Measurements type EA-06-125AC-350 strain gages. Strain gages at locations No. 1, No. 2, and No. 3 were oriented chordwise at quater-chord, half-chord, and three-quarter-chord respectively behind the point of impact to measure impact strains, while gage No. 4 was mounted axially just above the specimen grips, to measure bending strains. The peak strain data was reduced from on-line oscilloscope photographs taken at a sweep rate of 50 μ sec/cm. The 300 Hz to 50 kHz tape system used previously in Task I was used as a back-up on all channels, and as a record of long term bending response of the specimens.

The range of peak strains in Table XX varied from negligibly small to as high as 1.12 percent. Highest strains were recorded at gage No. 1, located directly behind the point of impact, at quarter-chord location on the specimen back face. Peak strains at mid-chord (gage No. 2) were considerably lower than at gage No. 1, and were also somewhat less than the peak strains recorded at gage No. 3. The higher strains at the more distant gage No. 3 are probably a function of the decreased thickness at that location compared to gage No. 2. The peak strains recorded at gage location No. 4 were the lowest except for a few cases where they exceeded the mid-chord (gage No. 2) strains, and indicates that overall axial bending stresses were low.

Comparison of peak strain response as a function of material and configuration variables indicates that Ti-6Al-4V $<$ 0°, 90° Modmor II/PR-286 $<$ 0°, ±45° Modmor II/PR-286 in peak strain amplitudes. In 1.27 cm (0.5 inch) diameter gelatin impacts at 15° on the leading edge, gage No. 1 peak strains are 0.320 percent for Ti-6Al-4V, 0.512 percent for 0°, 90° Modmor II/PR-286 graphite-epoxy, and 0.672 percent for 0°, ±45° Modmor II/PR-286. In quarter-chord impacts with the 1.27 cm diameter gelatin, the gage No. 1 peak strains are -0.048 percent for Ti-6Al-4V, -0.088 percent for 0°, 90° Modmor II/PR-286, and -0.102 percent for 0°, ±45° Modmor II/PR-286. The peak strains at the other gage locations exhibit the same relative ranking.

Comparison of projectile types in Table XX reveals that steel $>$ gelatin and ice in causing high peak strains, except at the 30° leading edge impact location, where the steel projectile penetrated the thin leading edge without causing appreciable strains at the four gage locations. Comparing gage No. 1 peak strain responses in 0°,±45° Modmor II/PR-286 for the three projectile types as a function of impact angle and location reveals: 0.960 percent for steel versus 0.032 percent for ice and 0.018 percent for gelatin at 0° leading edge; + OFF SCALE for steel versus 0.600 percent for ice and 0.672 percent for gelatin at 15° leading edge; + OFF SCALE for steel versus 0.112 percent for ice and -0.102 percent for gelatin at 15° quarter-chord; and -0.160 percent for steel versus 0.440 percent for ice and 1.12 percent for gelatin at 30° leading edge. The "OFF SCALE" strains generally denote peak strains greater than 1.2 percent depending upon the sensitivity used on the oscilloscope.

Increasing peak strain levels correlate with increasing severity of damage as measured ultrasonically. The 0.64 cm (0.25 inches) diameter steel projectiles which caused the highest peak strains in 0° and 15° leading edge impacts, and 15° quarter-chord impacts, also caused the highest extents of damage as shown in Table XX. For the 30° leading edge impacts the highest damage extent resulted from the gelatin impact, with a peak strain of 1.12 percent recorded at gage No. 1.

The overall strain levels resulting from the deformable ice and gelatin impacts reveal increasing deflection as a function of increased impact angle at the leading edge, and decreasing deflection as a function of increased specimen thickness at the point of impact. The overall ranking of impact strains in order of decreasing strains is: 30° -LE $>$ 15° -LE $>$ 15° -QC $>$ 0° -LE.

In the 0°, ±45° Modmor II/PR-286 graphite-epoxy simulated blades, no damage was found in specimens exhibiting peak strains of up to 0.112 percent, while damage was exhibited in specimens with peak strains of -0.160 percent (steel impact) and 0.440 percent or higher for

ice and gelatin impacts. A $0°,90°$ Modmor II/PR-286 specimen withstood peak strains to 0.512 percent without exhibiting any damage. Thus the $0°,90°$ configuration exhibits superior impact resistance due to lower strains for a given impact severity, and due to a higher strain capability prior to failure.

4.   Frequency Determinations

The post-impact frequency determinations have been completed in first bending, second bending, and first torsion for all Task II simulated blade shaped specimens in Part A "Effect of Ply Configuration" and Part B "Effect of Projectile Characteristics and Impact Location and Angle". These results are summarized in Tables XXI and XXII as percent frequency changes based upon the frequencies determined from each specimen prior to impact testing.

All specimens were clamped with uniform torque at the same end which was gripped during impact testing. Clamping length was 2.5 cm (1.0 inch). Bending frequencies were taken at controlled double tip amplitudes of 1.5 cm (0.600 inches) in first bending and 0.15 cm (0.060 inches) in second bending for all Modmor II/PR-286 specimens, and at 1.5 cm (0.600 inches) in first bending and 0.25 cm (0.100 inches) in second bending for all Ti-6A1-4V specimens. All specimens were tested in torsion by magnetically driving small weights which extended beyond the width at the specimen free end. The amplitude for the torsional tests was 0.10 cm (0.040 inches) for the Modmor II/PR-286, and 0.025 cm (0.010 inches) for the Ti-6A1-4V specimens. Standard Ti-6A1-4V and Modmor II/PR-286 reference specimens were tested periodically during all frequency determinations to prevent systematic shifts from occuring in the results.

The bending and torsional frequencies were not significantly degraded due to damage resulting from the impact tests, and no correlation was found between ultrasonically measured extent of damage and percent change in frequency. Comparison of the average percent frequency change of all 11 undamaged Modmor II/PR-286 specimens with those of all 17 damaged Modmor II/PR-286 specimens in Parts A and B revealed the following: + 0.3 percent undamaged versus +0.6 percent damaged in first bending; —0.4 percent undamaged versus —0.1 percent damaged in second bending; and +1.5 percent undamaged versus —0.6 percent damaged in first torsion. A similar comparison between the 12 undamaged and 6 damaged Ti-6A1-4V specimens in Task II, Parts A and B, revealed average changes in the frequencies to be: —0.5 percent undamaged versus —1.1 percent damaged in first bending; —1.0 percent undamaged versus —1.5 percent damaged in second bending; and 0.0 percent undamaged versus +1.0 percent damaged in first torsion. The insensitivity of the bending frequencies to impact damage can be attributed to the location of the impact damage which is away from the gripped end, as was found in Task I, and to the fact that fewer of the unidirectional load bearing plies in the specimen core were damaged than in the Task I normal inpacts. The lack of correlation between ultrasonic extent of damage and torsional frequencies is probably a result of the relatively small portion of the total area affected by the edge-on impacts, compared with damage extents in Task I. The maximum extent of damage exhibited by a Task II impacted specimen was only 8.1 percent.

5. Metallographic Inspection

Transverse sections were prepared from simulated blade specimens impacted with 1.27 cm diameter gelatin, 1.27 cm diameter ice, and 0.64 cm diameter steel projectiles, for comparison of damage extents. Damage due to ice and gelatin projectiles was limited to removal of the leading edge and some of the back face crossplies. Ice and gelatin impacts at quarter-chord caused no damage. Steel impact at quarter-chord caused extensive breakup of the composite similar to normal steel impacts in Task I.

Figure 28 shows typical damage caused by a 1.27 cm diameter gelatin impact at 30° on the leading edge. The leading edge has been removed at the point of impact, with limited cracking visible in the remaining specimen material. The fracture appears to be a bending failure of the leading edge which initiates at the impact surface (top) and tears outer crossplies away from the back face (bottom), Figure 28.

Figure 29 shows cross section views at the quarter-chord location of a 0,90° Modmor II/ PR-286 and a 0,±45° Modmor II/PR-286 simulated blade impact specimen after each specimen had been impacted at 15° quarter-chord with 1.27 cm diameter gelatin. Neither specimen reveals any bending failure or stress wave delamination and cracking damage. The lack of stress wave damage indicates that the normal velocity component of 69 m/sec (225 ft/sec) is below the damage threshold of the material as indicated from Task I results. Thus leading edge damage at 15° cannot be attributed to stress wave effects. The lack of bending failure at quarter-chord compared with the same impact at the leading edge is thus due to the greater strength of the thicker section at the quarter-chord location.

Damage due to a 0.64 cm diameter steel impact at 15° quarter-chord is shown in Figure 30. The impact damage is characterized by penetration and the multiple cracks and delaminations which were evident in specimens exhibiting stress wave damage due to normal inpacts in Task I. This indicates that the normal velocity component of 69 m/sec (225 ft/sec) in this impact is in excess of the stress wave damage threshold, as would be expected from the Task I results which indicated that a normal velocity of only 62 m/sec (200 ft/sec) was sufficient to cause stress wave and penetration damage with the 0.64 cm diameter steel projectiles.

6. Residual Tensile Strength

Residual tensile strength was determined as a function of impact damage for a selected group of nine Task II simulated blade specimens. The results, shown in Figure 31, indicate that leading edge damage does not cause a significant reduction in the residual tensile strength of the specimens, but that 0.64 cm diameter steel impacts at quarter-chord reduce tensile strength by approximately one-half.

Eight impact damaged specimens were divided into four groups: "no damage" specimens resulting from 15° quarter-chord impacts with 1.27 cm diameter ice and gelatin; "minor damage" specimens impacted with ice and gelatin at 15° on the leading edge; "moderate damage" specimens impacted with ice at 30° on the leading edge; and "major damage" specimens impacted at 15° quarter-chord with 0.64 cm diameter steel. The reference tensile strength of 568 MN/m^2 (82.5 ksi) was determined from a non-impacted specimen. The residual tensile

strengths of the undamaged specimens, and those specimens receiving minor to moderate damage to the leading edge exhibited no significant variation from the reference strength, ranging from 506 MN/m^2 (73.6 ksi) to 632 MN/m^2 (91.7 ksi). The insensitivity of the residual tensile strength to impact damage at the leading edge reflects the fact that few 0° plies were damaged. This is due to the specimen core-and-shell layup, which places a larger proportion of ±45° plies along the edges, and higher proportion of the load bearing 0° plies towards midchord. The first 0.6 cm (0.24 inches) of the 0,±45° simulated blade specimen layup leading edge in the chordwise direction consists of ±45° layers only. The 0.64 cm diameter steel impacts at the quarter-chord location caused fiber breakage in the 0° unidirectional plies resulting in residual tensile strengths of 307 MN/m^2 (44.5 ksi) and 267 MN/m^2 (38.7 ksi).

7.   Spin Impact Tests

The goal of the spin-impact simulated blade test program was to determine the effect of applied stress, increased projectile mass and velocity, and use of a leading edge protection scheme on impact damage. The results of these tests are summarized in Table XXIII. The effect of stress was determined using the F-39 whirl/FOD test cell at the Hamilton Standard Division of United Aircraft. Rotating simulated blade specimens were impacted 8.9 cm (3.5 inches) from the tip at 15° and 30° on the leading edge with ice, steel, and gelatin projectiles at relative speeds of 274 m/sec (900 ft/sec) and 396 m/sec (1300 ft/sec) at the impact point.

Results of these tests showed that:

- Damage to centrifugally stressed spin impact specimens without leading edge shields was comparable to damage to specimens impacted using the air cannon.

- The leading edge FOD shields afforded almost complete protection to the composite in leading edge impacts with 0.64 cm diameter steel and 1.27 cm diameter ice and gelatin projectiles.

- The leading edge FOD shields provided substantial protection against 2.54 cm diameter ice impacts at 30° to the leading edge. Gelatin projectiles caused more severe damage.

- The 2.54 cm diameter ice impacts at 400 m/sec caused denting to titanium, and did not fail the composite specimens.

a.   Test Technique

The test specimens consisted of seventeen 0°,±45° Modmor II/PR-286 graphite-epoxy simulated blades, and three identically shaped reference specimens of Ti-6Al-4V alloy. Thirteen of the Modmor II/PR-286 graphite-epoxy specimens were fitted with a metallic leading edge protection scheme.

All specimens were tested in a chamber evaluated to 254 torr, using a variable speed rotating arm rig capable of producing specimen mid-span rotational velocities of 396 ± 6 m/sec (1300

± 20 ft/sec). The impacting media were dropped into the specimen plane of rotation using a remotely actuated gravity drop chute for the 0.64 cm diameter steel projectiles, and by means of a pivoted arm apparatus for all other projectiles. All impacts were located at the leading edge, 11.4 cm (4.5 inches) from the gripped end, at an angle of 15° with respect to the chordwise centerplane of the specimen for steel projectiles, and 30° for ice and gelatin projectiles. The specimens were gripped using adhesively bonded fiberglass doublers which were bolted to the whirling arm rig as shown in Figure 32. The fixture was inclined at 15° and 30° angles with respect to the plane of rotation for the impact tests. The temperature of the leading edge was estimated during each test by applying temperature sensitive paint to the backside of each specimen prior to each run.

b. Leading Edge FOD Shield

The objective of the leading edge protection is to provide improved resistance to both local damage and to structural damage resulting from high velocity impact during a controlled spin impact test. The leading edge protection must also perform this function while conforming to the aerodynamic dimensions of the existing airfoil.

The leading edge protection scheme used for the Task II spin impact tests consists of a 0.15 cm (.006 inches) annealed stainless steel foil wrapped over a 304 stainless steel insert as shown in Figure 33. The foil extends 2.5 cm (1.0 inch) back from the leading edge on both sides of the specimen. The leading edge of thirteen 0°,±45° Modmor II/PR-286 specimens was removed to a chordwise depth of 0.86 cm (0.340 inches) and spanwise from 5.1 cm (2 inches) from the tip to a point 7.6 cm (3 inches) from the gripped end. The 304 stainless steel insert was 7.6 cm (3.0 inches) long, 0.84 cm (0.330 inches) wide, by 0.12 cm (0.047 inches) thick at the thickest point. The foils were preformed to the approximate dimensions of the specimens, and the inserts were brazed to the foils. The entire leading edge shield was then adhesively bonded to the simulated blade specimen, using Miller-Stephenson 907 epoxy adhesive.

c. Results

The results of the spin impact tests are summarized in Table XXIII and Figure 34.

(1) Effect of Applied Stress

Initial tests were conducted using three unprotected composite specimens and two titanium-6Al-4V reference specimens to assess the effects of rotating stress in the spin tests against identical air cannon tests conducted previously in Task II. The test conditions were: 274 m/sec relative velocity at 15° on the leading edge with the 0.64 cm steel projectiles for one composite plus the two titanium specimens; and 274 m/sec relative velocity at 30° on the leading edge using 1.27 cm diameter ice and gelatin against each of the other unprotected composite specimens. The 30° angle was utilized with the ice and gelatin projectiles to provide more severe damage and therefore provide better comparison with the leading edge shield protected specimens.

Damage to the unprotected spin impacted Modmor II/PR-286 specimens was comparable to that for the air cannon tests. The steel spin-impacted specimen, NAS-31 shown in Figure 34

32

reveals an 0.5 cm wide by 1.8 cm long hole due to an impact just behind the leading edge which is similar to damage shown for specimen NAS-9 in Figure 24 for a quarter-chord impact.

Spin-impacted specimen NAS-49, impacted with ice (Figure 35 left) reveals a 1.3 cm wide by 0.4 cm deep triangular piece removed from the leading edge. This is less severe than damage to specimen NAS-34 (Figure 27) where a 3.3 cm by 0.7 cm piece was removed and comparable to specimen NAS-37, which lost a 1.0 cm square portion of the leading edge. The variation in damage indicates that some impacted specimens may take only a partial slice of the ice projectile during impact. The gelatin spin-impacted specimen, NAS-21 shown in Figure 36, lost a 2.0 cm wide by 0.9 cm deep portion of the leading edge, compared with 1.5 cm wide by 0.9 cm deep for the air cannon impacted specimen NAS-40, and 2.0 cm wide by 1.0 cm deep for specimen NAS-45 (Figure 26).

Damage to the Ti-6Al-4V reference specimens due to spin impact tests with 0.64 cm diameter steel may be compared directly to the bench test results. A head on impact caused a semi-circular dent in spin-impacted specimen NAS-103 (Figure 37, top) and in bench tested NAS-104 (Figure 25, top). A glancing impact caused indentation and backside cracking on spin-impacted specimen NAS-101 (Figure 37, bottom) and bench impacted specimen NAS-113 (Figure 25, middle). The similarity of impact damage with and without applied stress is a result of the relatively low tensile stress level in the specimens at the impact location. The formula for centrifugal stress, F_c, is as follows:

$$F_c = \frac{mv^2}{R} \tag{1}$$

where m is the rotating mass, v is the velocity, and R is the radius from the axis.

The centrifugal force was estimated by assuming all the mass beyond the impact location to be at a single radius midway to the tip. Taking the values of F_c and dividing by the cross sectional area of the simulated blade specimens yields mean stress levels in the graphite-epoxy of 8.3 MN/m² (1.2 ksi) at 274 m/sec, and 18 MN/m² (2.6 ksi) at 396 m/sec. Performing the same calculation for the denser Ti-6Al-4V yields stresses of 23 MN/m² (3.4 ksi) at 274 m/sec, and 4.9 MN/m² (7.1 ksi) at 396 m/sec.

(2) Effect of Leading Edge Protection

The effect of leading edge protection was assessed in three steps. The 274 cm/sec velocity impacts were first compared against unprotected composite using 0.64 cm diameter steel at 15° on the leading edge and 1.27 cm diameter ice and gelatin at 30° on the leading edge. The projectile mass was then increased, keeping impact angle, location, and velocity constant, and increasing the projectile size from 0.64 cm to 1.27 cm diameter for steel, and from 1.27 cm to 2.54 cm diameter for ice and gelatin. Finally the velocity was increased to 396 m/sec (1300 ft/sec) at 15° on the leading edge with 2.54 cm diameter ice. The third stage was conducted using three specimens: an unprotected Modmor II/PR-286 composite specimen; a composite specimen with leading edge shield; and a Ti-6Al-4V reference specimen.

33

The effect of leading edge protection against steel projectiles is summarized in Tabel XXIII and shown in Figures 34 and 38. The leading edge shield on specimen NAS-22 in Figure 34 was nearly penetrated by a direct impact. However, the composite was protected against the 0.64 cm diameter projectile, as shown in a metallographical cross section view of the composite just behind the point of impact in Figure 38. By contrast, specimen NAS-29 which received two glancing impacts at 15° mid-chord, exhibited severe internal stress wave damage, including delaminations and broken fibers through the entire specimen thickness at mid-chord, as shown in Figure 39. The extent and severity of this damage indicates that cumulative shock wave damage due to hard body impacts could pose a serious threat to unprotected composite structures due to the relatively minor extent of externally visible damage at the point of impact compared with the large extent of internal damage. Comparison of the damage in NAS-29 to that in NAS 22 (Figure 38) further reveals that proper shielding can be effective against the stress wave and penetration damage caused by these impacts. In an impact using a more massive steel projectile, the leading edge shielded specimen NAS 5 absorbed a light impact with a 1.27 cm diameter steel projectile with only minor denting to the shield (Figure 34).

The effect of leading edge protection against ice projectiles is shown in Figures 35 and 40. The leading edge shield on specimen NAS-47 appears to have provided complete protection against the 1.27 cm diameter projectile at 30° on the leading edge, while these same impact conditions caused loss of composite from the unprotected specimen. The second shielded specimen, NAS-6 revealed only minor bending of the leading edge foil due to an apparent void in the braze bond between the foil and the leading edge insert at the point of impact. Specimens NAS-48 and NAS-36 (Figure 35), impacted with a 2.54 cm diameter projectile at 30°, each exhibited a dent in the shield at the point of impact. Damage to the underlying composite was minimal, as shown in a cross sectional view of NAS-48 in Figure 40.

The effect of leading edge shield protection against gelatin impacts is shown in Table XXIII and Figures 36 and 41. The leading edge shield provided nearly complete protection against the 1.27 cm diameter gelatin projectiles at 30° on the leading edge, revealing only slight debonding of the shield in specimen NAS-50. The 2.54 cm diameter gelatin at 30° caused some bending of the shield in specimen NAS-33, and caused severe specimen delamination and shield debonding in specimen NAS-38 (Figure 36). The severity of the damage transmitted to the composite can be seen in Figure 41 which shows a cross section view of the region behind the point of impact, showing major delaminations and cracking.

The effect of leading edge shield against 396 m/sec (1300 ft/sec) impacts with 2.54 cm diameter ice projectiles at 15° is shown in Figure 42. The Ti-6Al-4V reference specimen revealed a 2 cm wide semicircular dent in the leading edge. The unprotected graphite was severely damaged, but remained intact with a 4.8 cm wide (at leading edge) by 2.2 cm deep segment removed. The leading edge protection was removed from specimen NAS-12 due to the impact, with little damage to the remainder of the specimen. The two results with the Modmor II/PR-286 composite may not be truly representative because of the elevated temperatures generated during these tests due to the high tip speeds and the low vacuum. The estimated temperatures at the impact location were 408°K (275°F) for the unprotected specimen NAS-32, and 394°K (250°F) for the shielded specimen NAS-12. Separate work with HMS/PR-286 composite with the same cure cycle used for the Modmor II/PR-286 simulated blade specimens revealed a 20 percent decrease in transverse tensile strength and

a 24 percent decrease in transverse tensile modulus at 422°K (300°F). Moreover, the adhesive system utilized to bond the leading edge shields was designed for only 367°K (200°F) capability.

C. TASK III BALLISTIC ANALYSIS

1. Impact Modeling

a. Introduction

The objectives of the impact modeling analysis are: (1) to establish the important projectile/ target variables during impact; and (2) to utilize the variables of projectile type, mass, and velocity together with target variables of fiber type and layup to explain the types and extent of damage observed during the flat-normal impact tests conducted in the contract. The approach of the present analysis has been to establish bounds to the problem of an impact load applied to a transversely struck beam, and then to proceed to the calculation of beam deflections, and projectile/target contact stresses as a function of impact parameters. The effects of load, contact stress, and deflections are then related to the types of impact damage observed in Task I, Part A "Effect of Projectile Characteristics", conducted with $[(\pm45)_2 |0_{12}|(\mp45)_2]_T$ Modmor II/PR-286 graphite-epoxy composite.

The results of this analysis have shown that the mechanical behavior of the projectile and the bending response of the target during impact are important variables affecting the degree of impact damage to composite materials. A method of damage classification is presented for normal impacts in Task I, and a means of relating this classification is presented for predicting types of damage resulting from non-normal ballistic impacts to Task II specimens and to fan blades at typical operating conditions.

b. Procedure

The Task I, Part A impact tests were selected for the impact modeling as these are the largest body of tests (36 impacts) available using a single target ($[(\pm45)_2 |0_{12}|(\mp45)_2]_T$ Modmor II/PR-286), utilizing a total of 18 different projectile type/mass/velocity variables.

Three models have been utilized: the Hertz model; a modification of the Hertz model developed by Pratt & Whitney Aircraft; and an impulse model.

c. Hertz Model

The classical Hertzian impact assumes that the force acting upon the target due to an impacting spherical body is a function of the distance, α, between the centers of gravity of the particle and the target by the relationship (Reference 1):

$$F = n\alpha^{3/2}$$

where n is a function of the particle radius, Poisson's ratio, and modulus of elasticity of the particle and the target and

1) target and projectile are assumed isotropic and elastic
2) target body is assumed semi-infinite.

The Hertzian model assumptions are not met during the actual impact conditions encountered during the experimental phase of this work. Most importantly, the assumption of infinite target mass implies no bulk translation of the target during the impact. This has been shown to be a poor assumption based upon high speed photography and strain gage instrumentation results which have shown that a large first and second cantilever bending response is caused in the specimens due to the transverse impacts in Task I. Secondly, the assumption of isotropic and elastic target response is invalid. The graphite-epoxy target material is transversely isotropic within each ply, however, the response of a multidirectionally reinforced laminate is much more complex. The response of the graphite-epoxy composite material is essentially elastic to failure, therefore, the assumption of elastic behavior is good below the penetration threshold with ice and gelatin projectiles, and reasonable at the lowest velocities used with steel projectiles, where nonlinear target deformation was limited to small indentations at the impact face. The assumption of elastic target behavior becomes increasingly invalid as the penetration threshold is exceeded in any impact.

Projectile mechanical behavior may be characterized as elastic and isotropic for steel only within the range of conditions utilized in Task I Part A. Ice and gelatin are isotropic, but have low elastic limits. Ice shatters at low stresses (Figure 9), while gelatin splatters (Figure 8), resulting in near zero rebound velocity.

The Hertz impact model, based upon completely elastic behavior and no bulk compliance of the target beam, thus, predicts complete elastic rebound of the particle at the incoming impact velocity, and predicts an upper bound for the impact loads and contact stresses due to impact.

d. Modified Hertz Analysis

The Hertz analysis was modified to conform more realistically to the actual experimental conditions. The most significant modification made to the Hertz model has been an alteration of the contact force such that the bending compliance of a cantilevered beam target is accounted for, instead of requiring a semi-infinite target body as previously required. The Hertz assumption of isotropic material behavior has been partially accounted for by utilizing an equivalent bending modulus for the bending compliance calculation, and by substituting the composite material transverse tensile modulus for the indentation modulus. The Hertz assumption of elastic material behavior with target and projectile appears to be reasonable for the low speed steel impacts where visual deformation of the targets were minimal, and for low velocity gelatin impacts where both target and projectile appear to be undeformed after impact. Ice impacts are elastic until the yield strength of the ice is exceeded. However, compressive tests at low strain rates with ice revealed yield strengths in the range of only 0.98-$3.62 Mn/m^2$ (142-525 psi) (Reference 2).

The problem of a cantilever beam struck by a sphere was used to refine the contact force in the impact model. By superimposing the Hertz solution and the forced vibration of the beam, the time dependent force acting on the beam can be obtained from the solution of an integral equation (Reference 3). The integral equation does not lend itself to standard solution techniques, and an approximate numerical solution was therefore necessary. The solution was first obtained for a simply supported steel beam impacted with a spherical steel projectile. Results of this calculation showed that the maximum load for the Hertz solution was approximately 1.5 times the maximum load predicted by the beam solution, which was the expected result, since the Hertz impact problem provides an upper bound on the load. The impact times were nearly equal for the two solutions.

To account for the target compliance, transverse impact of a spherical projectile on a cantilevered beam was analyzed. The geometry is shown in Figure 43.

The beam, originally at rest, is struck by a mass, M, with initial velocity v_o, at a point $x = c$. The approach distance, α, is the difference of the displacement of the mass, W_2, and the deflection of the beam at the contact point, $W_1 <C>$, so that

$$\alpha = W_2 - W_1 <c> = V_o t - \frac{1}{M} \int_o^t dt_2 \int_o^t F(t_i)\, dt_1 - W_1 <c>$$

By replacing the displacement $W_1 <c>$ by a function representing the forced beam deflection and α by a force indentation relation, an integral equation for $F(t)$ is obtained. For a beam of length L, we have

$$W_1 <c> = \frac{1}{\rho A} \sum_{i=i}^{\infty} \frac{[X_i <c>]^2}{\omega_i \int_o^L X_i^2\, dx} \int_o^t F <\tau> \sin \omega_i (t-\tau)d\tau$$

The eigen functions X_i and frequencies ω_i are determined from the equations of free vibrations of the beam and depend on the boundary conditions of the beam. For simplicity, we assume the Hertz law of contact applies, and is given by

$$\alpha = KF^{2/3}$$

Substituting, we obtain the integral equation for F(t),

$$V_o t - \frac{1}{M} \int_o^t dt_2 \int_o^{t_2} F(t_1) dt_1 = KF^{2/3} +$$

$$+ \frac{1}{\rho A} \sum_{i=1}^{\infty} \frac{[X_i <c>]^2}{\omega_i \int_o^L X_i^2 dx} \int_o^t F <\tau> \sin \omega_i (t-\tau) d\tau$$

The force obtained from this analysis is in general agreement with expected results, that when a sphere strikes a beam, the motion of the beam decreases the force, but the contact time remains about the same.

The modified Hertz program thus presents a realistic approximation to transverse beam impacts where both target and projectile behave elastically, such as low velocity impacts with 1.27 cm (0.5 inch) diameter gelatin, and low velocity impacts with both 0.64 cm (0.25 inch) and 1.19 cm (0.46 inch) diameter steel. At higher velocity, the assumptions break down so that the modified Hertz analysis provides only a guide.

e. Momentum-Impulse Transfer

The momentum-impulse transfer analysis was developed exclusively for the ice and gelatin impacts, where assumption of elastic behavior leads to a prediction of projectile rebound, while strobe photography reveals that there is minimal rebound due to deformation and break-up of the projectile (Figures 8 and 9). The projectile is assumed to be a fluid with density equal to that of the projectile being modelled, with no elastic response. The target is initially considered to be semi-infinite, but this assumption is later relaxed to include the effects of target beam displacement.

The model is developed by considering only the momentum transfer of fluid mass, M_p, impinging upon a semi-infinite flat plate with a normal velocity of V_n. The fluid mass will initially be considered as a cylinder with equivalent mass to a sphere of the same diameter (Figure 44) so that the impinging cross section is constant, and the average force, F_n, is:

$$\overline{F}_n = \frac{d (m_p V_n)}{dt} = m_p \left(\frac{\overline{\Delta V_n}}{\overline{\Delta t}} \right) \tag{1}$$

38

Since the target does not deform and the projectile has no elastic properties (no rebound), the average contact time $\overline{\Delta t}$ is taken equal to the projectile diameter, D, divided by the normal velocity, V_n:

$$\overline{\Delta t} = \frac{D}{V_n} \qquad (2)$$

The average change in normal velocity, $\overline{\Delta V_n}$, is taken equal to $-V_n$, since the final normal velocity is assumed to be zero. Expressing the mass in terms of density (Figure 44), and substituting the above yields:

$$\overline{F}_n = \frac{-\pi}{6} \rho D^2 V_n^2 \qquad (3)$$

Defining the average contact pressure, $\overline{P}_n$, as the average force divided by the cross sectional area of the impinging fluid cylinder yields:

$$\overline{P}_n = \frac{-2}{3} \rho V_n^2$$

The above equations assume no rebound as do the solutions to the two previous models, and therefore can be considered as a minimum values for the case of a semi-infinite target. The effect of target compliance may be approximated by assuming that the actual impact time $\overline{\Delta t}$ is increased by the additional time required for the projectile to traverse the distance which the beam has deflected during the impact, δ:

$$\overline{\Delta t} = \frac{D + \delta}{V_n} \qquad (5)$$

Estimates of the beam displacement are available from the modified Hertz analysis.

The actual calculations of force and pressure used to simulate the Task I, Part A impacts are based upon spherical projectile geometry, resulting in a parabolic function of instantaneous force as a function of time.

These equations represent minimum values for force and load irrespective of any projectile mechanical properties, and reveal that for deformable projectiles:

- Force increases with the density to the first power, and with the diameter and velocity squared,

- Duration of the impact force is directly related to projectile size, and inversely related to projectile velocity, and

- Pressure is independent of projectile size, increasing with density to the first power, and velocity to the second power.

These observations predict that:

(1) gelatin should be more damaging than ice due to its 9 percent higher density

(2) since contact pressure is a function of velocity squared, even ice projectiles should exhibit a penetration threshold at a sufficiently high velocity.

f.   Impact Parameters

The response of graphite-epoxy composite specimens to normal impacts can be divided into four regions delineated by three thresholds (Figure 45). Below a certain critical velocity the target response is all elastic, and no discernible damage results. As the projectile velocity is increased, a damage threshold is achieved where the impact tensile stress waves exceed the composite through thickness tensile strength S_{33T}, and stress wave delaminations and cracking are visible. Further increases in projectile velocity result in contact stress exceeding the through thickness compressive strength S_{33C} of the material, resulting in localized penetration. At high impact energies using large projectiles, specimen fluxural failure occurs due to large deflections caused by the impact, before penetration can occur. The criteria for impact damage and the above observed failure types are summarized below:

CRITERIA FOR IMPACT DAMAGE

DAMAGE REGION:	Damage Threshold – Stress Wave Damage	Penetration Threshold – Increasing Penetration	Flexural Failure
CRITERION:	Tensile Stress Waves Exceed S_{33T}	Projectile/Target Contact Pressures Exceed S_{33C}	Deflection Exceeds Beam Flexural Strength
OBSERVED FAILURES:	Delamination, Splitting, Cracking	Indentation, Broken Fibers	Fracture, Gross Delamination

The Hertz model, modified Hertz model, and momentum-impulse model assumptions were utilized to predict the force as a function of time histories (loading functions) and contact times for the Task I, Part A, impact conditions. These results are summarized in Table XXIV and Figures 46 through 50. The Hertz calculations were performed for all impacts to serve

as a standard reference. The modified Hertz,and momentum-impulse calculations were not made for the higher velocity steel impacts, as the assumption of elastic target response was clearly invalid for these penetrative conditions.

The maximum load calculations summarized in Table XXIV reveal that the Hertz assumptions lead to the highest peak loads under all conditions simulated from Task I, Part A. Relaxation of the semi-infinite target assumption in the modified Hertz program resulted in lower loads than the Hertz values, and higher than the minimum momentun-impulse calculated loads, as was expected. The highest maximum loads among the ice and gelatin impacts result from impacts with 2.54 cm diameter projectiles at 152 m/sec (500 ft/sec), and from the 1.27 cm diameter projectiles at velocities of 274 m/sec (900 ft/sec) and above. The duration of these stresses is much longer for the 2.54 cm diameter projectiles than for the 1.27 cm diameter projectiles, as can be seen from the contact time results in Table XXIV.

The shape of the loading curve is shown for several representative impacts in Figures 46 through 50. Figure 46 shows force as a function of time for the case of 1.27 cm diameter gelatin impacting a $[(\pm 45_2)| 0_{12} |(\mp 45)_2]_T$ Modmor II/PR-286 cantilevered beam at 152 m/sec (500 ft/sec). The curve for the modified Hertz analysis is similar in shape to the Hertz curve, but predicts a 27 percent lower maximum stress. The momentum-impulse analysis predicts an impact duration 23 μ sec longer than the 30μ sec predicted by the Hertz program, with resultant maximum load of only 33 percent of the Hertz calculations. The actual bounds of the loading curve function for this impact are therefore between 33 percent and 73 percent of the Hertz load, depending upon whether the gelatin impacts as a fluid (no rebound), or impacts elastically (56 m/sec rebound velocity).

Load curves for 1.27 cm diameter gelatin and ice projectiles at 274 m/sec are shown in Figures 47 and 48 respectively. At the higher velocity the impact times for all models agree closely, varying from 64 to 71 μsec for the gelatin, and 62 to 66 μ sec for the ice impact. The bounds of the loading curve for the gelatin impact vary from 45 percent of the Hertz load for the fluid projectile properties, to 72 percent of the Hertz load if the gelatin behaves elastically. For the ice, the upper elastic load bound is 72 percent of the Hertz load, while the lower bound is 43 percent of the Hertz load. The upper bound peak loads are nearly identical for these two impacts, 10.9 x 10^3 Newtons (2460 lbf) for gelatin and 10.9 x 10^3 Newtons (2450 lbf) for ice, but observation of high speed photography with ice impacts reveals early shattering leading to near-fluid behavior during impact, indicating that the lower bounds of 6.45 x 10^3 Newtons (1450 lbf) is more reasonable for the ice. Results from Task I Part A also show lower damage extents for a given impact energy with ice when compared to gelatin.

Loading curves for 2.54 cm diameter gelatin projectiles at 61 m/sec (200 ft/sec) and 152 m/sec (500 ft/sec) are shown in Figures 49 and 50 respectively. The upper and lower load bounds are 39 percent and 13 percent of the Hertz load at 61 m/sec, and 37 percent and 24 percent of the Hertz load at 152 m/sec. These results show that the error in the load calculation due to the assumption of a semi-infinite target becomes more severe as the ratio of projectile to target mass is increased. An interesting aspect of the load curves for the 2.54 cm diameter projectiles (including steel and ice, not shown) is that multiple impacts result if completely elastic behavior is assumed. This implies that the combination of vibratory

modes (the solution of the integral equation assumes that the first 25 modes are involved in the motion) excited by the original impact would cause the beam to rebound away from the projectile at a velocity greater than its residual forward velocity, causing momentary separation.

2. Deflections

The vertical deflections of a transversely impacted beam are a function of both the magnitude and duration of the impact loads. The modified Hertz loading function was therefore used to determine beam deflections as a function of time and position for a 5.1 cm (2 inches) wide by 0.25 cm (0.100 inches) thick by 20.3 cm (8.0 inches) long cantilevered beam impacted at a point 8.9 cm (3.5 inches) from the fixed end. A bending modulus of 42.0 GN/m² (6.1 x 10⁶ psi) was utilized to simulate the bending modulus of the $[(\pm 45)_2 \mid 0_{12} \mid (\mp 45)_2]_T$ Modmor II/PR-286 composite specimens utilized in Task I, Part A. The beam vertical deflections were calculated at locations 5.1 cm (2.0 inches), 10.2 cm (4.0 inches), 15.2 cm (6.0 inches) and 20.3 cm (8.0 inches) from the fixed end. These deflections plus the boundary condition that the slope of the beam at the fixed end must approach zero at the point of attachment were used to construct the beam shape as a function of location and time. The constructions resulting from the loading curves given in Figures 46 through 50 are shown in Figures 51 through 55. The vertical and horizontal scales are plotted on a 1:1 scale, to give a realistic view of the beam deflections. The beam shape is shown at five times: prior to impact; at the termination of impact (or of the initial impact in the case of multiple impacts); at 424 μ sec; at 1270 μ sec; and at 1800 μ sec. The deflections shown assume elastic projectile behavior, and are more severe than the actual impacts to the extent that the real projectile behaved as a fluid with no rebound.

The beam deflections as a function of time are shown for 1.27 cm diameter gelatin at 152 m/sec, 1.27 cm diameter gelatin at 274 m/sec, and 1.27 cm diameter ice at 274 m/sec in Figures 51, 52, and 53, respectively. In all three cases, the mid-span beam location nearest the impact point is initially deflected downward (impact assumed coming down onto beam) at the end of the impact, while the quarter-span and three-quarter-span locations are unmoved, and the tip is deflected slightly upwards. The mid-span deflections at this time are 0.294 cm (0.116 inch) for the 152 m/sec gelatin impact, 0.490 cm (0.193 inch) for the 274 m/sec gelatin impact, and 0.440 cm (0.173 inch) for the 274 m/sec ice impact. Deflection at 424 μ sec progresses downward (positive) at quarter, half and three quarter span, while the tip continues upward, giving the beam a concave upward bow. At 1270 μ sec, the first three span location deflections have changed only slightly, but the tip deflection is now more positive than the three-quarter span location. At 1800 μ sec, the quarter-span deflection is negative (upward), with the remaining three locations progressively more positive, in what appears like a second bending mode deflection. This is in agreement with the Task I Part A results which observed second bending response in all specimens after the initial impact transients had damped out. The tip deflections at 1800 μ sec are 2.60 cm (1.04 inches) for the 152 m/sec gelatin impact, and 4.78 cm (1.88 inches) and 4.35 cm (1.71 inches) for the 274 m/sec gelatin and ice impacts, respectively.

Deflections as a function of time are shown for the case of 2.54 cm diameter gelatin at 61 m/sec (200 ft/sec) in Figure 54, and at 152 m/sec (500 ft/sec) in Figure 55. Initial deflections for the 2.54 cm diameter impacts are similar to those for the smaller projectiles. The mid-span position exhibits a positive deflection of 0.73 cm (0.29 inch) at 61 m/sec, and 1.55 cm (0.61 inch) at 152 m/sec, while the remainder of the beam is relatively undisturbed, exhibiting small positive deflections at quarter-span and tip, and a small negative deflection at three-quarter span. The deflection constructed in Figure 55 for gelatin at 152 m/sec bears strong resemblance to the actual shape of a composite Task I, Part A, specimen being deformed by such an impact in Figure 8, right. The beams then take on a concave upward shape at 424 μ sec, but do not assume the final appearance of second bending at 1800 μ sec. Instead the entire beam exhibits positive deflections. The final tip deflection resulting from the 61 m/sec impact is 2.97 cm (1.17 inches), and is comparable to that for the 1.27 cm diameter impacts in Figures 51 through 53. The back face of this specimen at the point of impact remains in a convex shape until approximately 1800 μ sec. Strain gages on this face should, therefore, have indicated tension until this time. This is in good agreement with the strain record for specimen 982-2 impacted with 2.54 cm diameter gelatin at 68 m/sec as shown in Figure 11. The deflections shown resulting from the 152 m/sec impact in Figure 55 are clearly more severe than those shown in the previous figures, and indicates why tests with 2.54 cm diameter gelatin and ice projectiles at this velocity resulted in flexural failure of the specimens. At 1800 μ sec midspan deflection is 6.53 cm (2.57 inches) and tip deflection is 8.25 cm (3.25 inches). Fitting a radius of curvature to the mid-span bending shape yields a radius of 4.7 cm (1.85 inches) over a 5 cm length of the beam. Using the formula for skin strain on a beam due to bending around a radius:

$$\epsilon = \frac{t}{2\ell}$$

where t = beam thickness
ℓ = radius of curvature

yields ϵ = 2.7 percent, which is far in excess of the yield strain of the Modmor II/PR-286 composite material.

3.   Contact Stresses

The calculations of maximum impact projectile/target compressive stresses are summarized in Table XXV. These pressures were arrived at using (Reference 1):

$$q = \frac{-3P}{2 \pi a^2}$$

where P is the load and a is the radius of the area of contact.

for the Hertz program, and

$$q = \frac{3}{2\pi} \sqrt[3]{\frac{16}{9\pi^2} \cdot \frac{P}{R^2(K_c^2 + K_p^2)}}$$

for the modified Hertz program. The momentum-impulse pressure calculation is derived by dividing the maximum load by the projectile cross-sectional area.

The ease with which steel projectiles penetrate the Modmor II/PR-286 composite is seen in the very high contact stress generated at the interface. Using the modified Hertz calculation which is reasonably valid for the low velocity steel impacts yields contact pressures of 2040 MN/m^2 (296 ksi) for the 0.64 cm diameter steel at 61 m/sec (200 ft/sec) and 1680 MN/m^2 (244 ksi) for 1.27 cm diameter steel at 30 m/sec (100 ft/sec). These pressures are easily in excess of the S_{33c} compressive strength of the composite, which is approximately 138-241 MN/m^2 (20-35 ksi in low strain rate tests).

The maximum pressures using the modified Hertz program exceed 138 MN/m^2 (20 ksi) in four instances: 1.27 cm diameter gelatin at 274 m/sec (147 MN/m^2); and 1.27 cm diameter ice at 214 m/sec (150 MN/m^2), 274 m/sec (166 MN/m^2), and 305 m/sec (173 MN/m^2). The fact that only the gelatin projectiles caused penetration damage at the impact face in Task I, Part A, is further evidence that the gelatin behaves more elastically (and hence closer to the upper bound of the loading curve) than does the ice. This quasi-fluid behavior of the ice would thus indicate that ice presents less of a ballistic impact threat than do birds, assuming that the viscoelastic response of real birds is fairly approximated by the response of the gelatin spheres used in Task I.

4. Application to Turbine Engine Blading

Application of the Task I results to the simulated blade testing of Task II and to turbine engine blading is accomplished by resolving actual impacts into their normal and tangential components, as shown in Figure 56. It has been demonstrated in Task II that the tangential component of ice and gelatin impacts does not cause any measurable damage in $0°$-LE impacts at 274 m/sec. Relating the normal component of the Task II impacts to the normal impact damage and penetration thresholds established for $[(\pm45)_2 \mid 0_{12} \mid (\mp45)_2]_T$ Modmor II/PR-286 composite in Task I, Part A, furthermore indicates that the normal components in Task II for ice and gelatin projectiles are below the damage thresholds, as shown in Table XXVI. Metallography of Task II specimens impacted at $15°$-QC showing no damage confirmed this prediction for one case, and impacts at $30°$-LE revealed only bending damage and no stress wave damage. All Task II impacts with steel against unprotected composite resulted in severe stress wave damage. Thus the resolution of the vector velocity components appears to be valid.

Knowing the damage threshold of a particular projectile type at the limiting case of normal impact, and using the relationship that $v_n = V \sin \alpha$ from Figure 56, it is possible to define

44

the range of blade operating parameters above which stress wave damage will occur, and below which no stress wave damage will occur. This is accomplished by plotting the locus of points where $v \sin \alpha$ equals the normal impact damage threshold velocity. This is shown for 1.27 cm diameter gelatin in Figure 57, 1.27 cm diameter ice in Figure 58, and for 1.19 cm diameter steel in Figure 59. The range of leading edge impact angles and velocities for a typical fan blade at take off conditions is included for reference on the three figures. Figures 57 and 58 show that the entire range of fan operating conditions falls outside of the stress wave damage threshold region, indicating that no stress wave damage should result to Modmor II/PR-286 composite blade material due to impacts with these projectiles. This further indicates that damage due to leading edge impacts with the ice and gelatin projectiles is the result of structural failure of the relatively thin leading edge due to the high loads imposed by the impact. Work conducted in Task I indicates that gelatin impacts may cause higher loads than ice impacts due to more elastic behavior and due to higher density, indicating that for a given mass, bird impacts may be more severe than ice impacts.

The typical fan blade take off parameters fall entirely within the damage and penetration threshold for steel in Figure 59, indicating that all steel impacts will cause penetration and stress wave damage. Experimental work in the Task II spin impact tests have demonstrated that severe wave damage does occur even in glancing impacts, and has also demonstrated that proper shielding can protect the composite. The leading edge FOD shield utilized in the Task II spin impact tests was successful in arresting steel impact without transmitting stress wave damage to the composite.

45
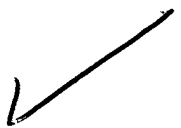
IV. CONCLUSIONS

The following conclusions have been drawn:

- Impacting projectiles cause decreasing damage in the following order: steel, gelatin, ice.

- Increased composite transverse tensile strength correlated with improved resistance to delamination damage.

- Addition of S-Glass and PRD-49-1 fibers to graphite composite resulted in increased impact resistance to cracking and delamination.

- Lay-ups using dispersed angled plies exhibited the best impact resistance to delamination damage.

- Residual tensile strength was an effective parameter in measuring damage caused by penetrative impacts but was not an effective measure of delamination type damage.

- Ultrasonic inspection and torsional modulus were the most effective measure of delamination type damage.

- In tapered simulated blade specimens damage severity increased with increasing impact angle for ice and gelatin impacts at the leading edge.

- Ply-layups resulting in increased leading edge stiffness, such as obtained by the addition of 90° surface plies, were effective in reducing impact damage.

- Metallic leading edge shields afforded protection to leading edge impacts with 0.64 cm diameter steel projectiles and 1.27 cm diameter ice and gelatin projectiles.

- Metallic leading edge shields provided protection against 2.54 cm diameter ice projectiles at 30° impingement angle to the leading edge but were not effective against gelatin projectiles.

REFERENCES

1. Bitter, J. G. A., "A Study of Erosion Phenomena, Parts I and II, Wear, 6, (1963)

2. Muguruma, J., "Effects of Surface Condition on the Mechanical Properties of the Crystals", British Journal of Applied Physics, 1969, Ser. 2, Vol. 2

3. Timoshenko, S., Zeitschrift fur Matematik und Physik, Vol. 62, 1913, p 198, Zur Frage mach der Wirkung Eines Stosses auf Einen Balken
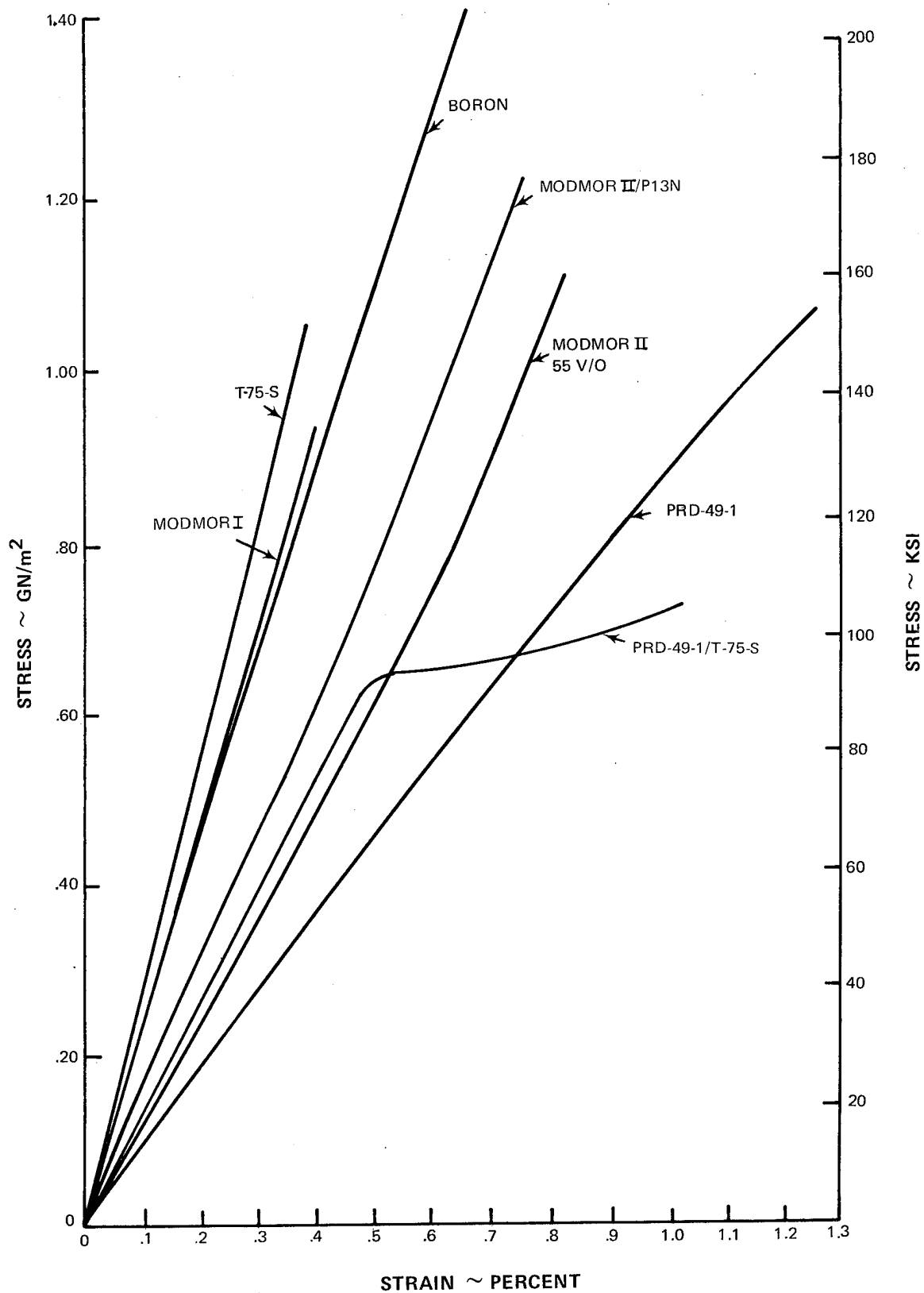
Figure 1   Typical Longitudinal Tensile Stress Versus Strain Curves for Unidirectionally
            Reinforced PR-286 Epoxy Composite Systems and the Modmor II/P13N
            Polyimide System
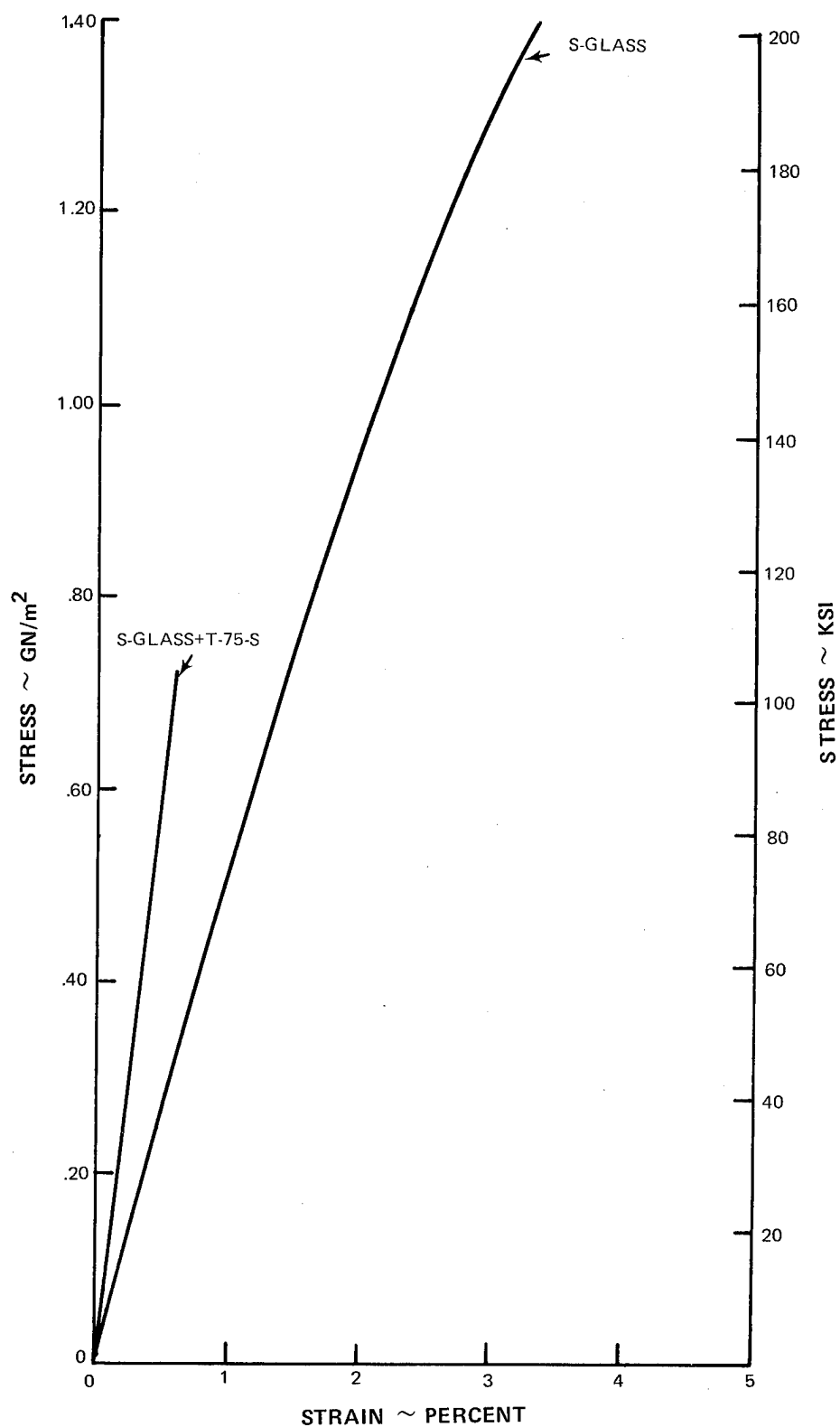
Figure 2   Typical Longitudinal Tensile Stress Versus Strain Curve for the Unidirectionally
Reinforced S-Glass/PR-286 and S-Glass plus T-75-S/PR-286 Epoxy Composite Systems

49
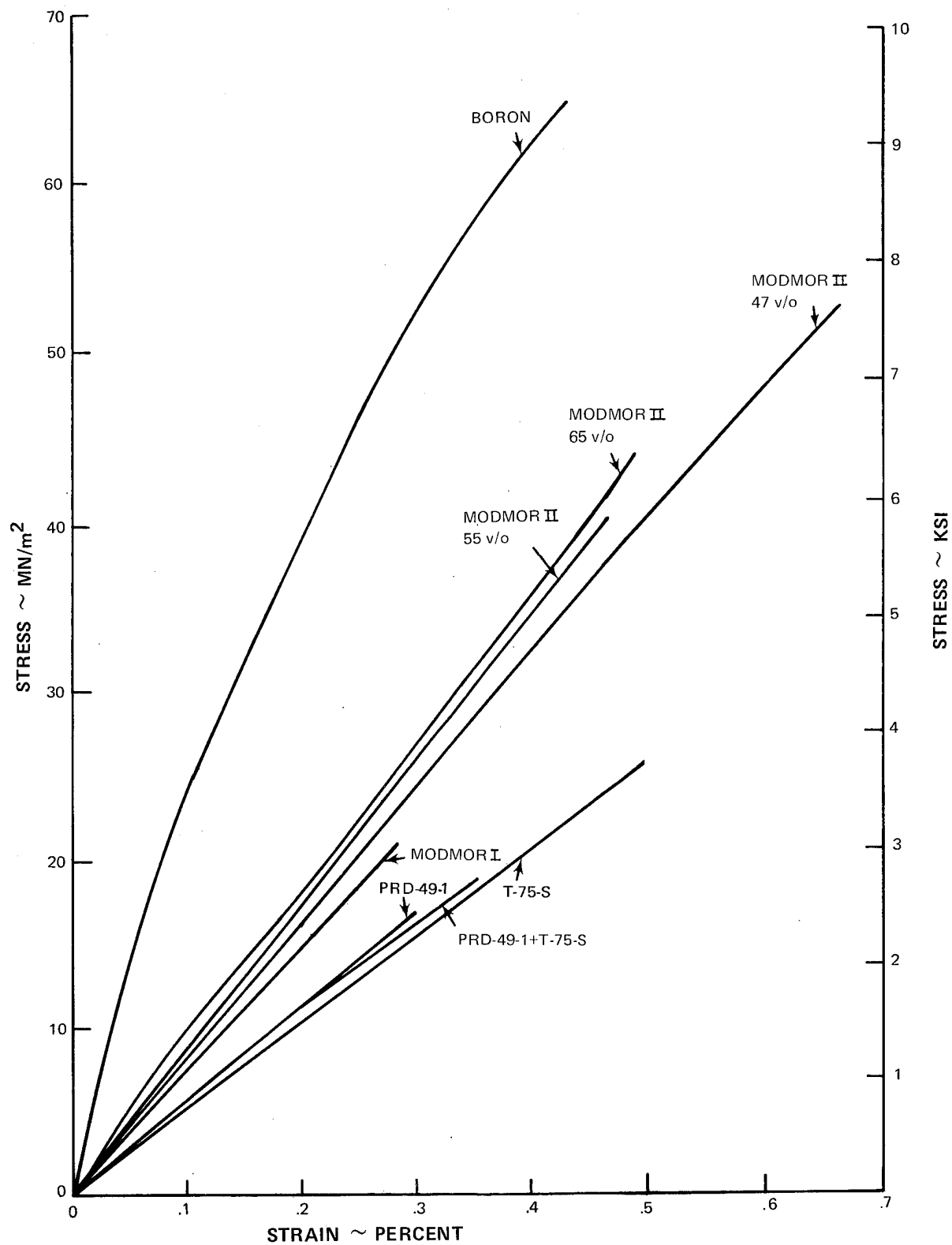
Figure 3   Typical Transverse Tensile Stress Versus Strain Curves for Unidirectionally
Reinforced PR-286 Epoxy Composite Systems
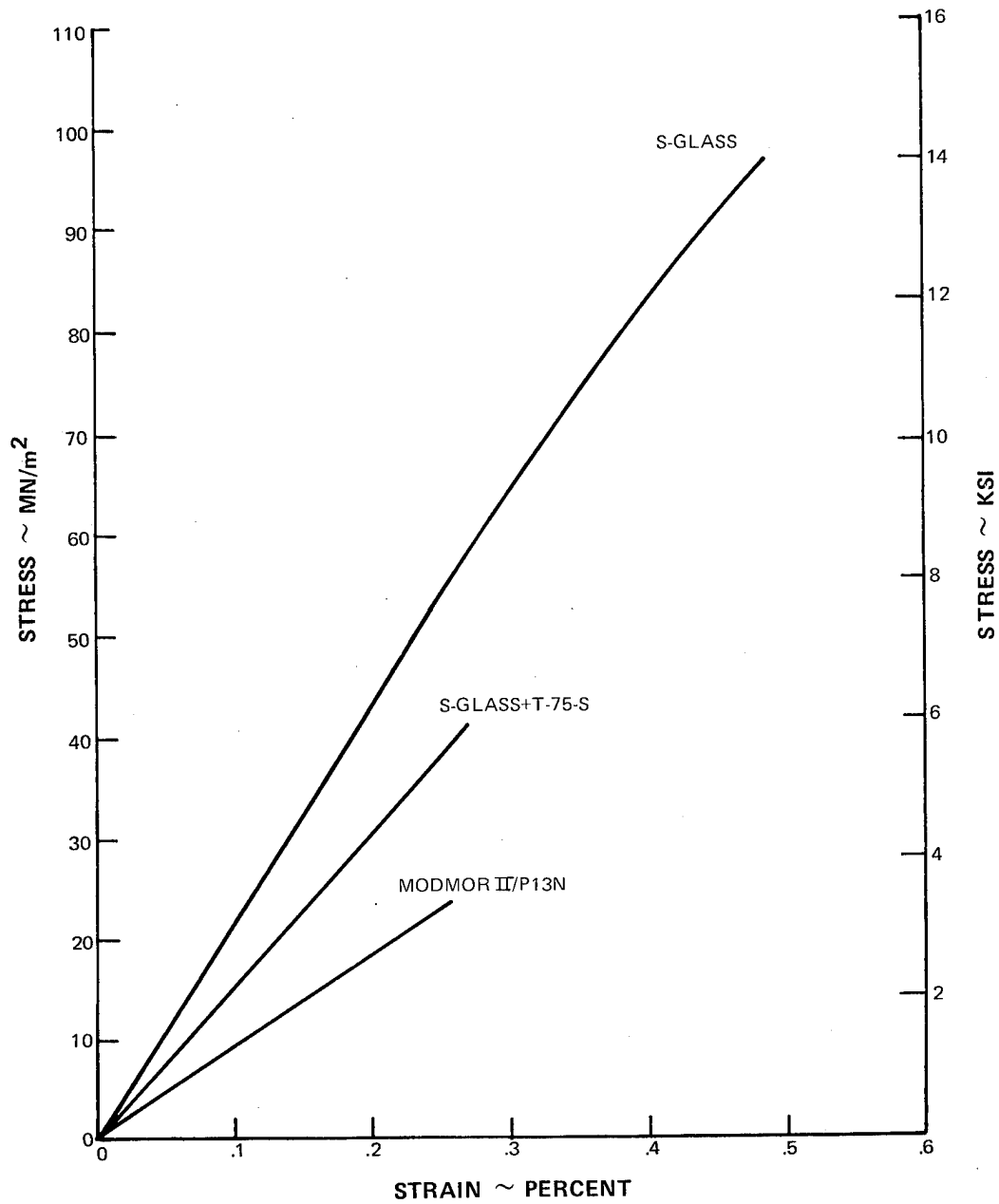
Figure 4   Typical Transverse Tensile Stress Versus Strain Curve for the Unidirectionally
Reinforced S-Glass/PR-286 and S-Glass plus T-75-S/PR-286 Epoxy Composite
Systems, and the Modmor II/P13N Polyimide System

51
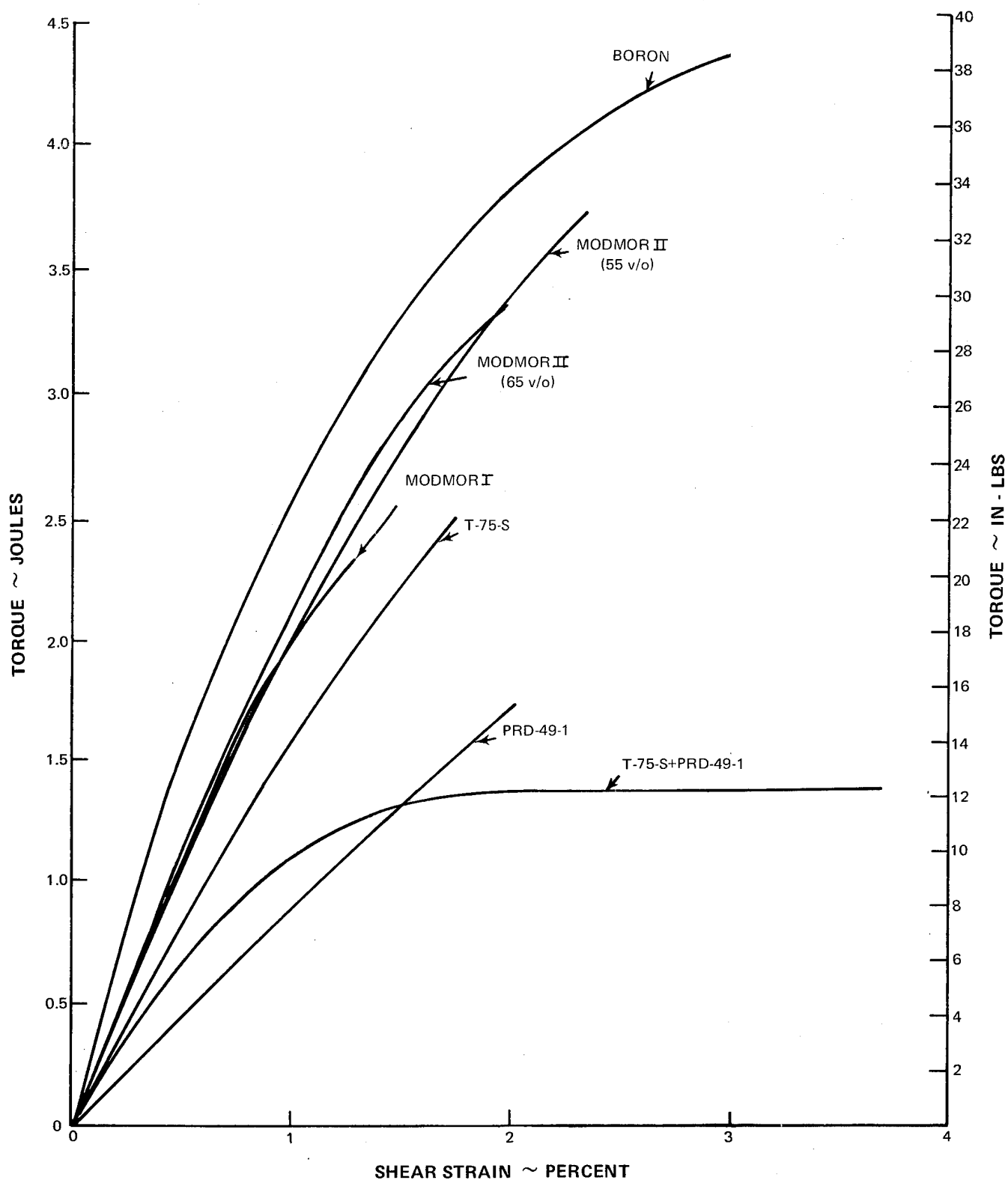
Figure 5   Typical Torque Versus Shear Strain Curves for Unidirectionally Reinforced
            PR-286 Epoxy Composite Systems
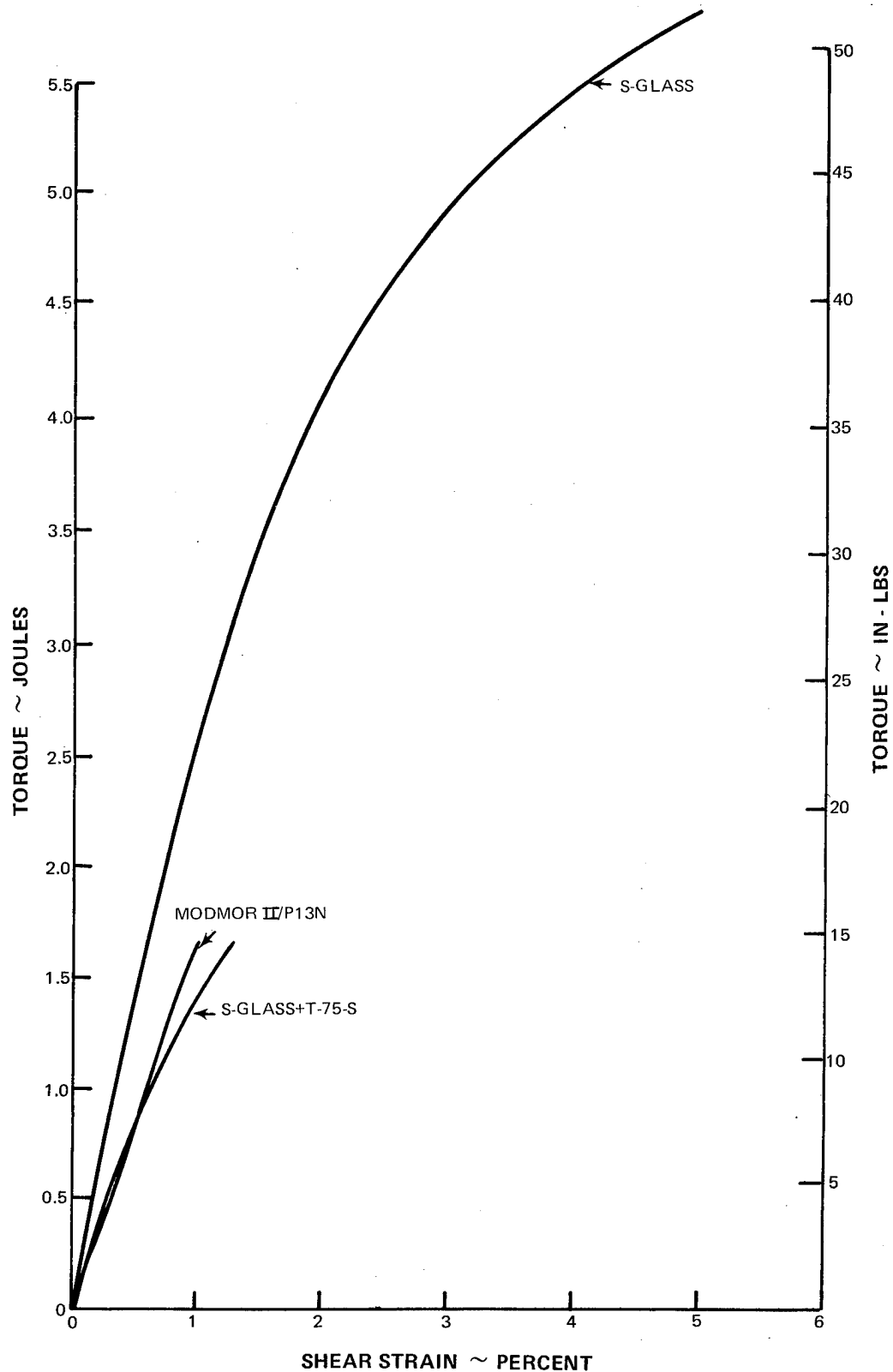
Figure 6   Typical Torque Versus Shear Strain Curve for the Unidirectionally Reinforced
S-Glass/PR-286, S-Glass Plus T-75-S/PR-286, and Modmor II/P13N Composite
Systems

53
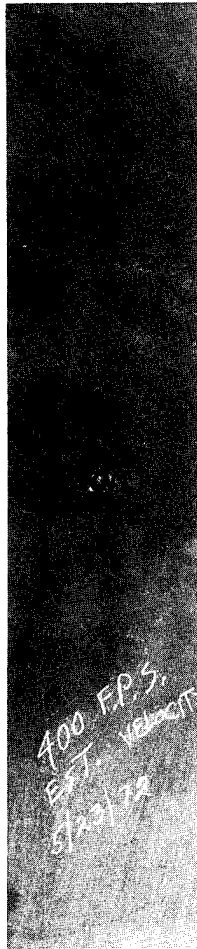
(H-96019) (H-96020)
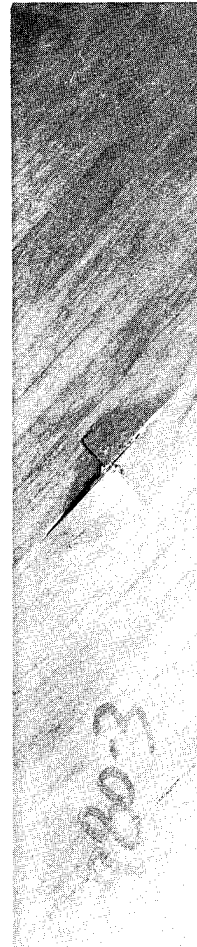
FRONT FACE BACK FACE

Figure 7 Front and Back Face Views of $[(\pm 45)_2 \mid 0_{12} \mid (\mp 45)_2]_T$ Modmor II/PR-286
Specimen After Impact With 0.64 cm Diameter Steel Ball at 122 m/sec

Mag:½X

54
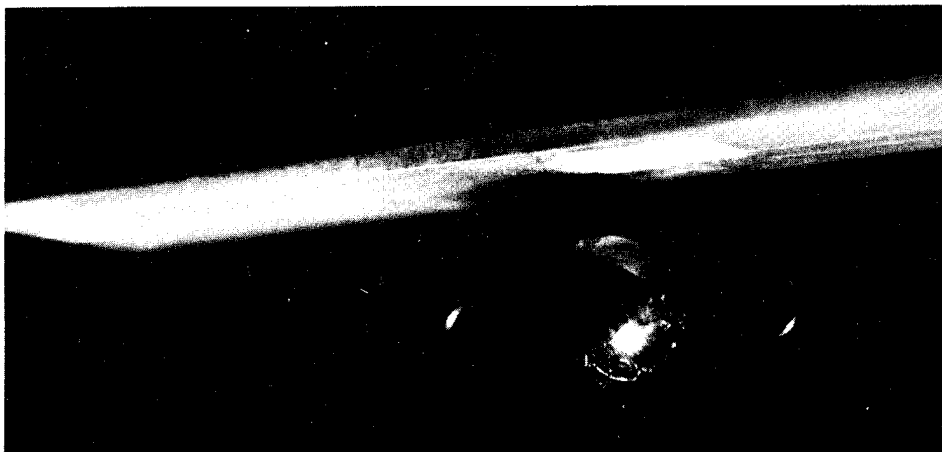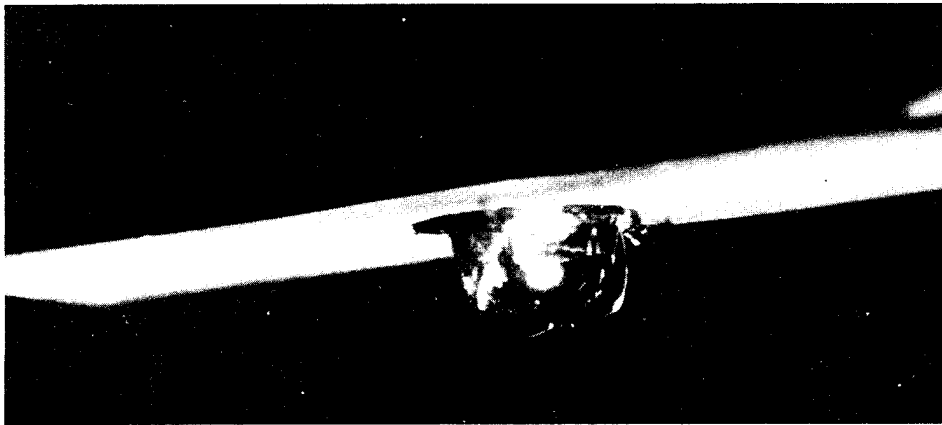
Figure 8   High Speed Strobe Photographs Showing Approach and Impact of a 2.54 cm Diameter Gelatin Ball

55
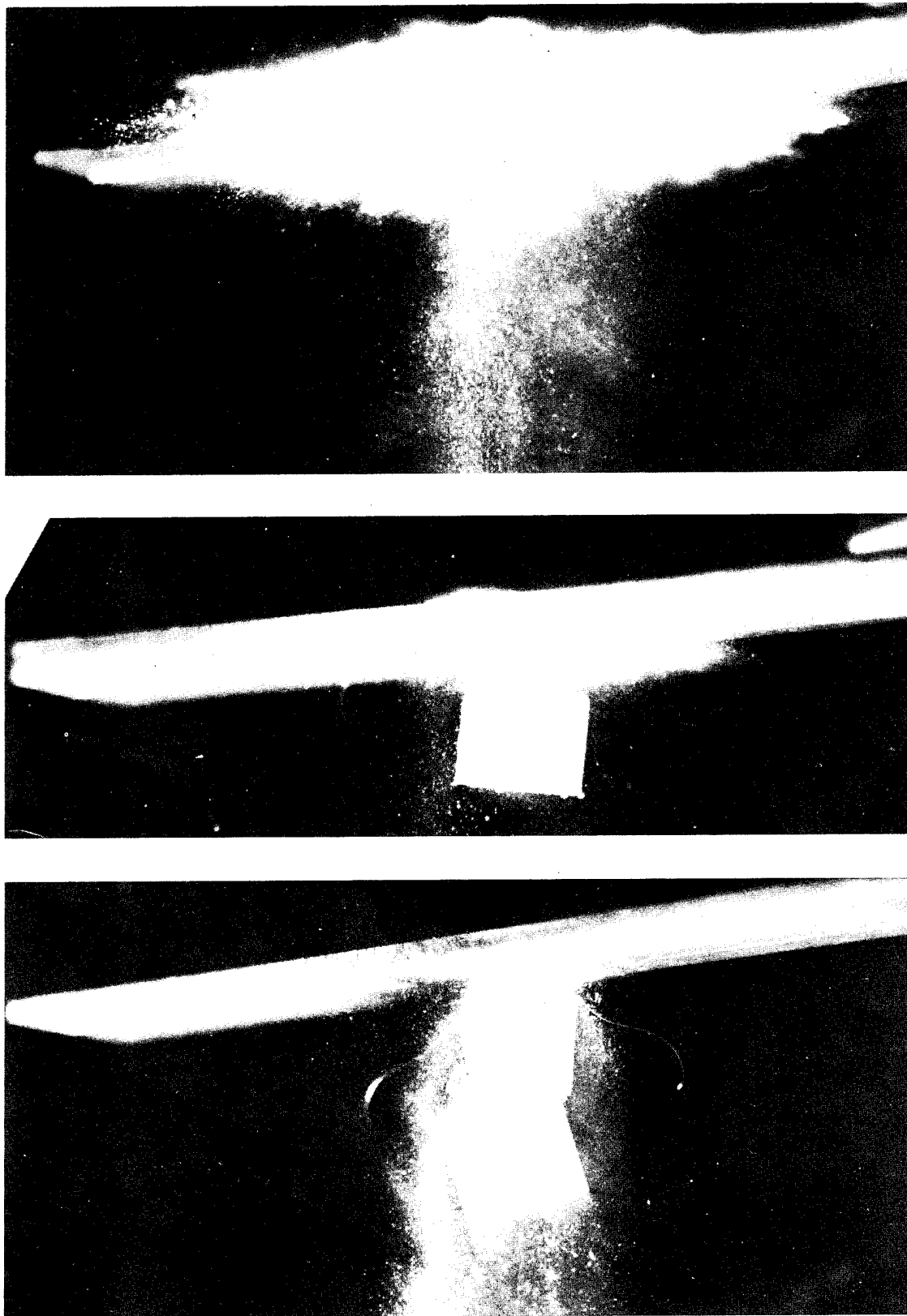
Figure 9   High Speed Strobe Photographs Showing Approach and Impact of a 2.54 cm
Diameter Ice Ball
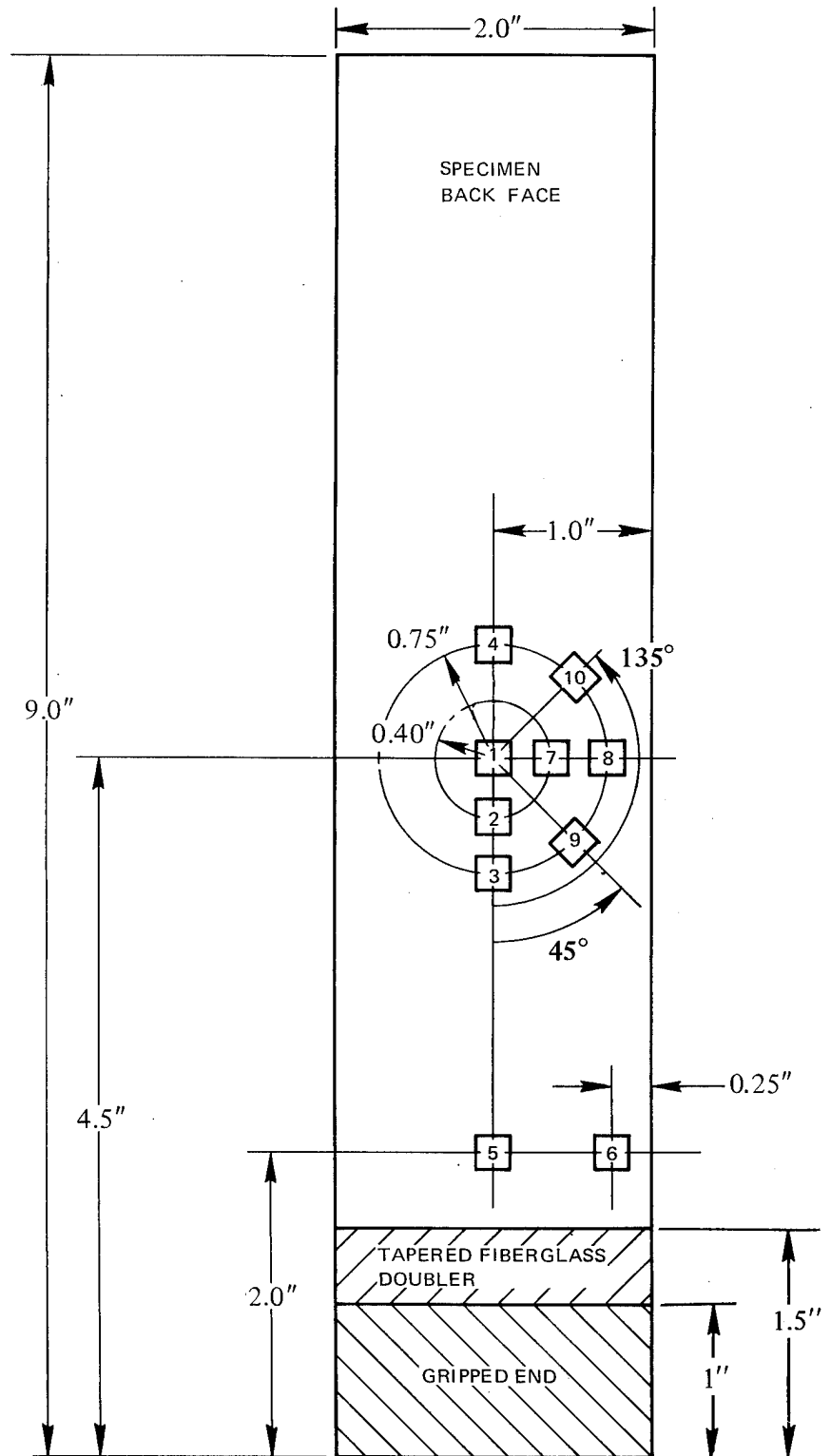
Figure 10   Location of Strain Gages on Task I Instrumented Impact Specimens
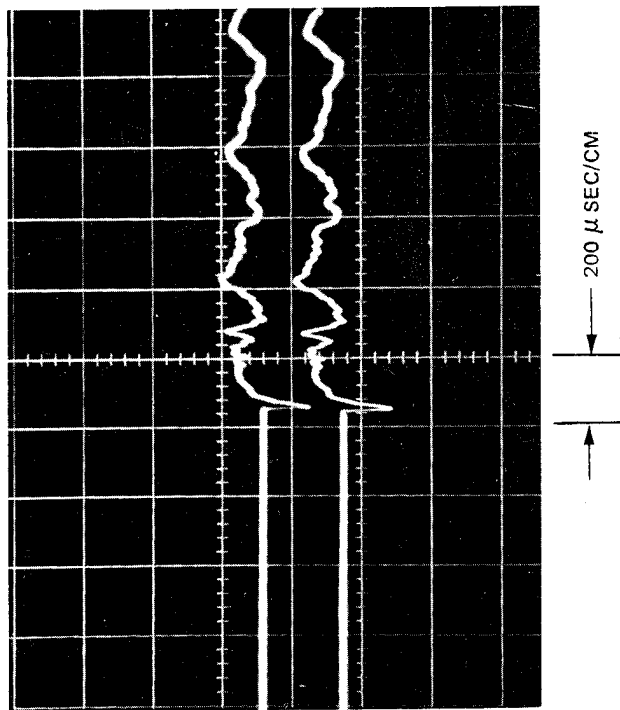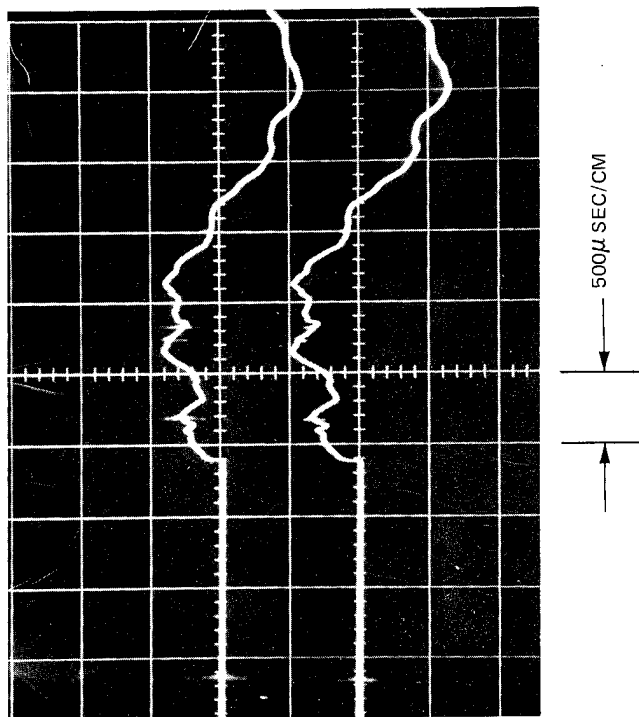
Figure 11   On Line Oscilloscope Photograph Comparisons of Dynamic Strain Response as a Function of Amplifier Frequency Response. Upper Traces Are Directly Through Oscilloscope (1000 KHz), While Lower Traces Have Passed Through Translator Amplifier (50 KHz)

C-SCAN

PHOTO LOCATION

NO DAMAGE

1012-2

MAG: ½X

IMPACT FACE
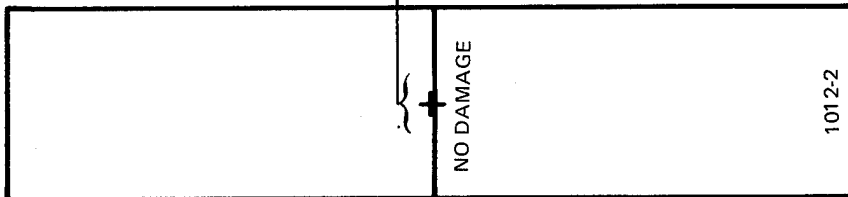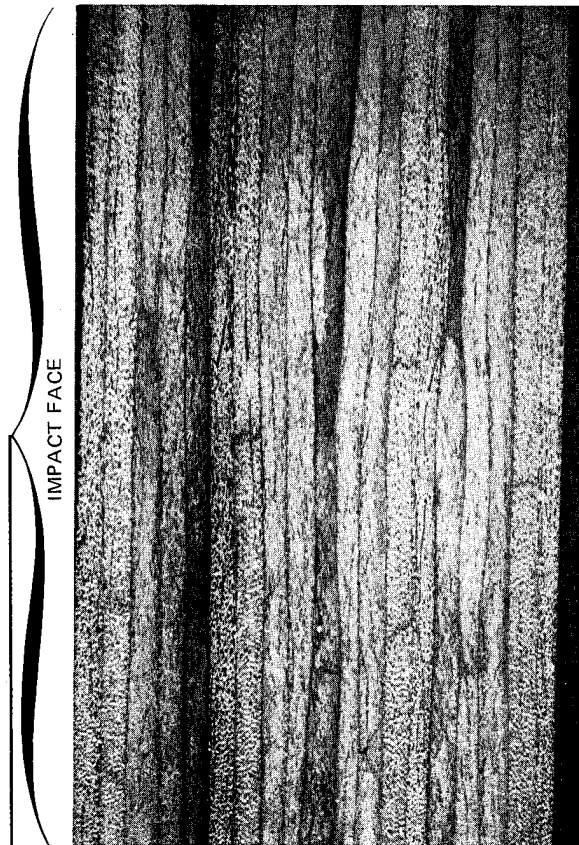
BACK FACE

MAG: 22X

Figure 12   Transverse Cross Section View of Modmor II/PR-286 Pseudo-Isotropic Layup Specimen After Impact With 1.27 cm Diameter Ice at 282 m/sec

C-SCAN

DAMAGED AREA

984-2

MAG: ½X

PHOTO LOCATION

IMPACT FACE

BACK FACE

MAG: 11X
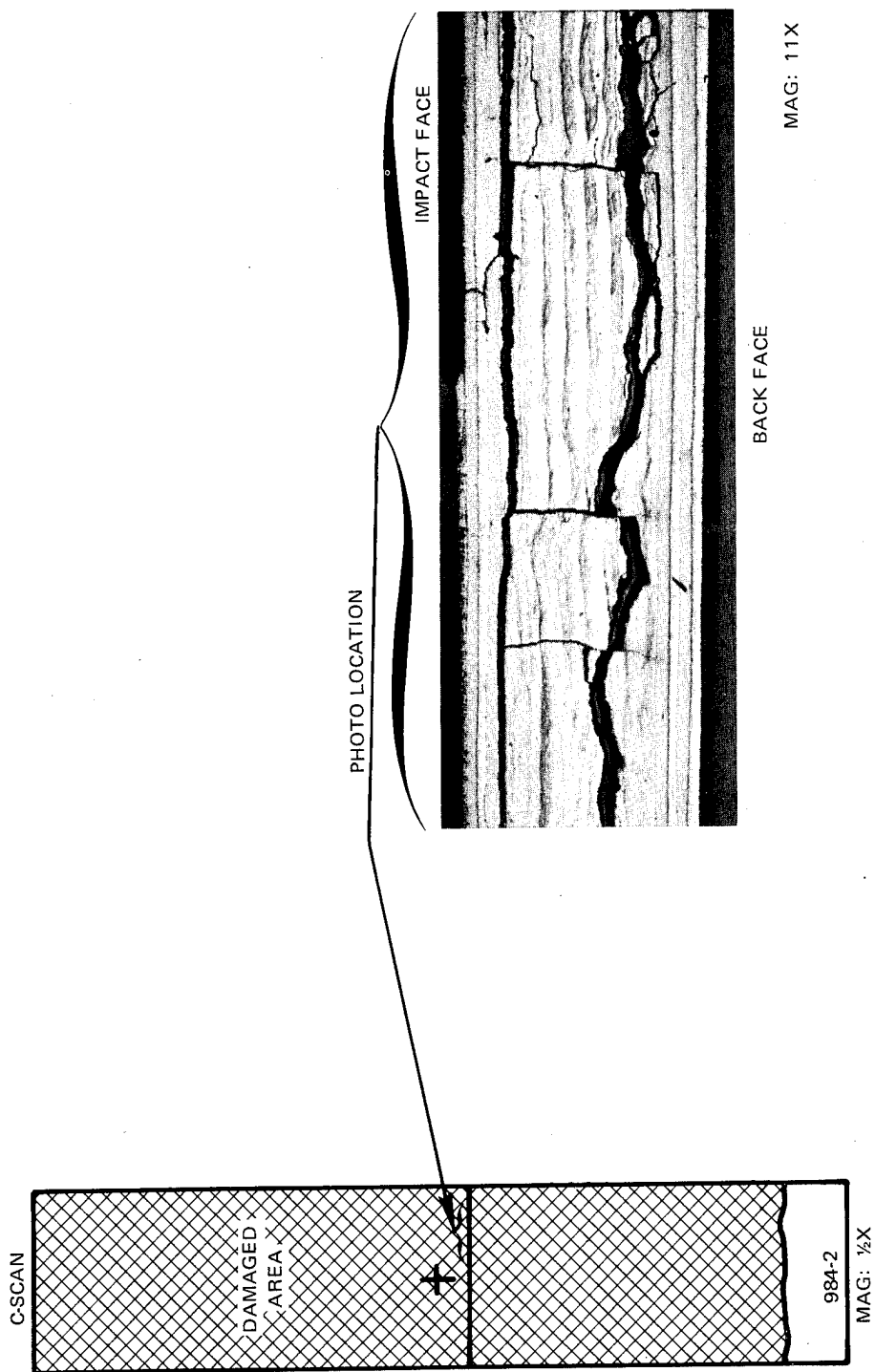
Figure 13   Transverse Cross Section View of $[(\pm 45)_2 | 0_{12} | (\mp 45)_2]_T$ Modmor II/PR-286 Specimen After Impact With 2.54 cm Diameter Gelatin at 107 m/sec
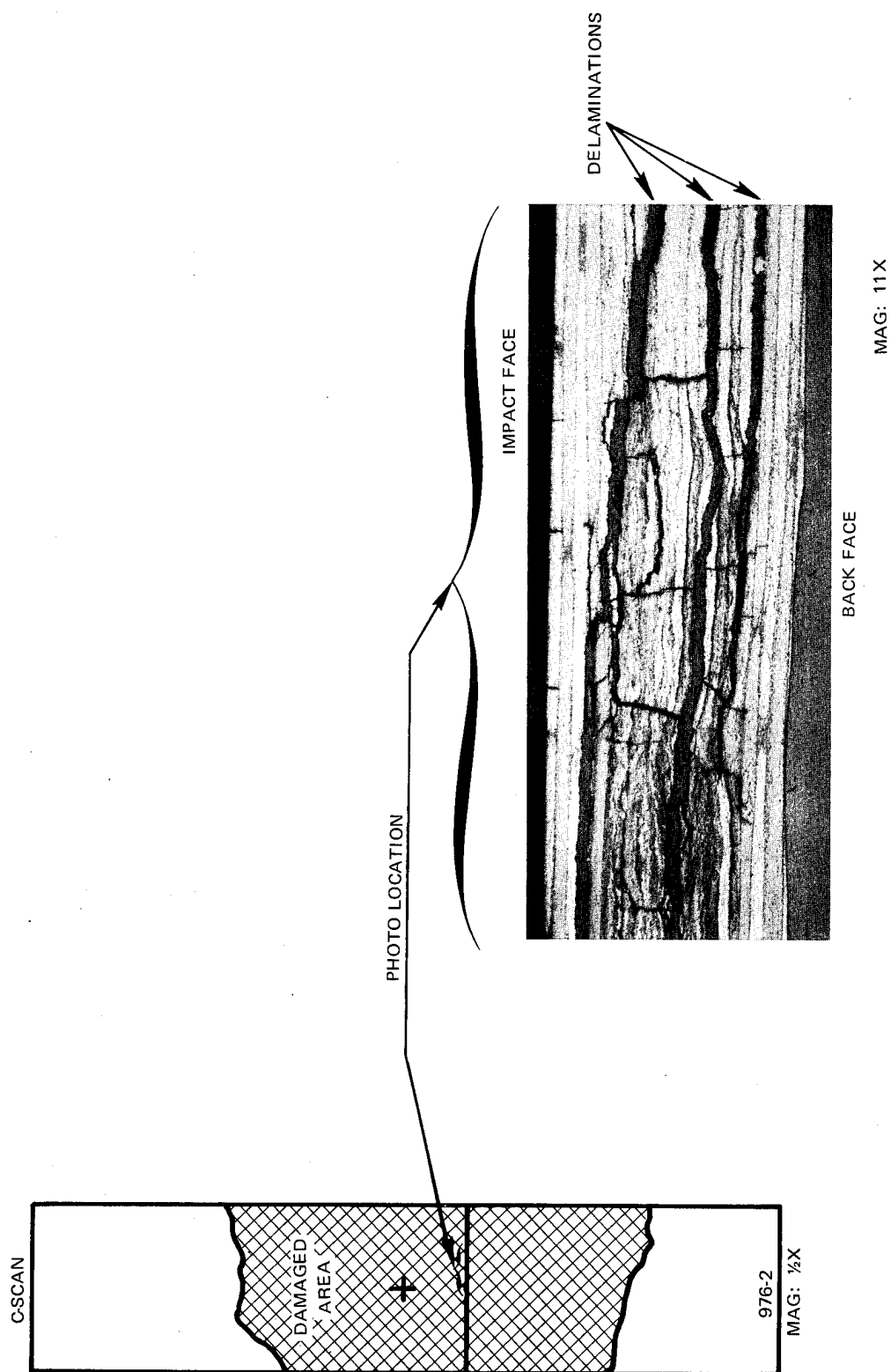
Figure 14   Transverse Cross Section View of $[(\pm45)_2 | 0_{12} | (\mp45)_2]_T$ Modmor II/PR-286 Specimen After Impact With 1.27 cm Diameter Gelatin at 274 m/sec. (Note Multiple Cracks and Delamination)

61

C-SCAN

DAMAGED AREA

PHOTO LOCATION

IMPACT FACE

BACK FACE

SCALE: ~3X

9824

MAG: ½X
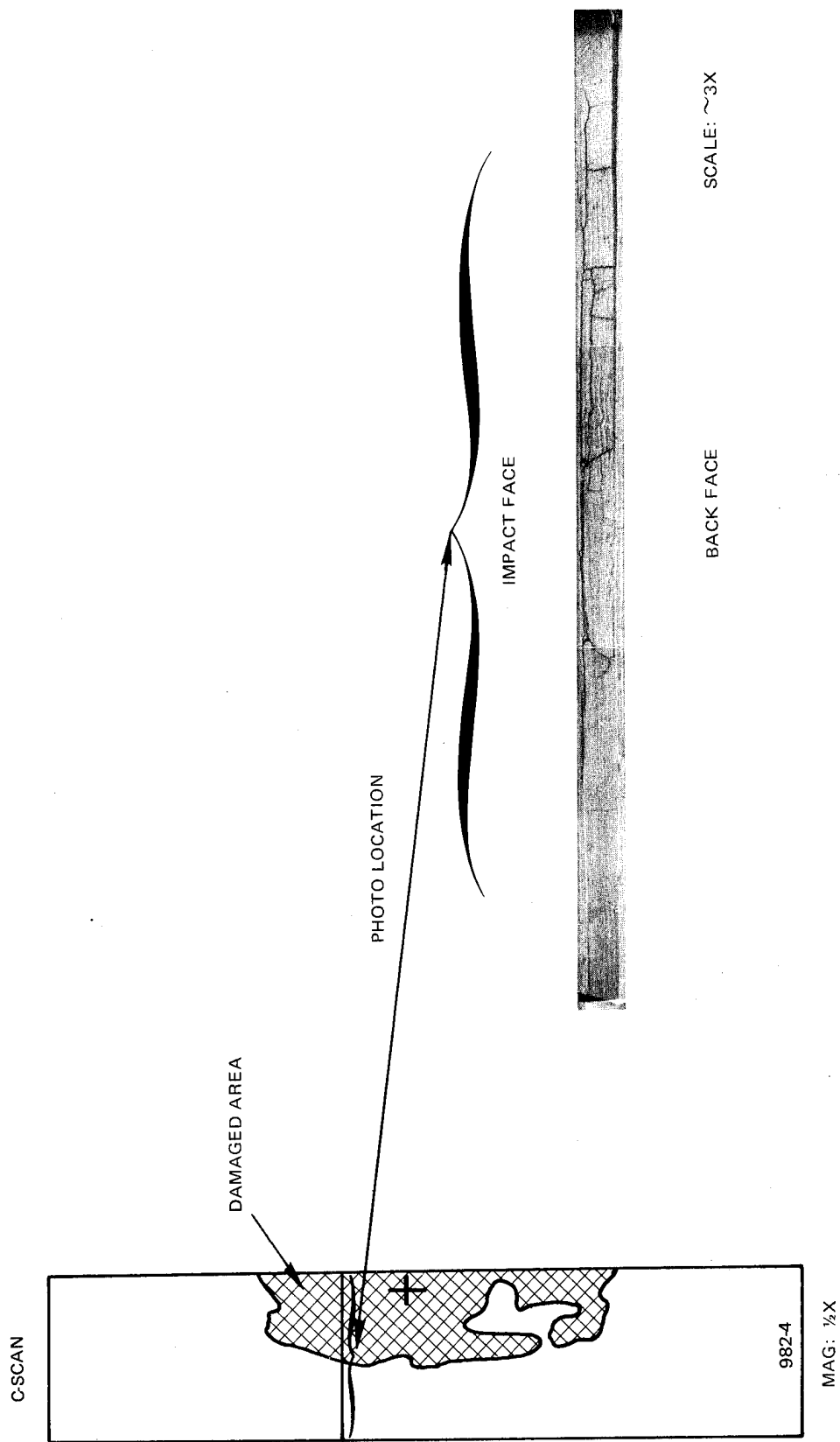
Figure 15 Transverse Cross Section View of $[(\pm 45)_2 \mid 0_{12} \mid (\mp 45)_2]_T$ Modmor II/PR-286 Specimen After Impact With 1.27 cm Diameter Ice at 279 m/sec
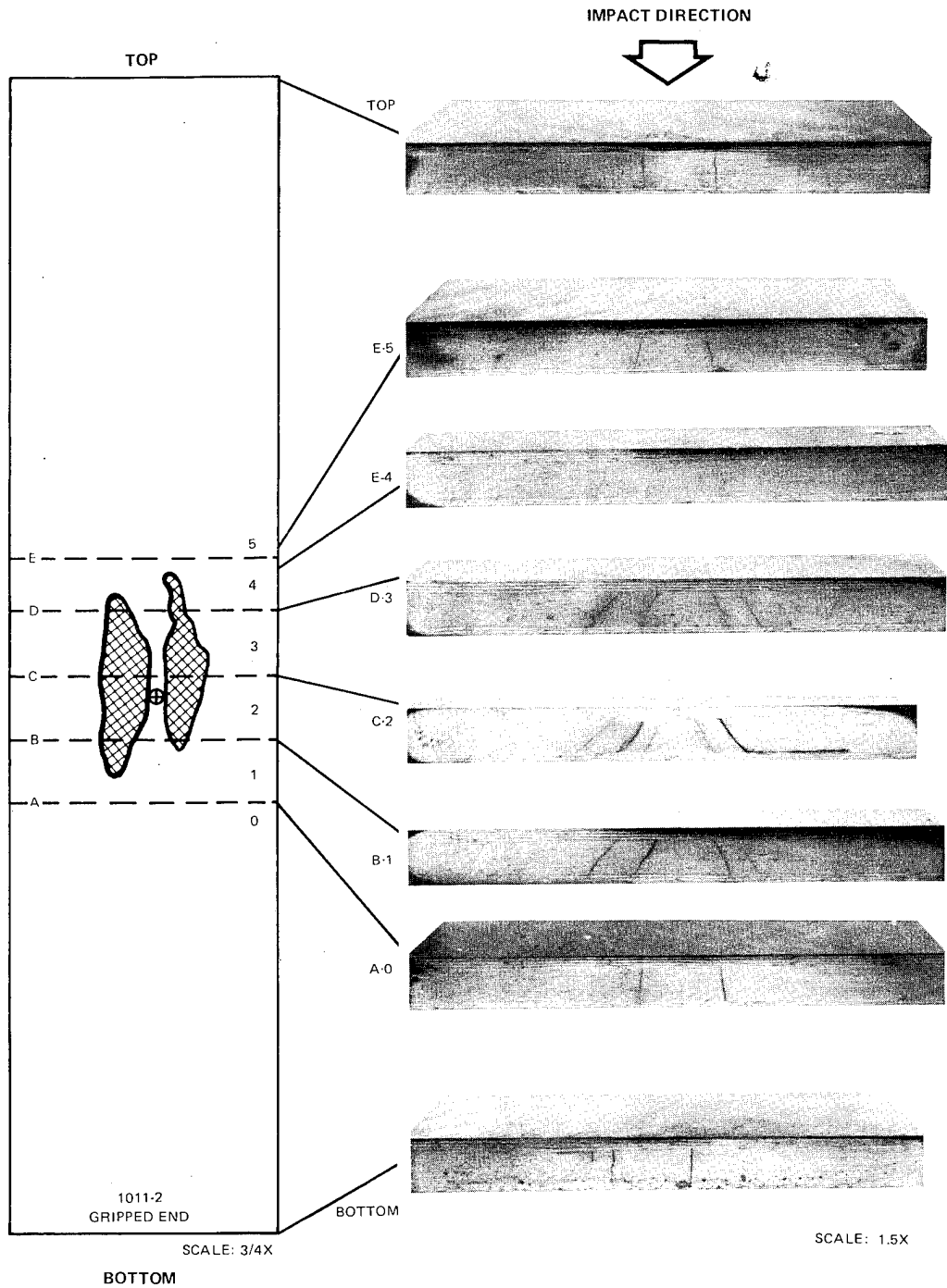
Figure 16   Comparison of Ultrasonic C-Scan Inspection With Transverse Metallographic Sections Taken From $[(\pm45)_4 |0_{24}| (\mp45)_4]_T$ Modmor II/PR-286 Specimen
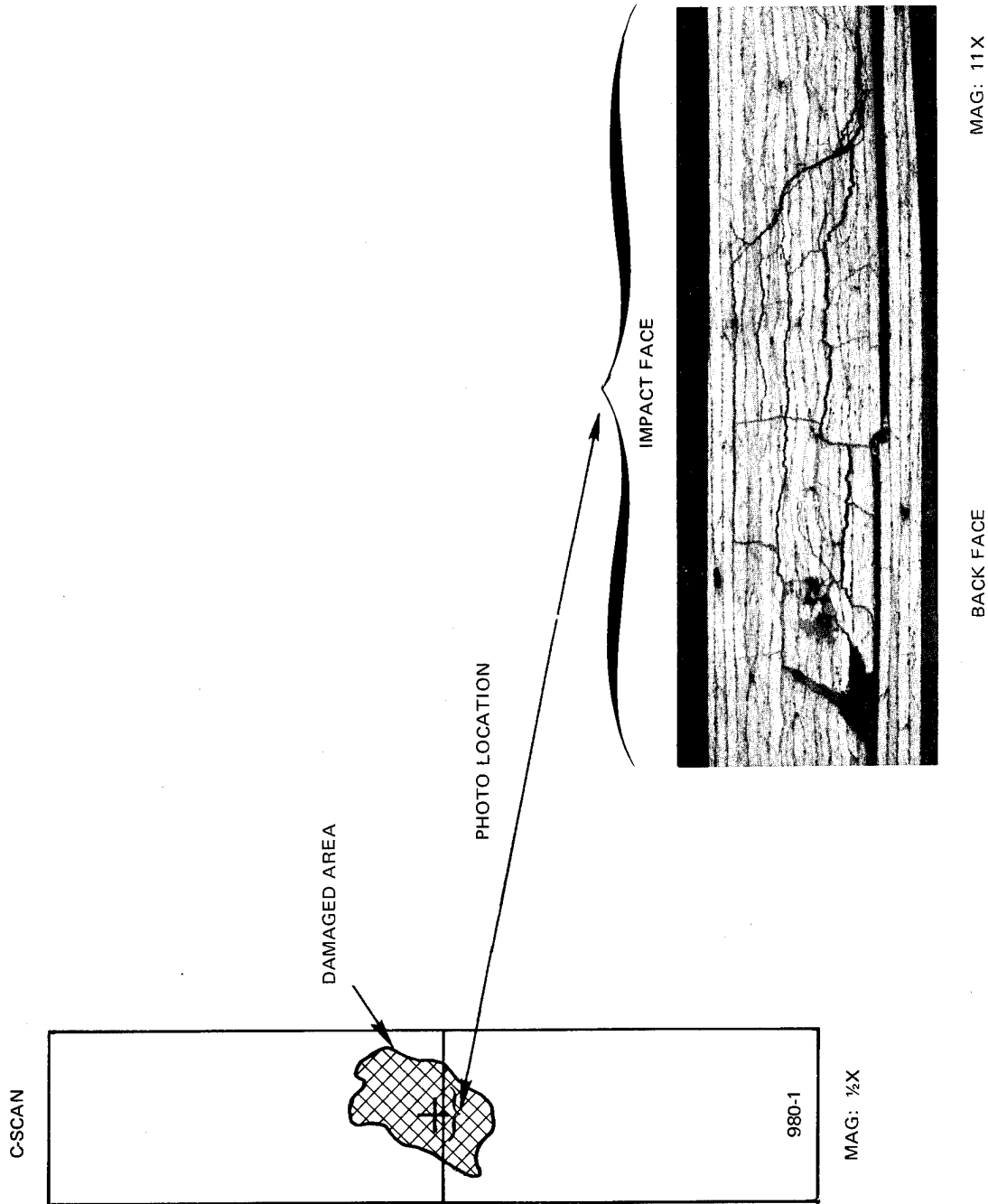
Figure 17   Transverse Cross Section View of $[(\pm45)_2 |0_{12} |(\mp45)_2]_T$ Modmor II/PR-286 Specimen After Impact With 0.64 cm Diameter Steel at 65.8 m/sec
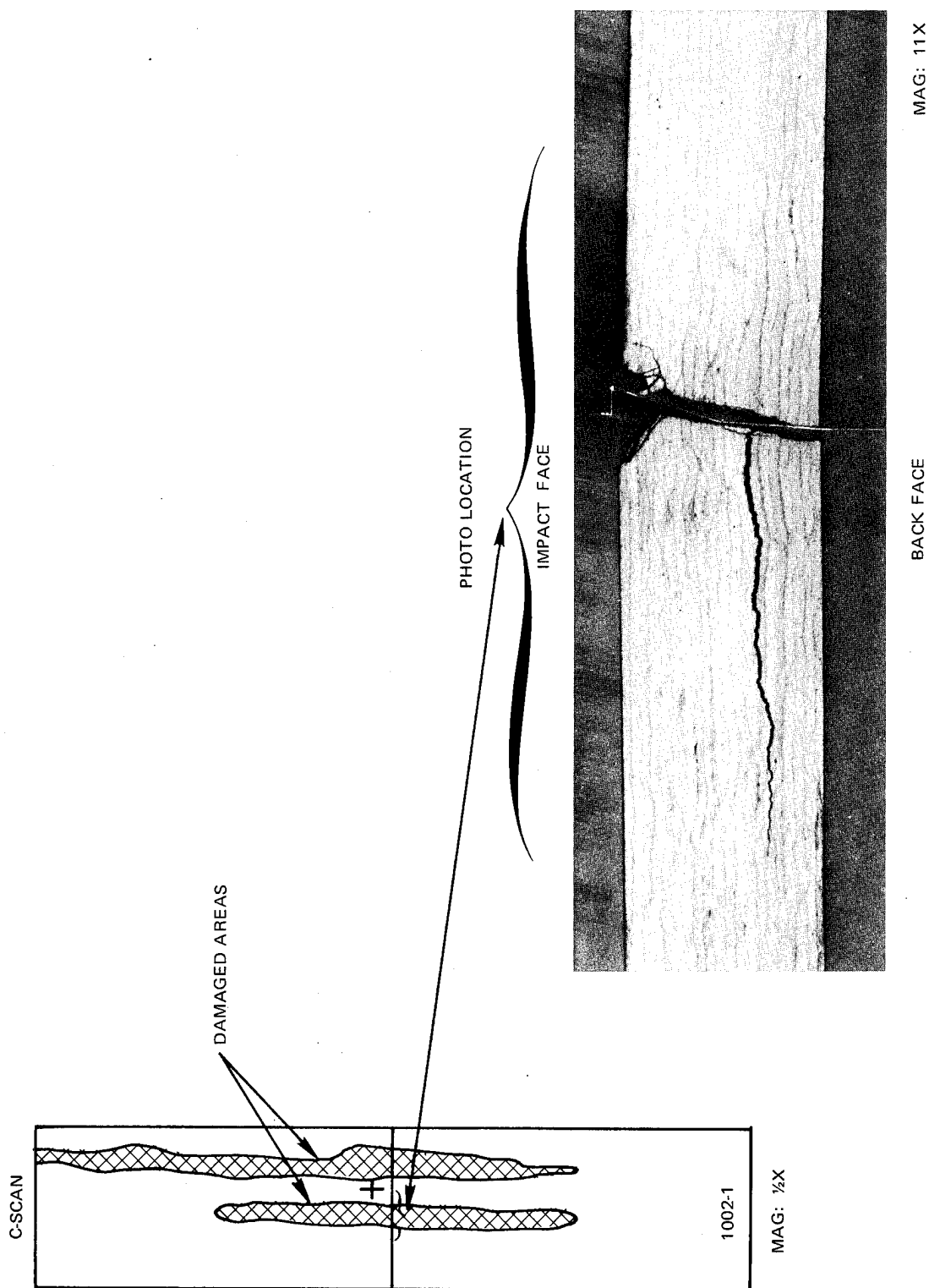
Figure 18   Transverse Cross Section View of $[0_{20}]_T$ Modmor II/PR-286 Specimen After Impact With 1.27 cm Diameter Ice at 262 m/sec
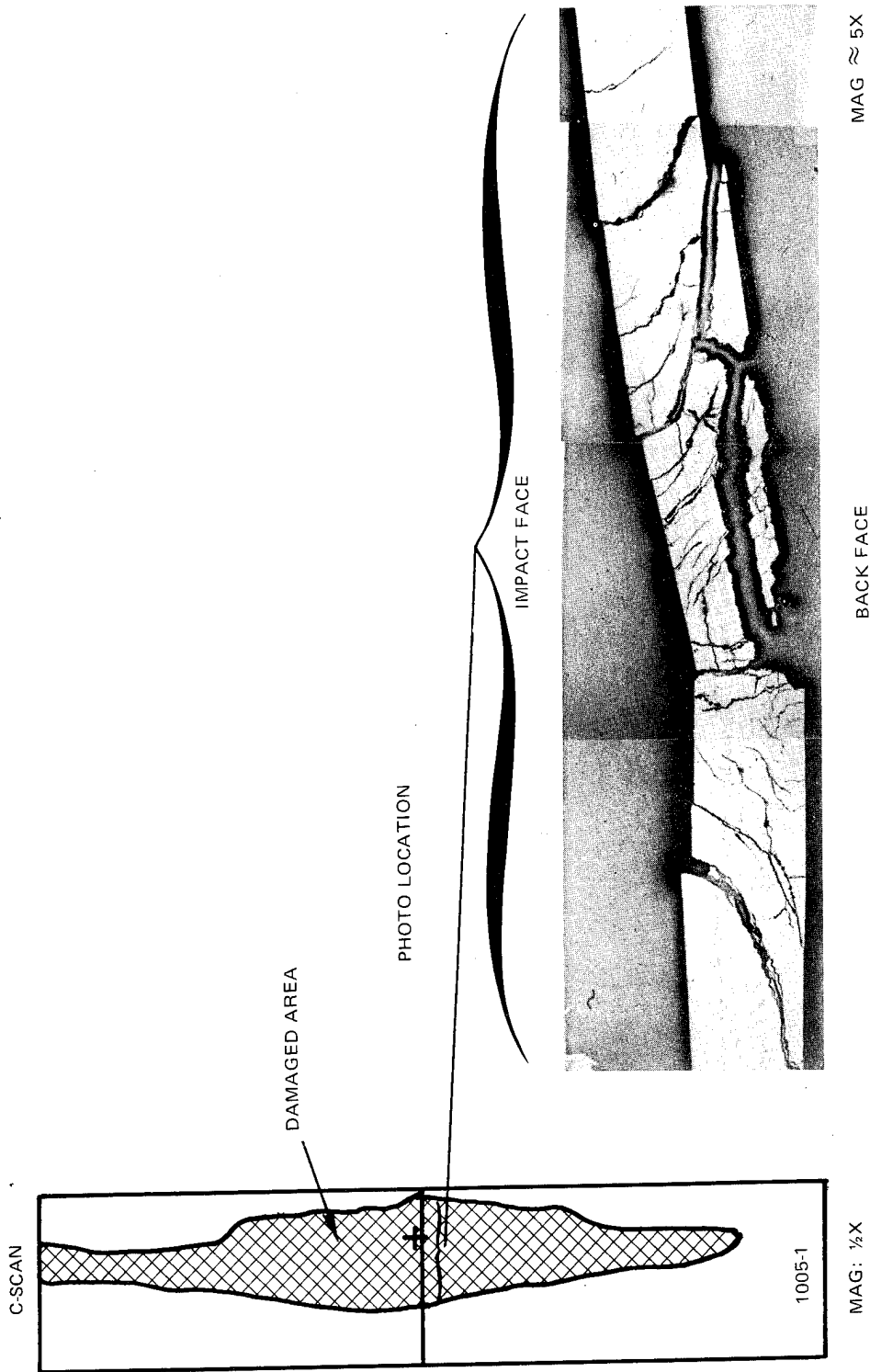
Figure 19   Transverse Cross Section View of $[0_{18}]_T$ T-75-S/PR-286 Specimen After Impact With 1.27 cm Diameter Ice at 260 m/sec

66

BARE FIBER SURFACE

MAG: 930 X

FRACTURED RESIN

BARE FIBER SURFACE
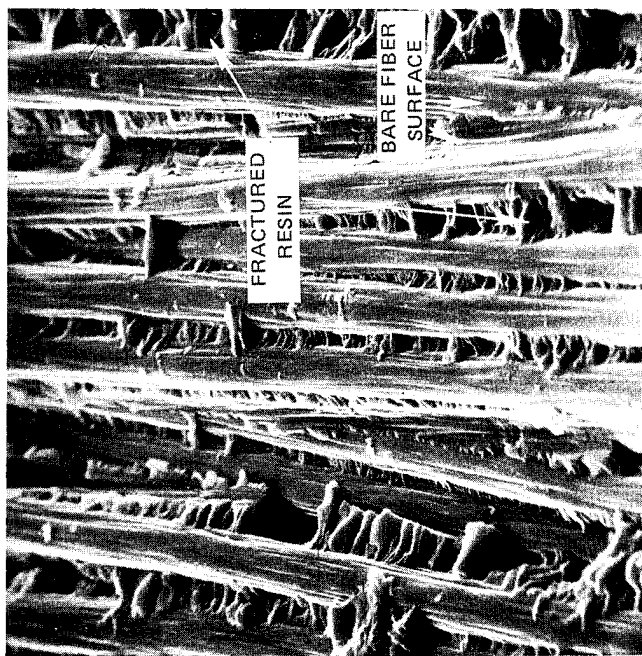
MAG: 930 X

Figure 20   Scanning Electron Microscope Photographs of Typical Interlaminar Fracture Surfaces From Impacted Modmor II/PR-286 Specimens

67

MAG: 1000 X

UNBONDED
FIBERS

MAG: 470 X

UNBONDED
FIBERS

Figure 21   Scanning Electron Microscope Photographs of a Modmor II/PR-286 Transverse
Tensile Specimen Fracture. (Note Completely Unbonded Fibers)

68

MAG: 4000X

FIBER

SMOOTH
FIBER-MATRIX
INTERFACE
FAILURE

MAG: 930X

SMOOTH
FIBER-MATRIX
INTERFACE
FAILURE

FIBER
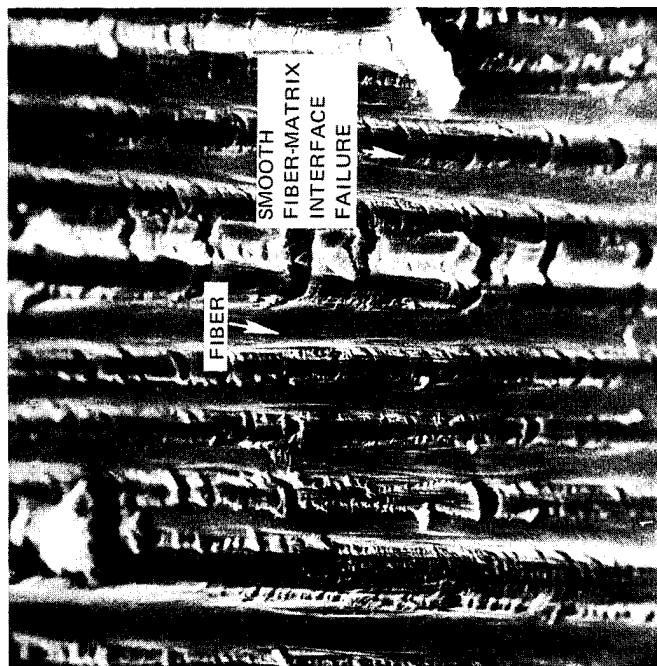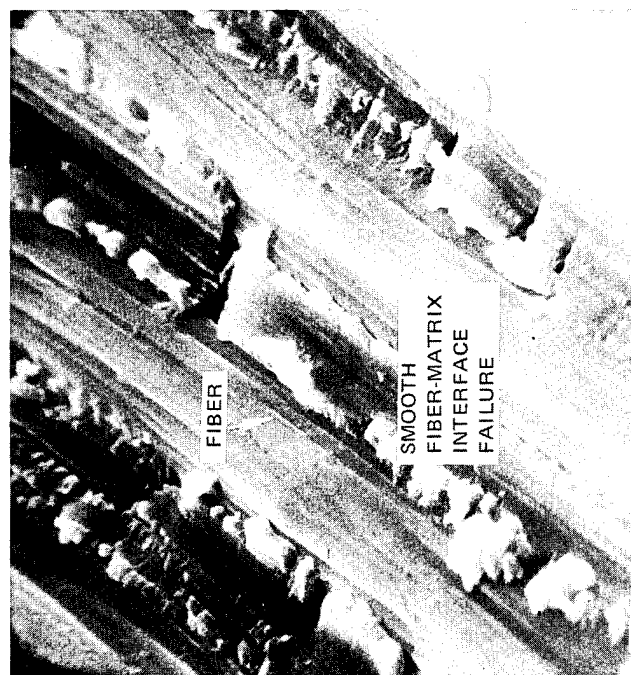
Figure 22   Scanning Electron Microscope Photographs of a Modmor II/PR-286 Short Beam
Interlaminar Shear Specimen Failure. (Note Lack of Matrix Tensile Fracture)

69
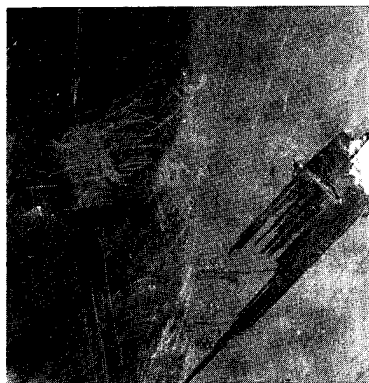
BACK   FRONT   NAS-13

0°, ± 45° MODMOR II/PR-286
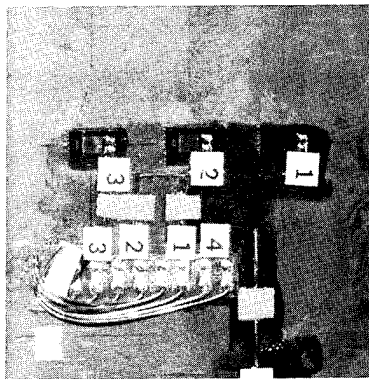
BACK   FRONT   NAS-41

0°, 90° MODMOR II/PR-286

Figure 23   Effect of Ply Configuration Upon Impact Damage to Modmor II/PR-286 Simu-
lated Blade Specimens After Impact at 15° on the Leading Edge With 1.27 cm
Diameter Gelatin at 274 m/sec. (Mag: 0.7X)

70

NAS-30

BACK   FRONT

15° - LE

NAS-9

BACK   FRONT

15° - QC

NAS-17

BACK   FRONT

0° - LE
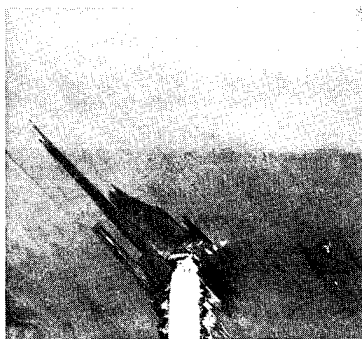
NAS-37
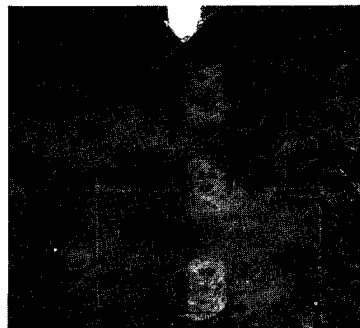
BACK   FRONT

30° - LE
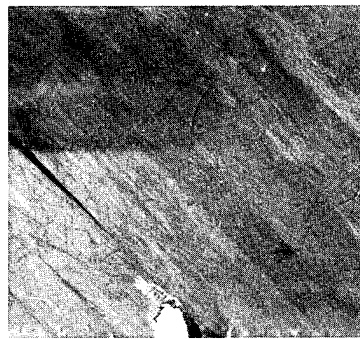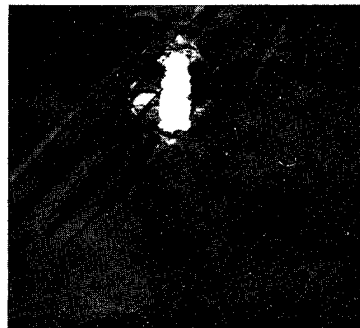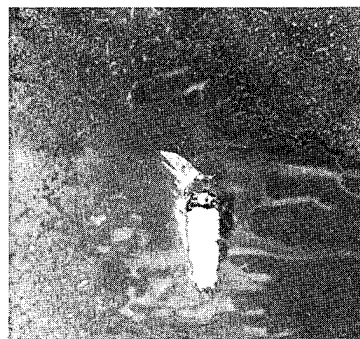
Figure 24   Effect of Impact Location and Angle Upon Damage to 0°, ±45° Modmor II/ PR-286 Simulated Blade Specimens Impacted With 0.64 cm Diameter Steel at 274 m/sec. (Mag: 0.7X)

71

BACK   FRONT

0° - LE

BACK   FRONT   NAS-113

15° - LE

BACK   FRONT   NAS-115

15° - QC
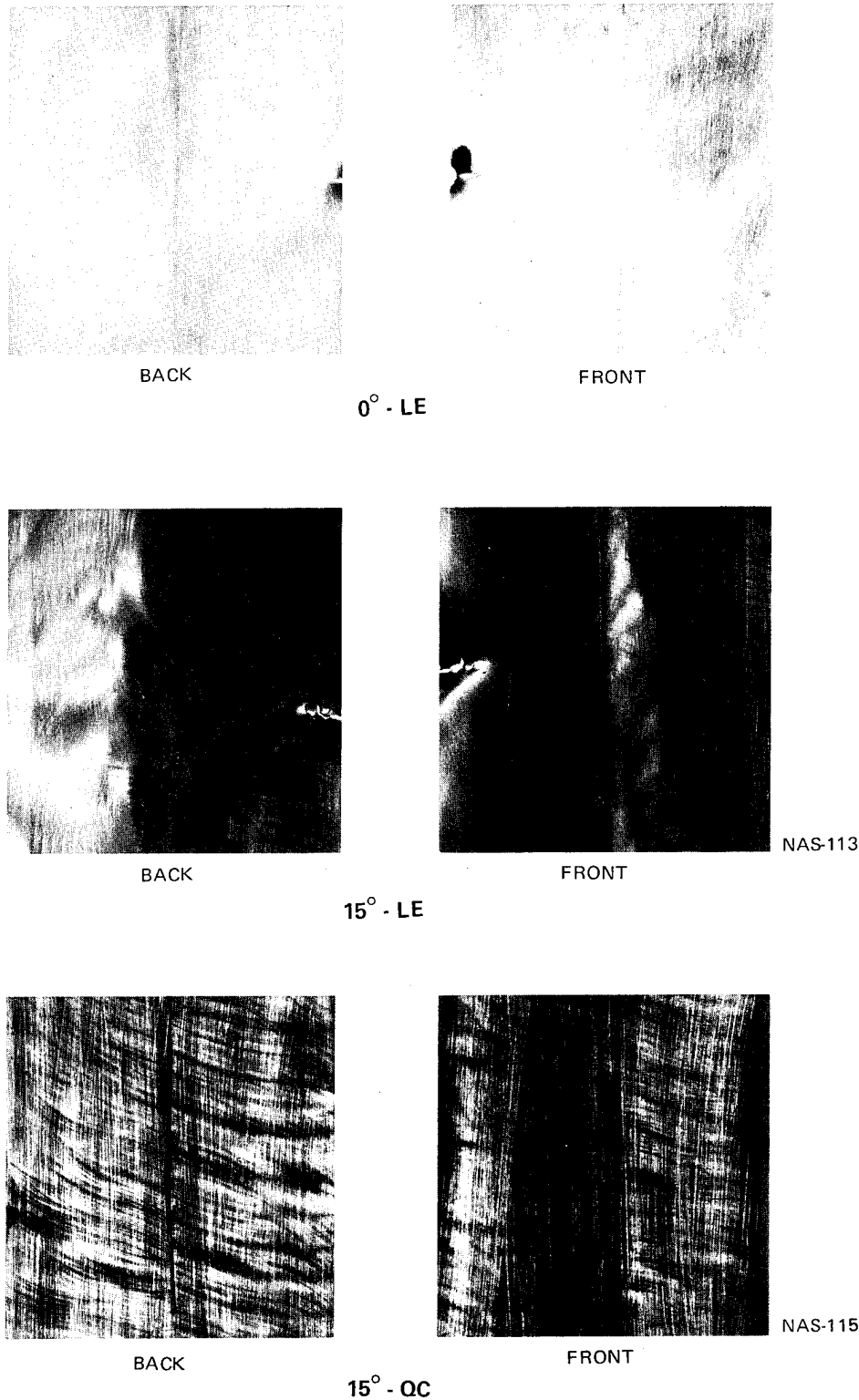
Figure 25   Effect of Impact Location and Angle Upon Damage to Titanium - 6Al-4V Simulated Blade Specimens Impacted With 0.64 cm Diameter Steel at 274 m/sec. (Mag: 0.7X)

72

NAS-13 · FRONT · BACK · **15° - LE**

NAS-2 · FRONT · BACK · **15° - QC**

NAS-24 · FRONT · BACK · **0° - LE**

NAS-45 · FRONT · BACK · **30° - LE**
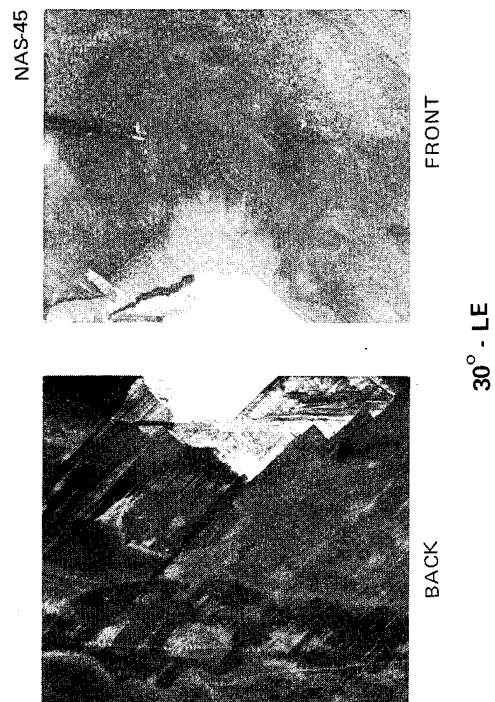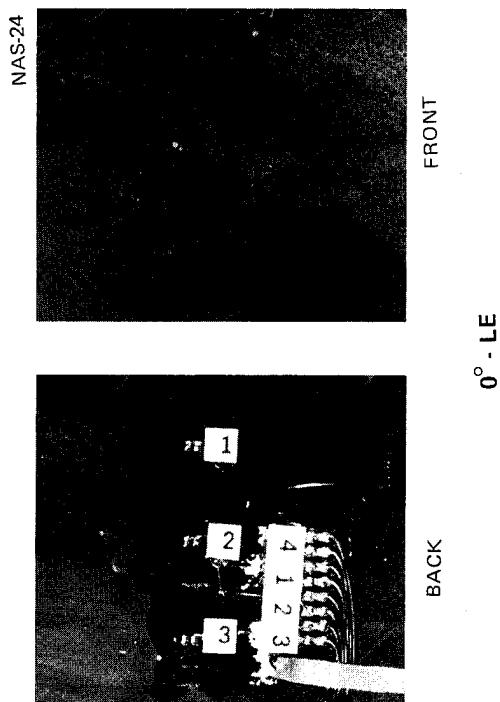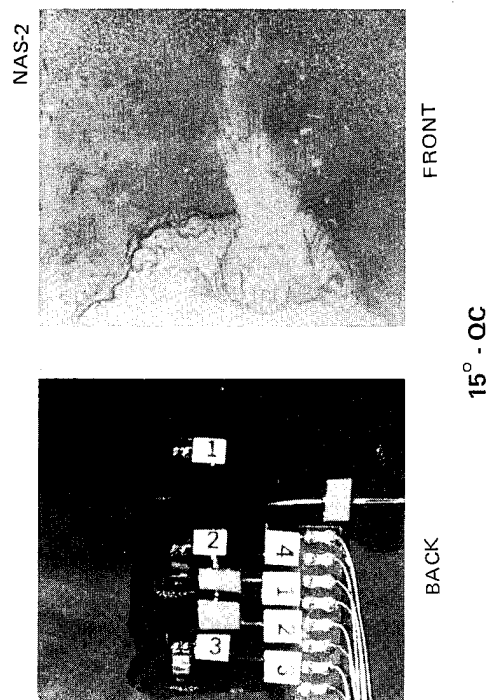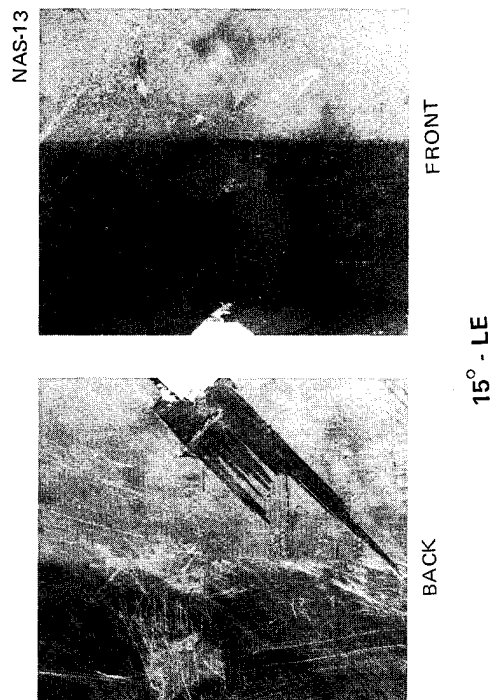
Figure 26   Effect of Impact Location and Angle Upon Damage to 0°, ±45° Modmor II/ PR-286 Simulated Blade Specimens Impacted With 1.27 cm Diameter Gelatin at Approximately 274 m/sec. (Mag: 0.7X)

73
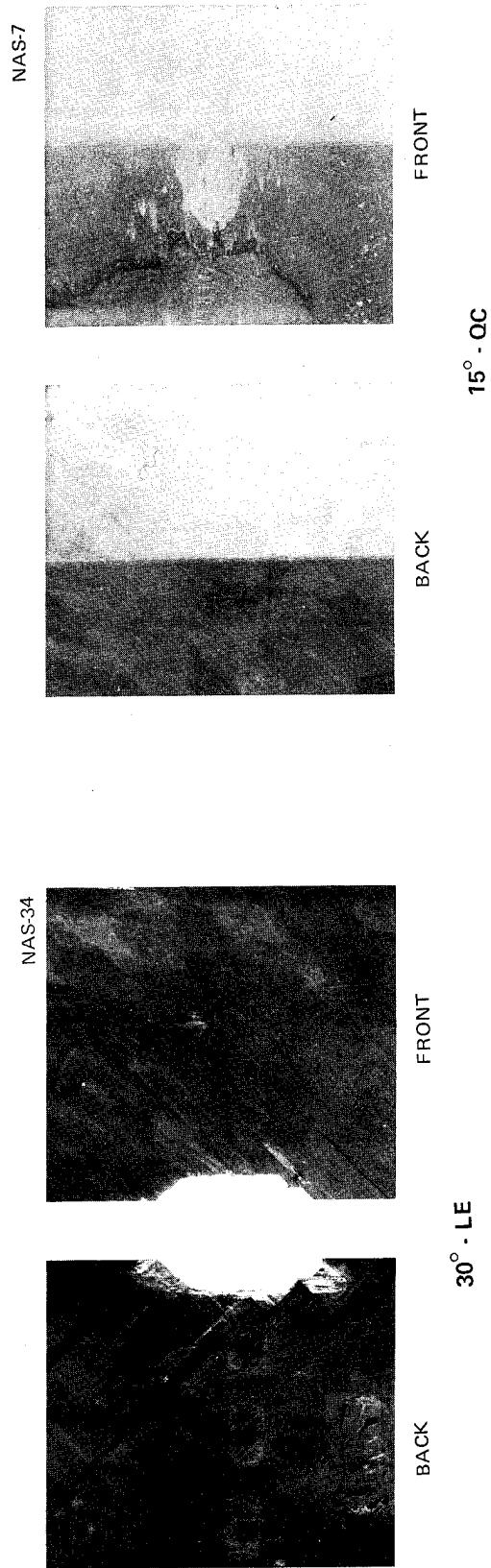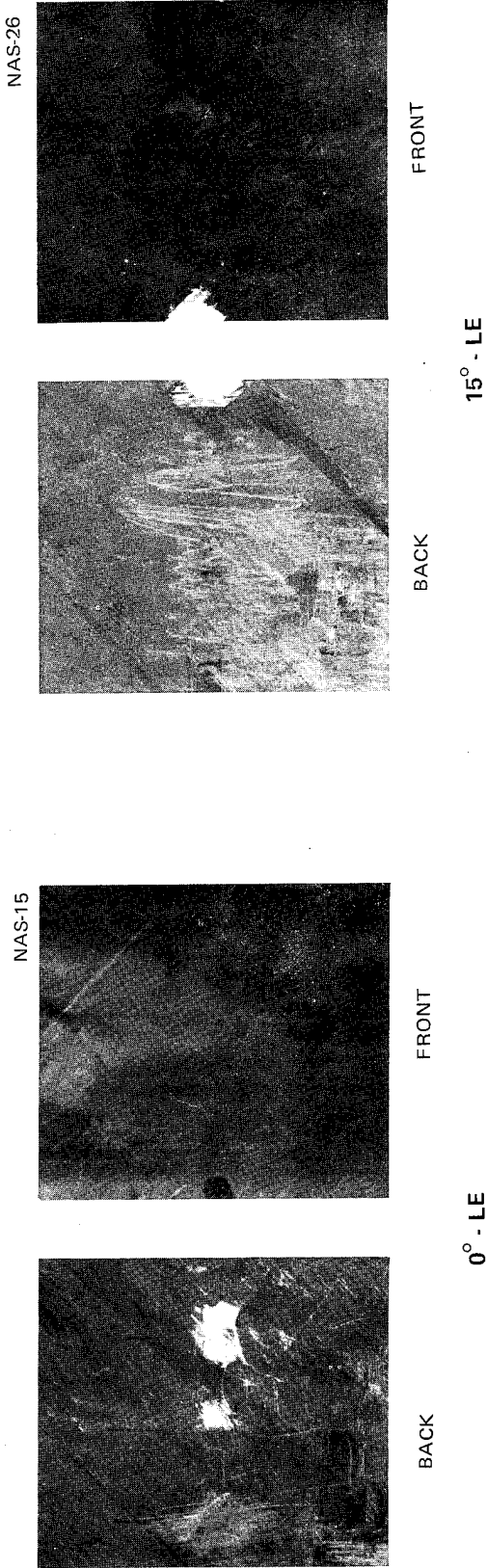
Figure 27   Effect of Impact Location and Angle Upon Damage to 0°, ±45° Modmor II/ PR-286 Simulated Blade Specimens Impacted With 1.27 cm Diameter Ice at Approximately 274 m/sec. (Mag: 0.7X)

74
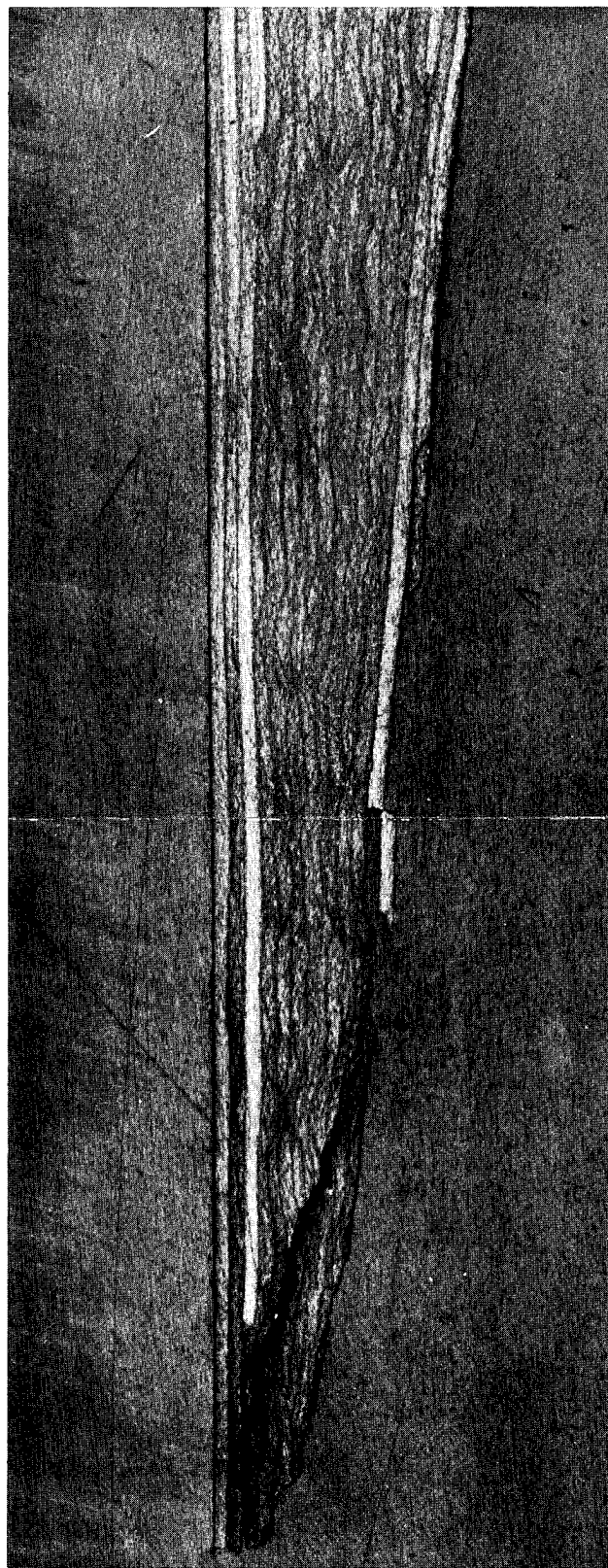
NAS-40

MAG:15X

Figure 28   Transverse View Showing Typical Leading Edge Damage Caused by
1.27 cm Diameter Gelatin Impact at 30° to the Leading Edge
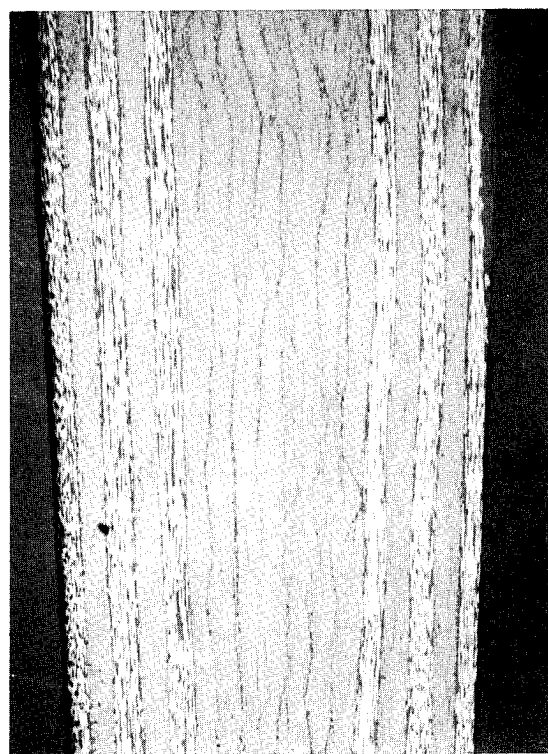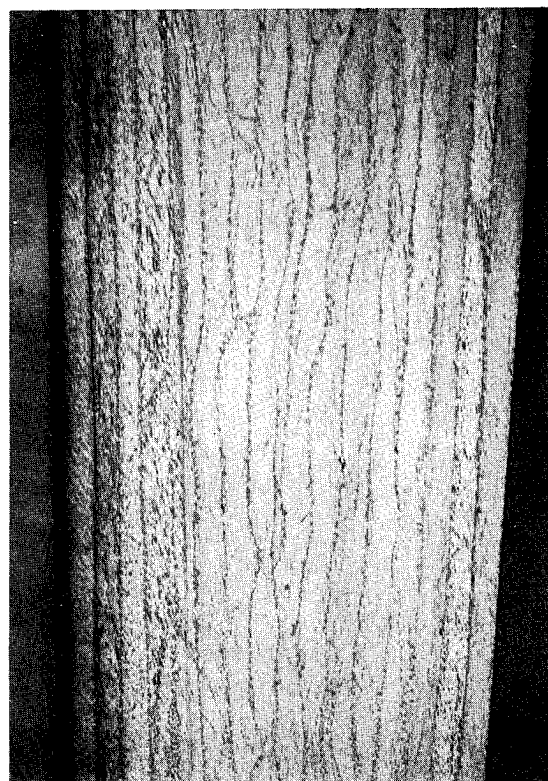
NAS-44 $(0°, 90°)$ MAG: 25X   NAS-3 $(0°, ±45°)$ MAG:25X

Figure 29   Transverse Cross Section Views of $0°$, $90°$ and $0°$, $±45°$ Modmor II/ PR-286 Specimens at the Quarter Chord Location Showing No Damage After Impact With 1.27 cm Diameter Gelatin at $15°$ - QC

76

MAG:7.5X

NAS-28
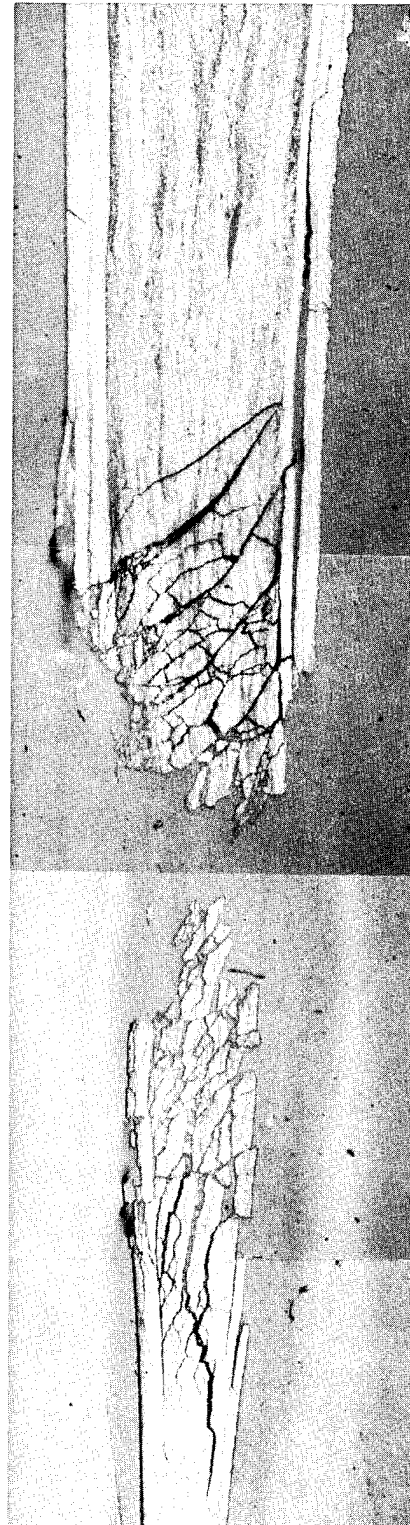
Figure 30   Cross Section View of Specimen Impacted With 0.64 cm Diameter Steel
at 15° Quarter-Chord and 274 m/sec Showing Multiple Fractures Typical
of Stress Wave Damage
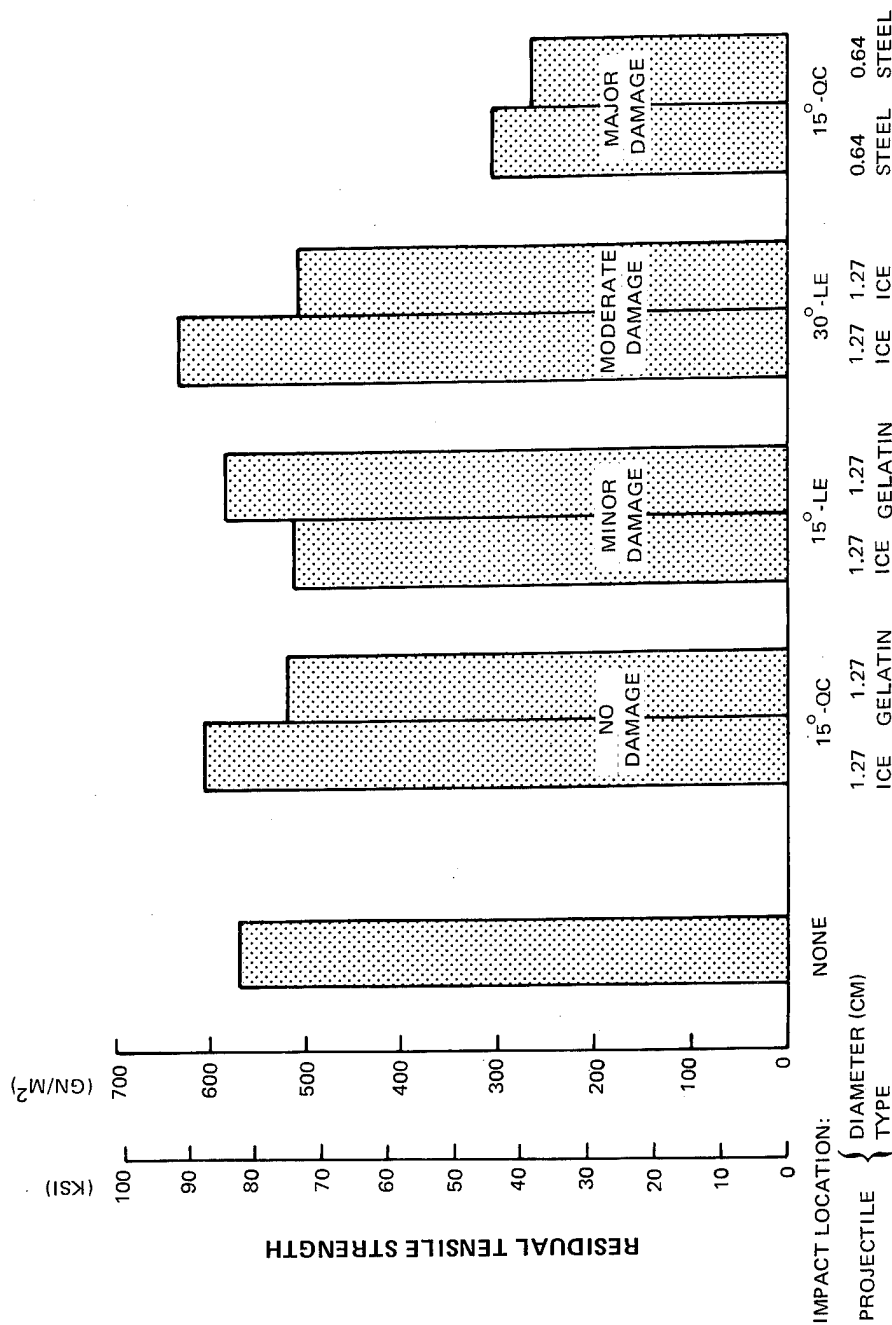
Figure 31   Residual Tensile Strength As a Function of Impact Damage (All Impacts
at 274 m/sec)

78
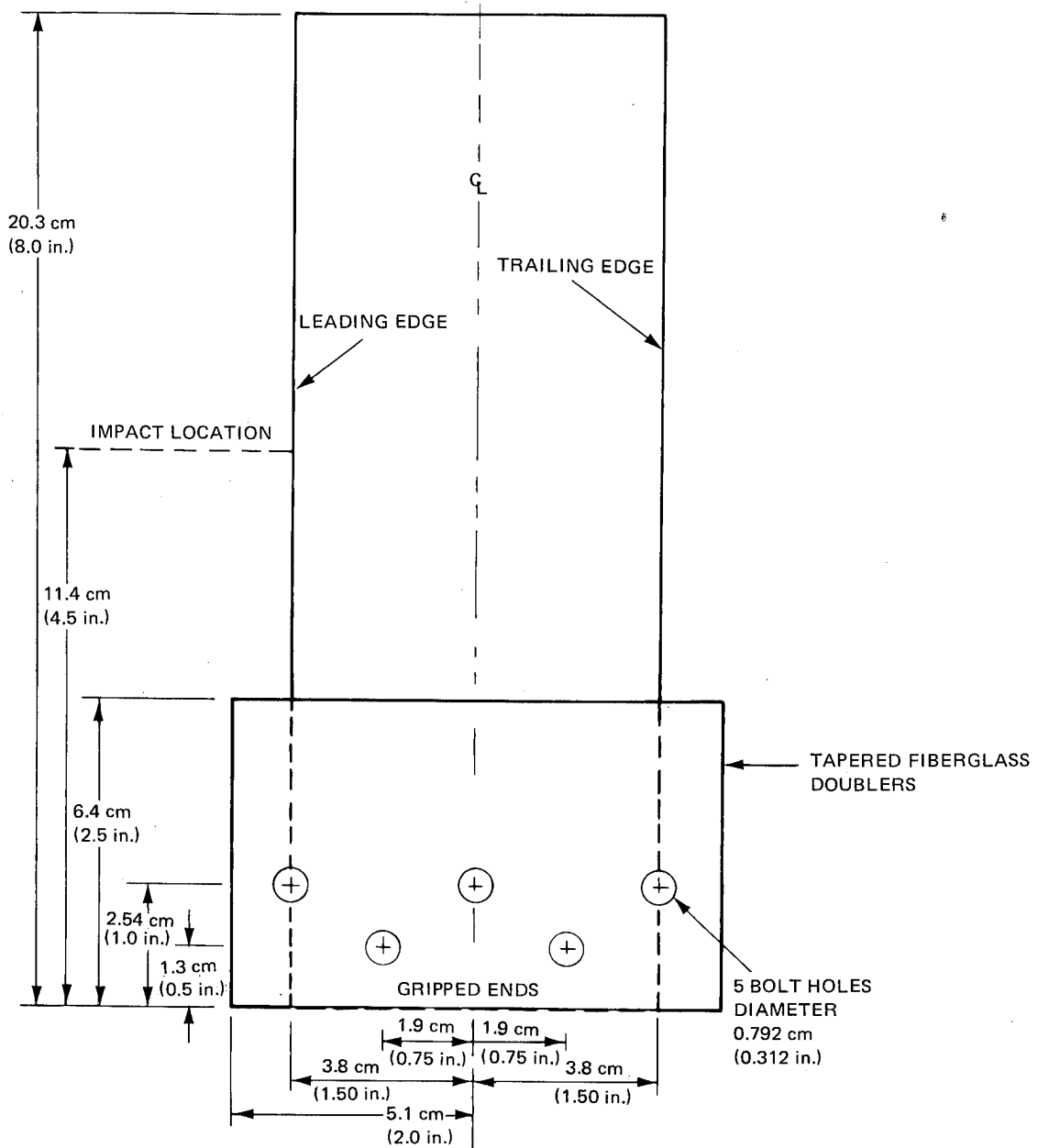
Figure 32   Task II Spin Impact Specimen Attachment Configuration

7.62 cm
(3.0 in.)

2.54 cm
(1.0 in.)

0.84 cm
(0.33 in.)

304 STAINLESS STEEL
INSERT

0°, ±45° MODMOR II/PR-286 COMPOSITE

0.015 cm
(0.006 in.) 301 STAINLESS STEEL FOIL
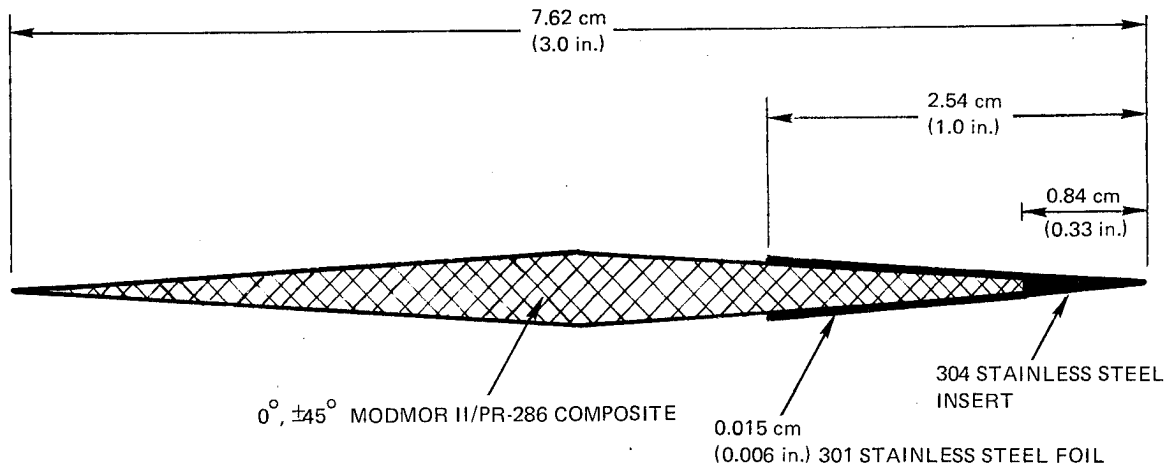
Figure 33   Cross Section View Showing Simulated Blade Specimen With Leading
Edge Protection

80
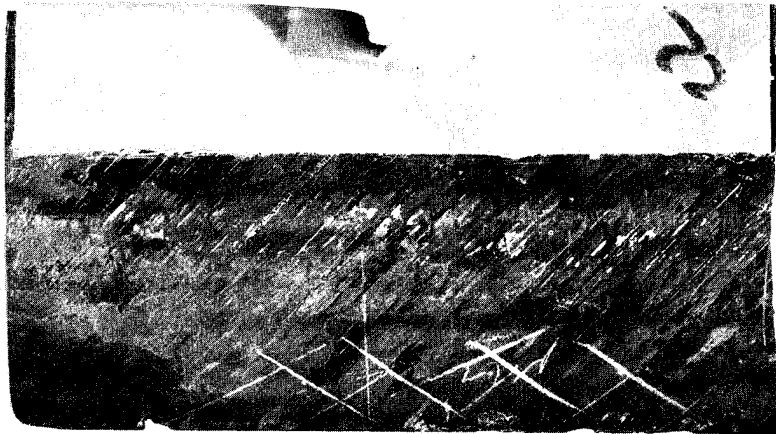
NAS-5

1.27 CM STEEL

NAS-22

0.64 CM STEEL

NAS-31

0.64 CM STEEL

Figure 34   Effect of Leading Edge FOD Shield Against Steel Projectiles at 274 m/sec (900 ft/sec). All Spin Impacts at 15° to the Leading Edge. (Mag: 0.9X)

81

NAS-36

2.54 CM ICE

NAS-47

1.27 CM ICE

ICE
IMPACT

DEBRIS

NAS-49

1.27 CM ICE
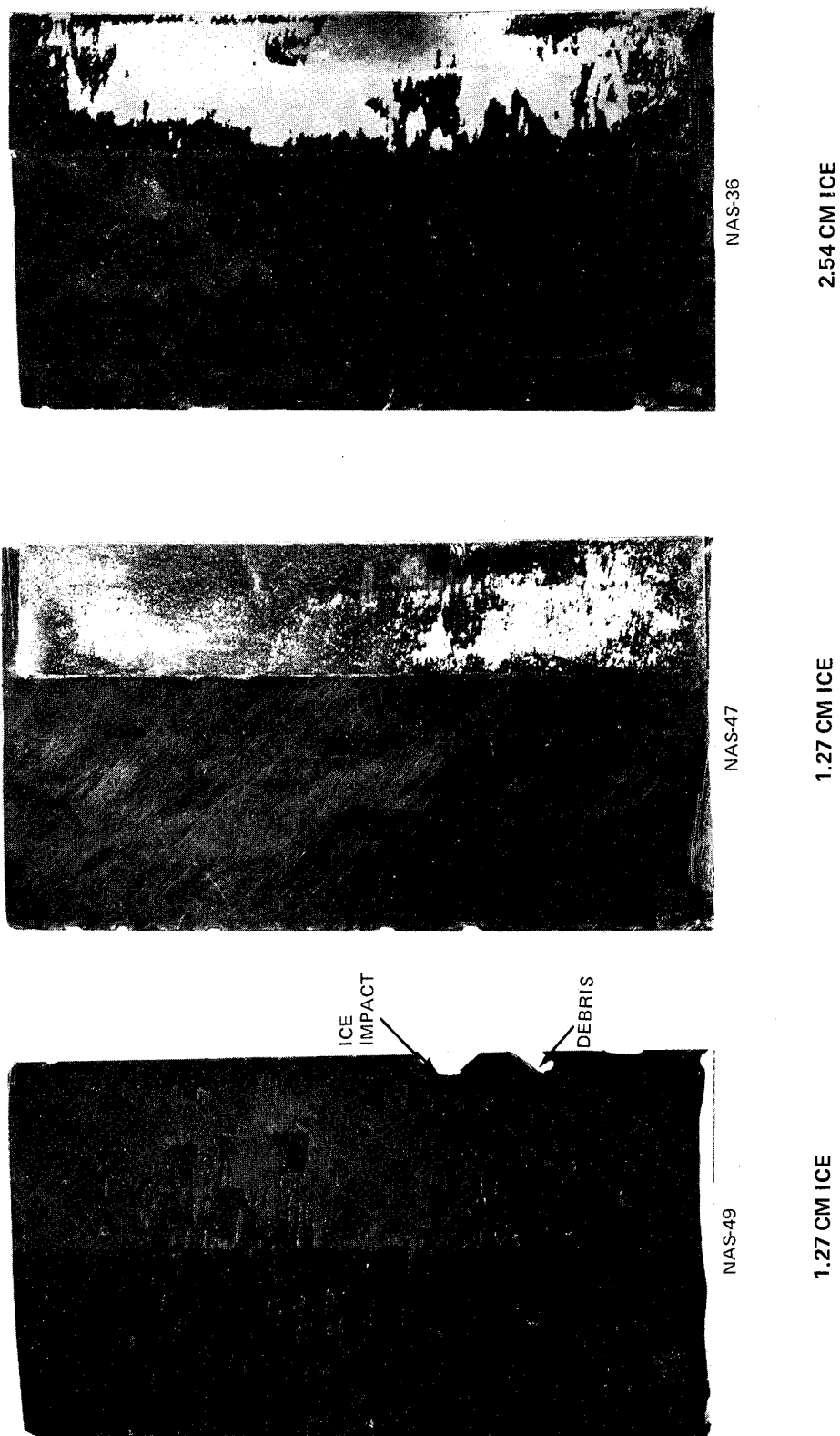
Figure 35   Effect of Leading Edge Shield Against Ice Particles at 274 m/sec (900 ft/
sec). All Spin Impacts at 30° on the Leading Edge. (Mag: 0.9X)

GELATIN IMPACT

DEBRIS
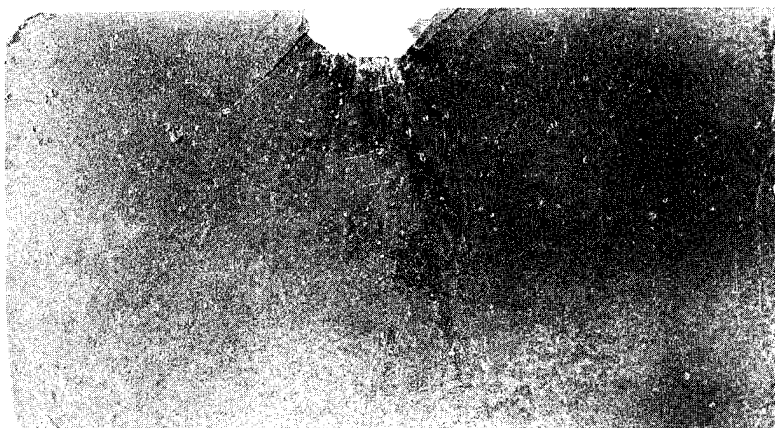
NAS-38
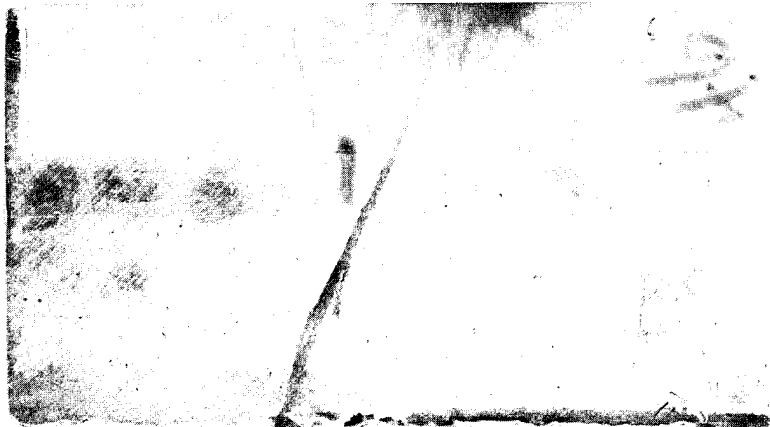
2.54 CM GELATIN

NAS-46

1.27 CM GELATIN

NAS-21
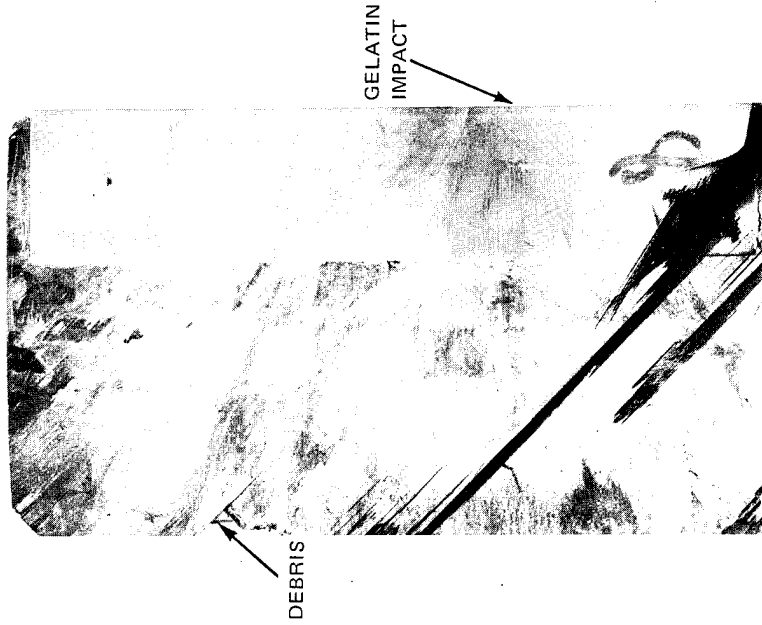
1.27 CM GELATIN

Figure 36   Effect of Leading Edge Shield Against Gelatin Projectiles at 274 m/sec (900 ft/sec). All Spin Impacts at 30° on the Leading Edge. (Mag: 0.9X)

83

BACK   FRONT   NAS-103
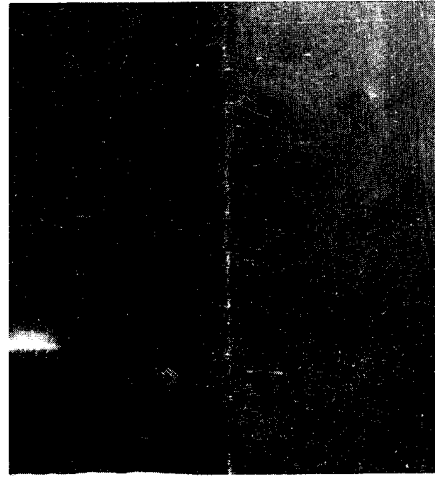
FRONT   BACK   NAS-101

Figure 37   Impact Damage to Titanium -6Al-4V Due to 0.64 cm Diameter Steel
               Impacts at 15° on the Leading Edge During Spin Test

84
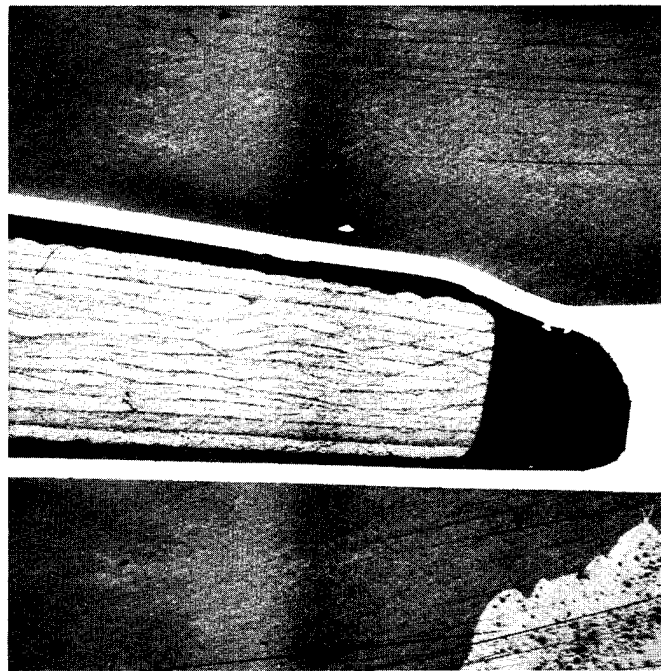
NAS-22   MAG:15X

Figure 38   Transverse Cross Section View of Modmor II/PR-286 Specimen Just
             Behind Point of Impact on FOD Shield Which was Spin Impacted With
             0.64 cm Diameter Steel at 274 m/sec. Note Lack of Damage to Composite

(1) VISUAL DAMAGE
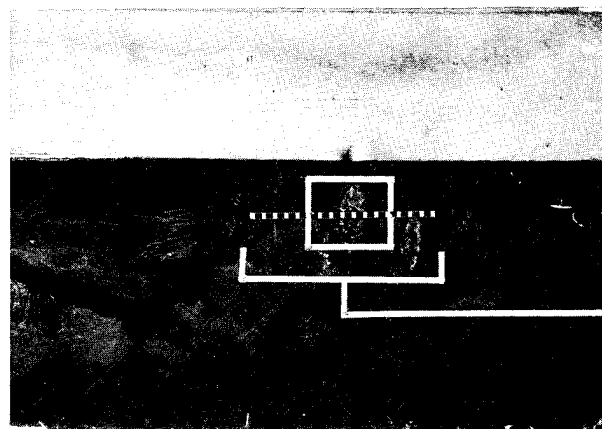
MAG:3/4X

(2) OUTER PLIES REMOVED
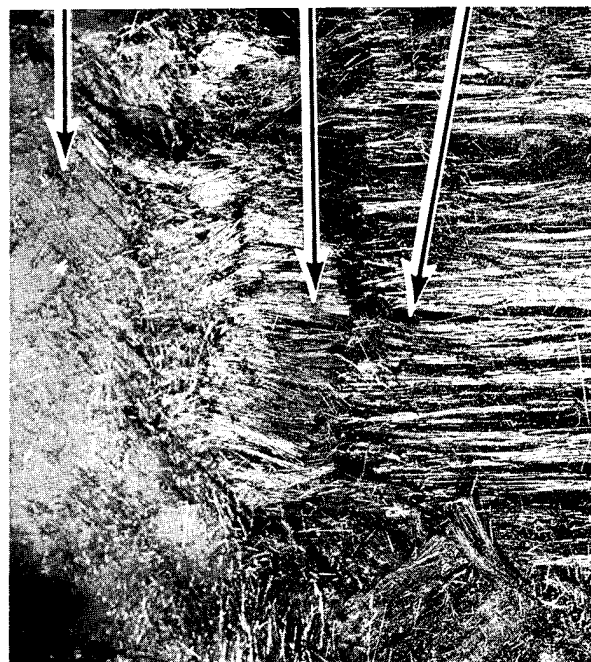
CROSS PLIES

BROKEN FIBERS IN OUTER LONGITUDINAL LAYER

BROKEN FIBERS IN SECOND LAYER

MAG:10X

(3) LONGITUDINAL CROSS SECTION
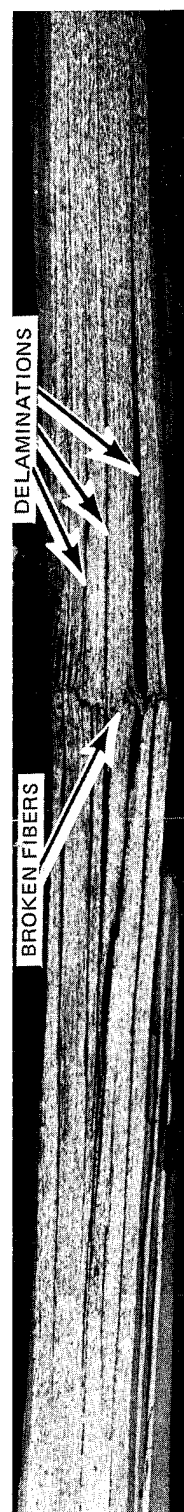
DELAMINATIONS

BROKEN FIBERS

MAG:5X

Figure 39   Specimen NAS-29 After Two Glancing Impacts at Mid-Chord With 0.64 cm Diameter Steel at 274 m/sec. Insert 1 Shows Minimal Visual Damage at Impact Points. Inserts 2 and 3 Reveal That Broken Longitudinal Fibers and Delamination Extends Through Entire Specimen Thickness.

86
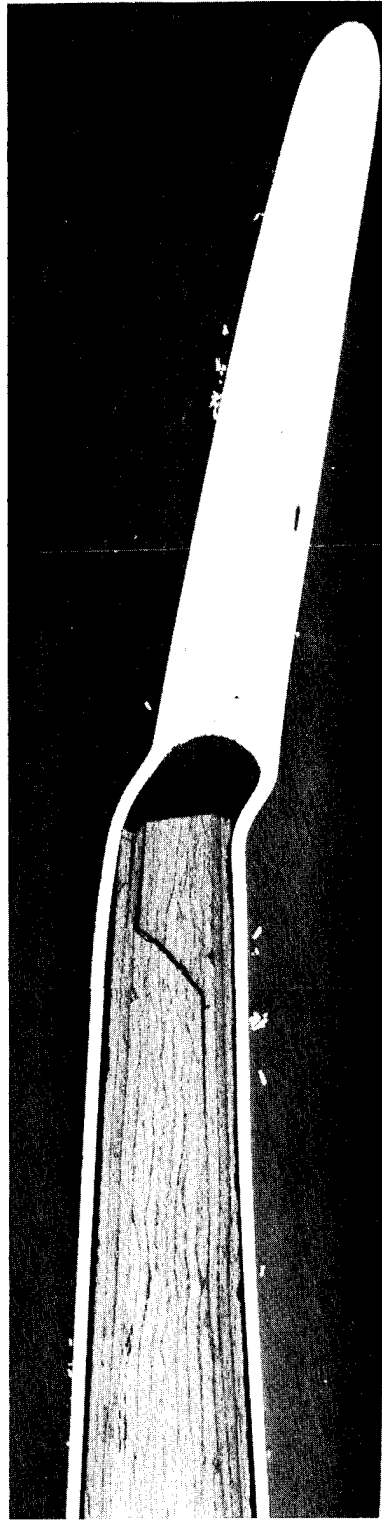
MAG:11X

NAS-48

Figure 40   Transverse Cross Section View of Leading Edge Shield-to-Composite
Region Showing Ductile Behavior of Foil and Slight Cracking in Composite
After 2.54 cm Diameter Ice Impact at 274 m/sec and 30° to the Leading
Edge
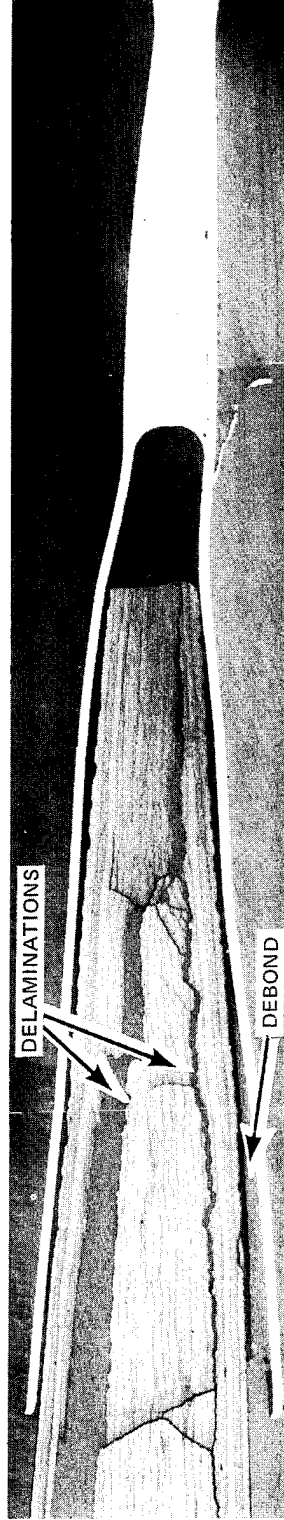
Figure 41   Transverse Cross Section View of Leading Edge-to-Composite Region
Showing Severe Delamination in Composite After 2.54cm Diameter
Gelatin Impact at 274 m/sec and 30° to the Leading Edge

NAS-109

TITANIUM-6Al-4V

NAS-12

MODMOR II/PR-286
WITH FOD SHIELD

NAS-32

MODMOR II/PR-286
UNPROTECTED
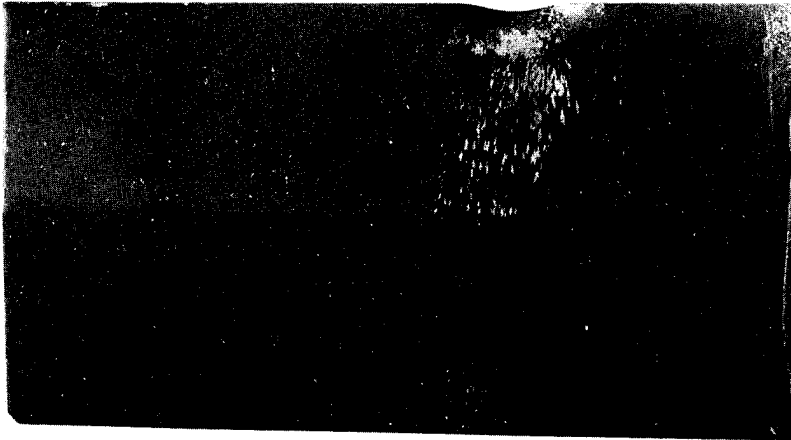
Figure 42   Effect of Leading Edge FOD Shield Against 2.54 cm Diameter Ice Projectiles at 396 m/sec (1300 ft/sec). All Impacts at 15° on Leading Edge. (Mag: 0.9X)

89
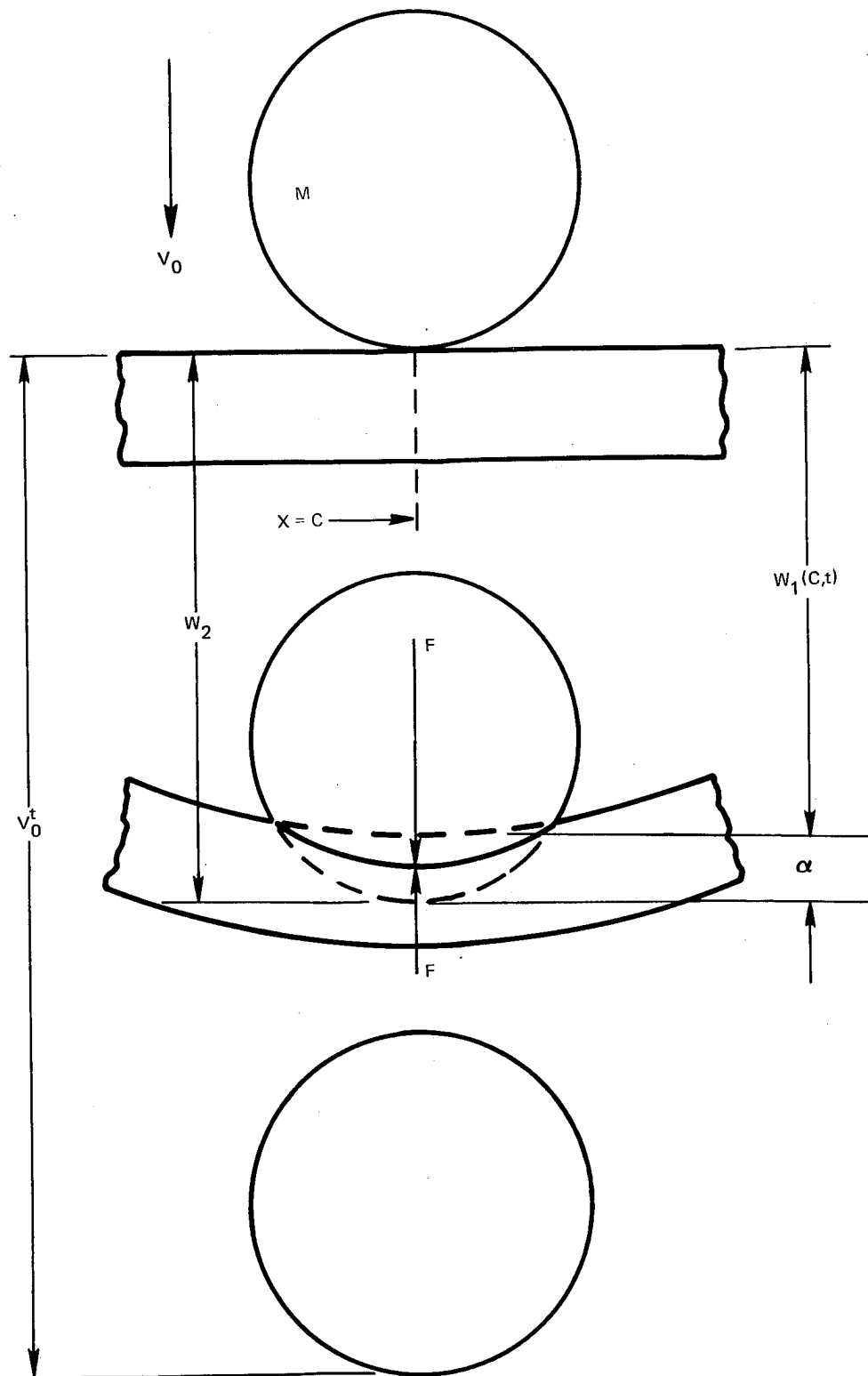
Figure 43   Geometry of Spherical Projectile Impact on a Beam

SPHERE   EQUIVALENT CYCLINDER

PHYSICAL MODEL

$$V = \frac{4}{3}\pi\frac{D^3}{8} = \frac{\pi}{6}D^3$$

$$\text{MASS} = \frac{\pi}{6}D^3\rho$$

$$V = \frac{\pi D^2}{4} \cdot D = \frac{\pi}{4}D^3$$

$$\text{MASS} = \frac{\pi}{4}D^3\rho' = \frac{\pi}{6}D^3\rho$$

$$\text{WHERE } \rho' = 2/3\,\rho$$
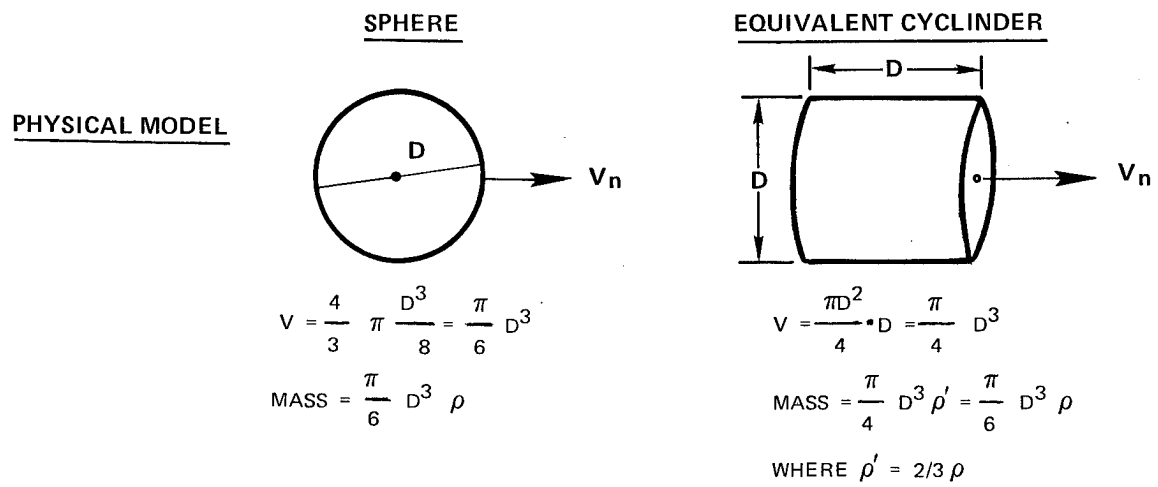
Figure 44   Dimensions of Equivalent Cylinder Used to Calculate the Average Momentum-Impulse Force
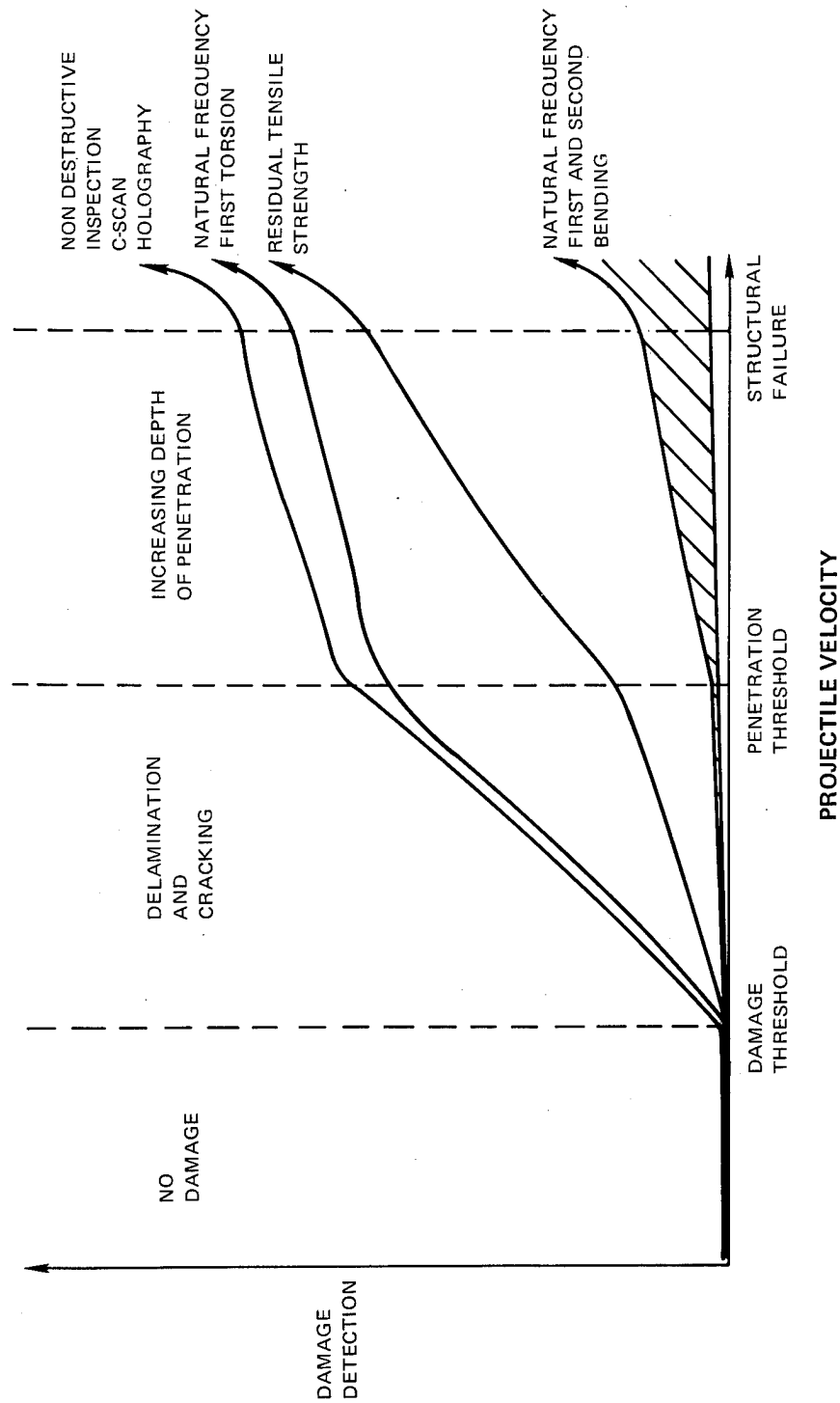
Figure 45
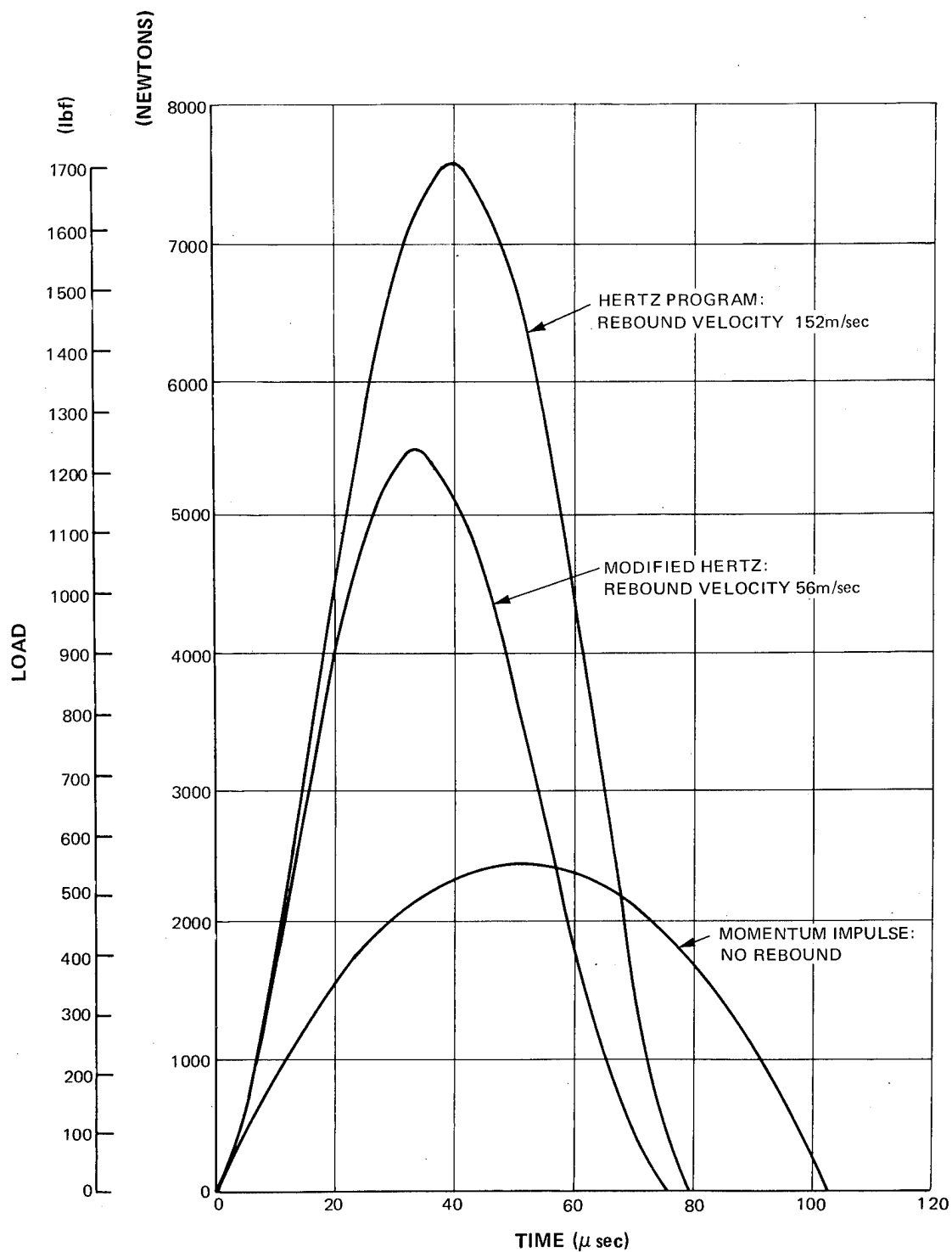
Figure 46   Load as a Function of Time for 1.27 cm Diameter Gelatin at 152 m/sec
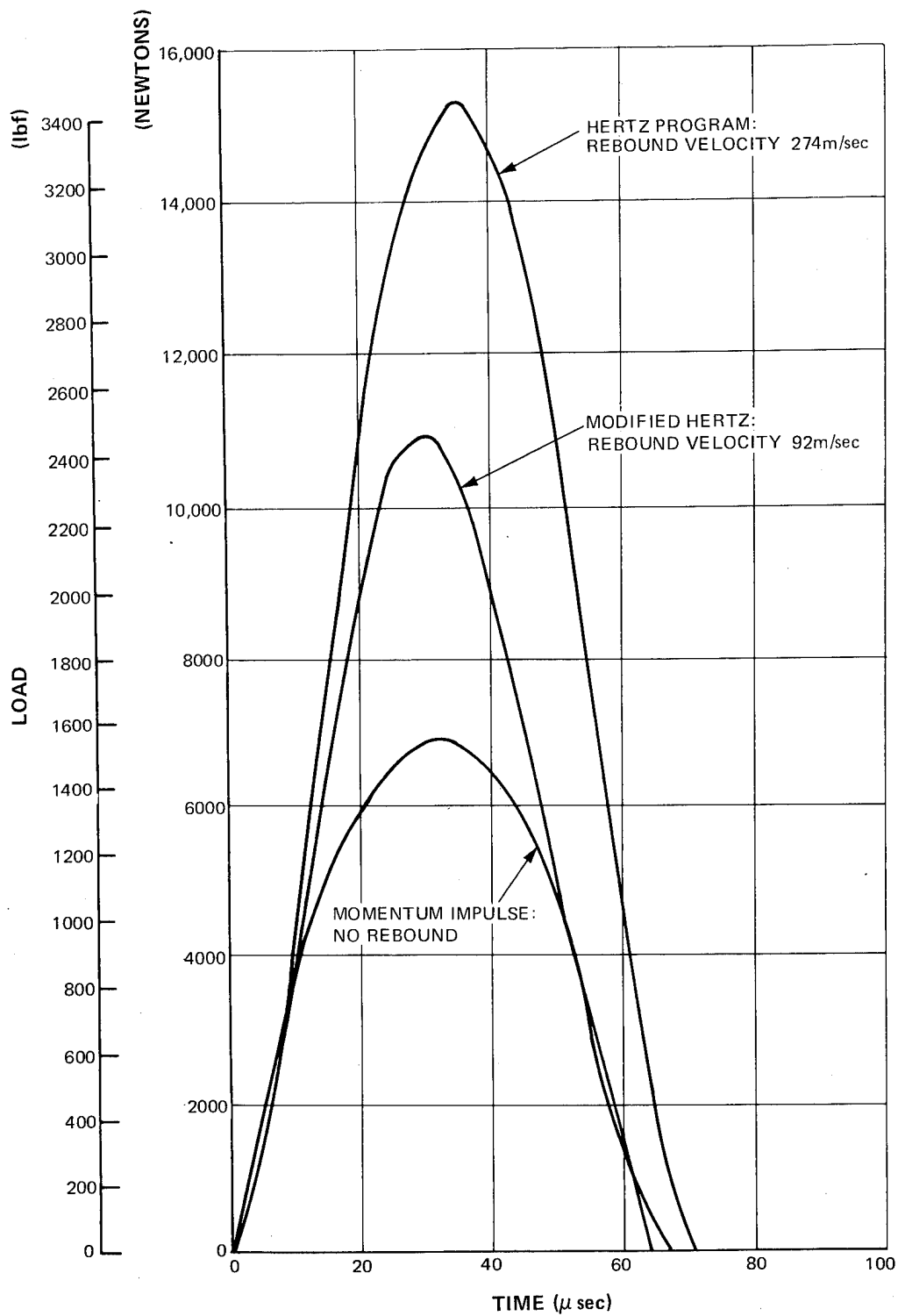
Figure 47   Load as a Function of Time for 1.27 cm Diameter Gelatin at 274 m/sec
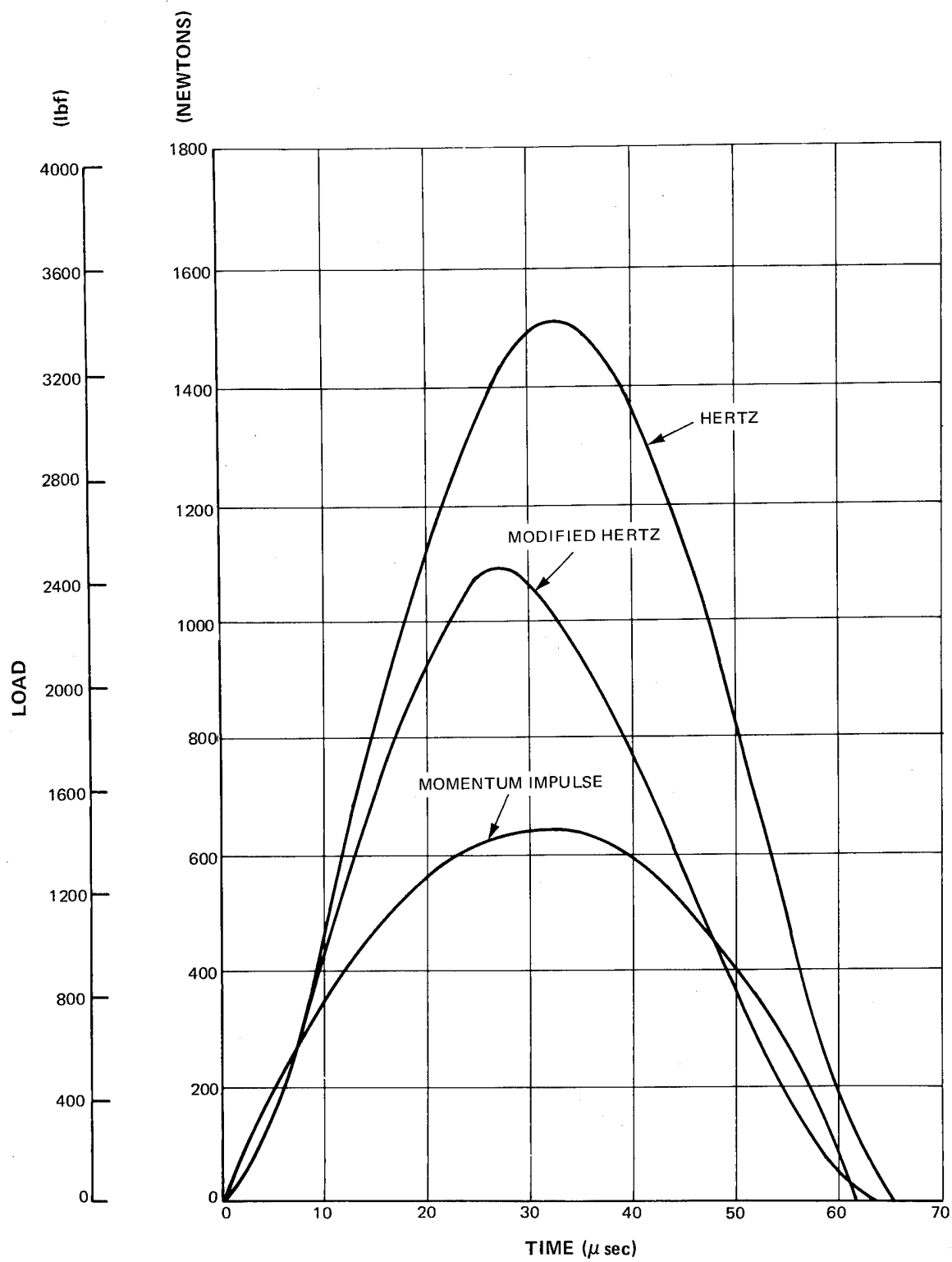
Figure 48   Load as a Function of Time for 1.27 cm Diameter Ice at 274 m/sec
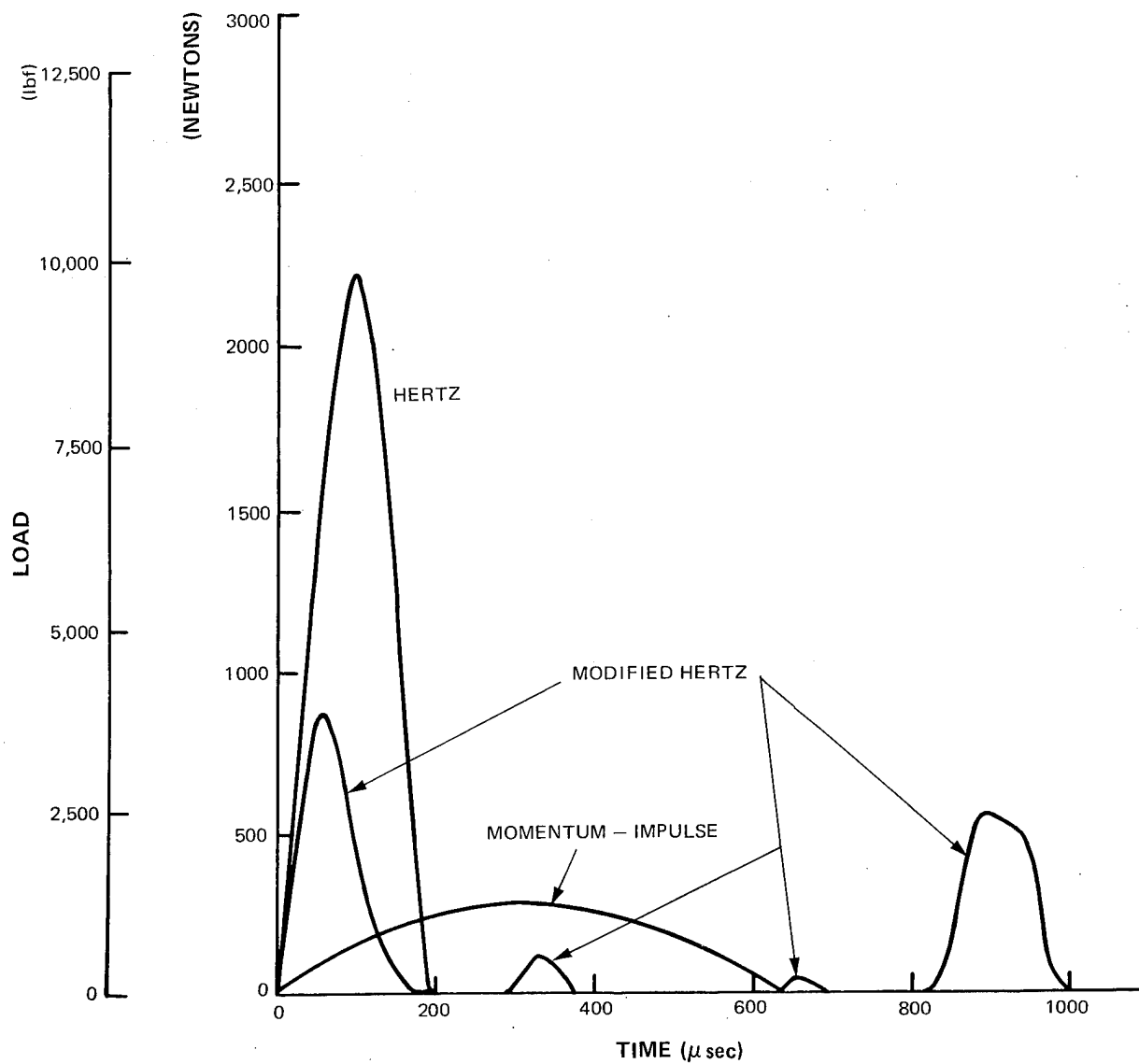
Figure 49   Load as a Function of Time for 2.54 cm Diameter Gelatin at 61 m/sec
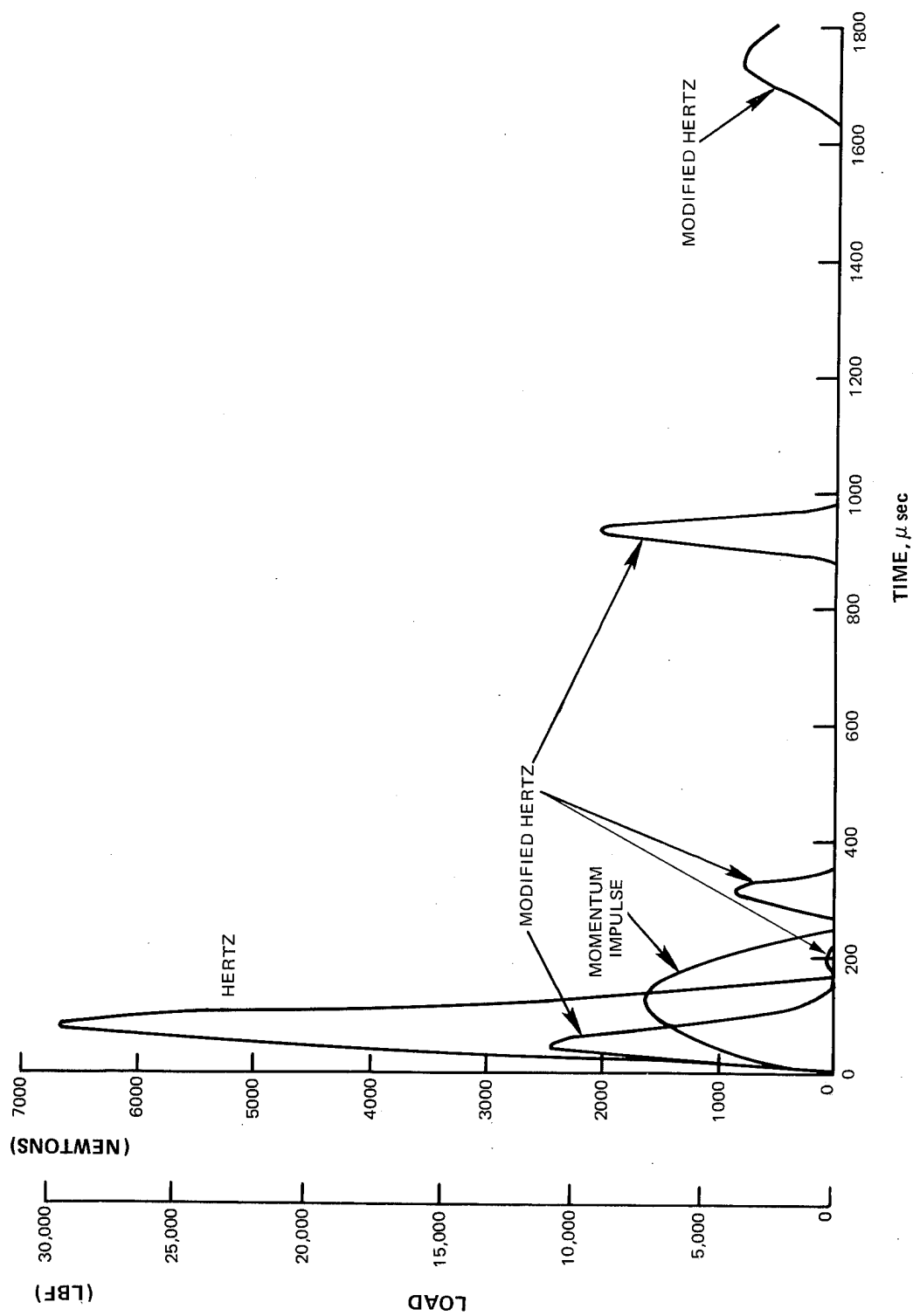
Figure 50   Load as a Function of Time for 2.54 cm Diameter Gelatin at 152 m/sec
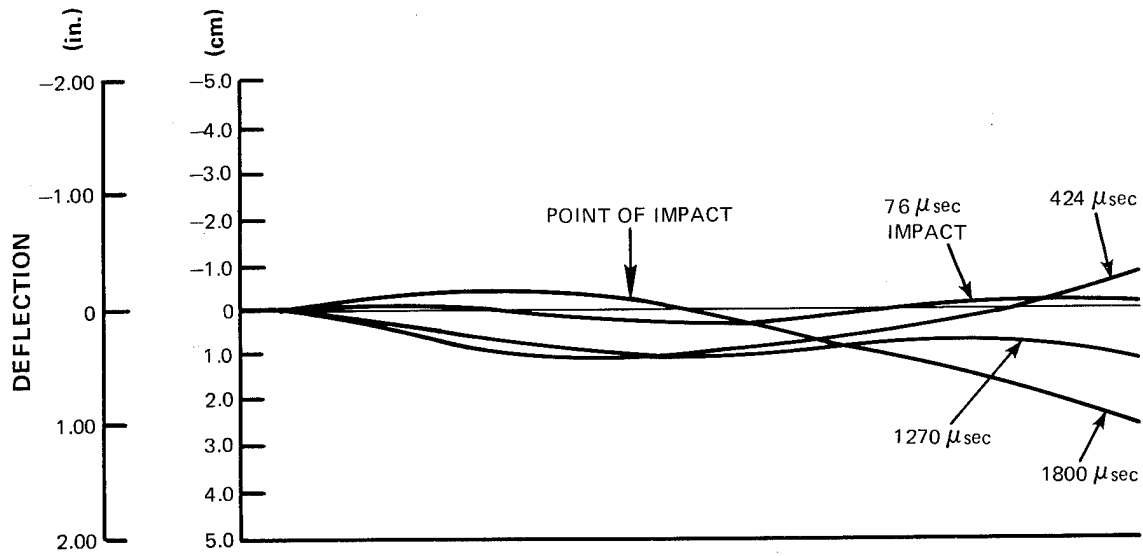
Figure 51   Deflection as a Function of Time for a Cantilevered $[(\pm 45)_2 \mid 0_{12} \mid (\mp 45)_2]_T$ Modmor II/PR-286 Composite Beam Impacted by 1.27 cm Diameter Gelatin at 152 m/sec
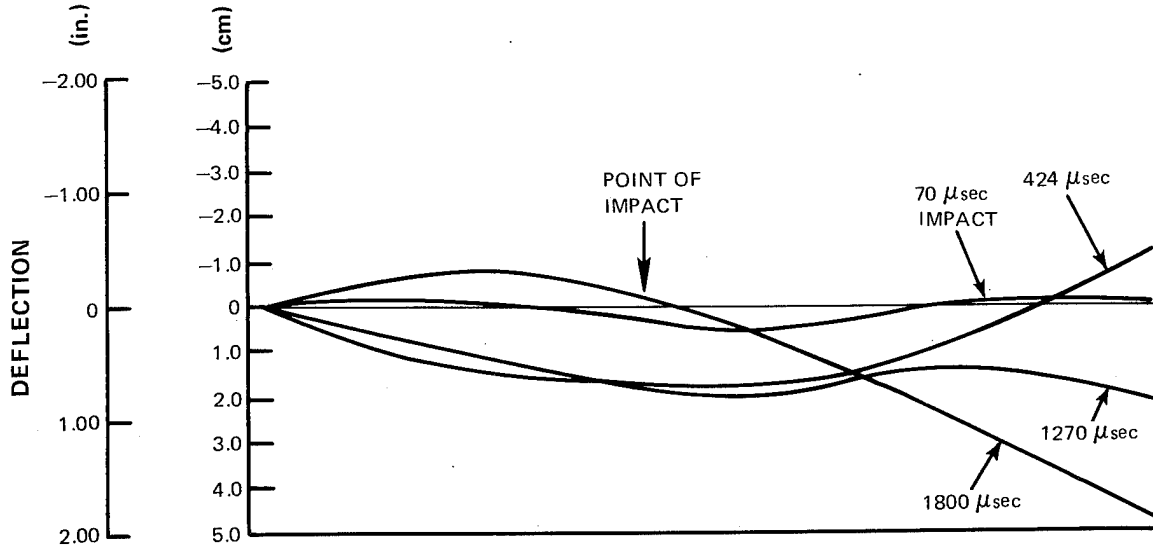
Figure 52   Deflection as a Function of Time for a Cantilevered $[(\pm 45)_2 \mid 0_{12} \mid (\mp 45)_2]_T$ Modmor II/PR-286 Composite Beam Inpacted by 1.27 cm Diameter Gelatin at 274 m/sec
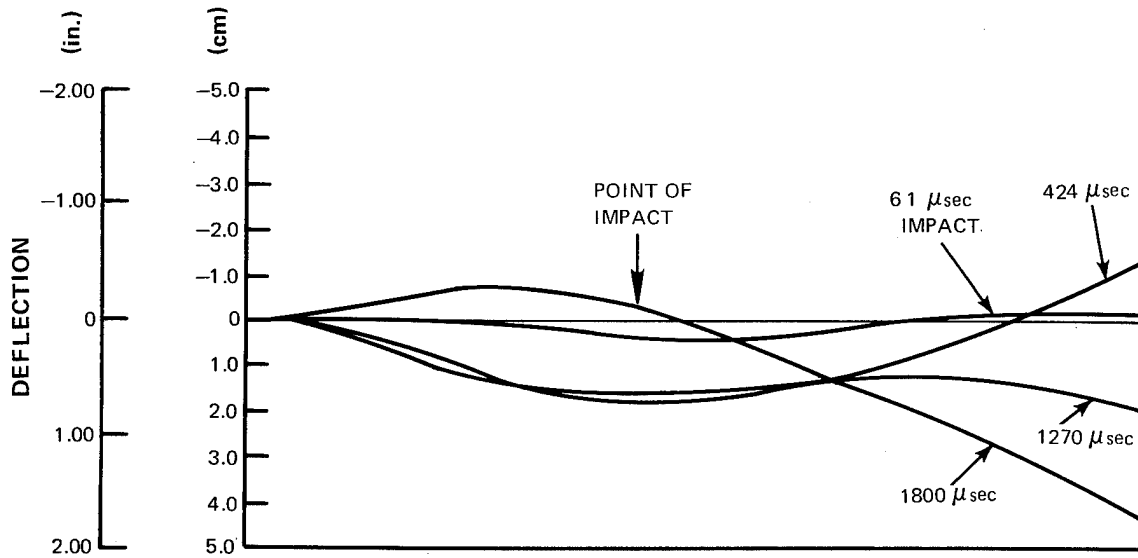
Figure 53   Deflection as a Function of Time for a Cantilevered $[(\pm 45)_2 \mid 0_{12} \mid (\mp 45)_2]_T$ Modmor II/PR-286 Composite Beam Impacted by 12.7 cm Diameter Ice at 274 m/sec
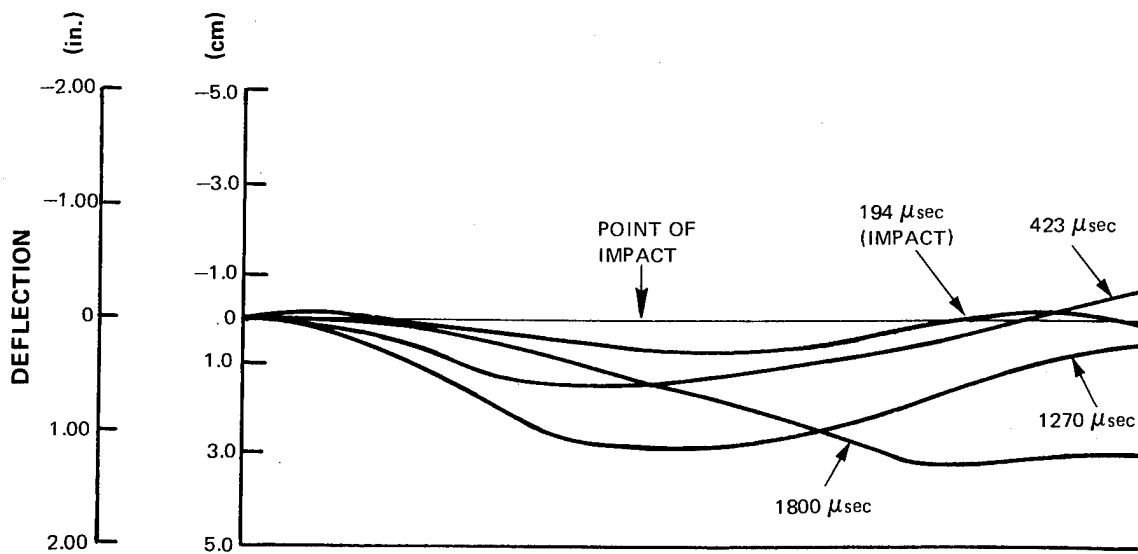
Figure 54   Deflection as a Function of Time for a Cantilevered $[(\pm 45)_2 \mid 0_{12} \mid (\mp 45)_2]_T$ Modmor II/PR-286 Composite Beam Impacted by 2.54 cm Diameter Gelatin at 61 m/sec
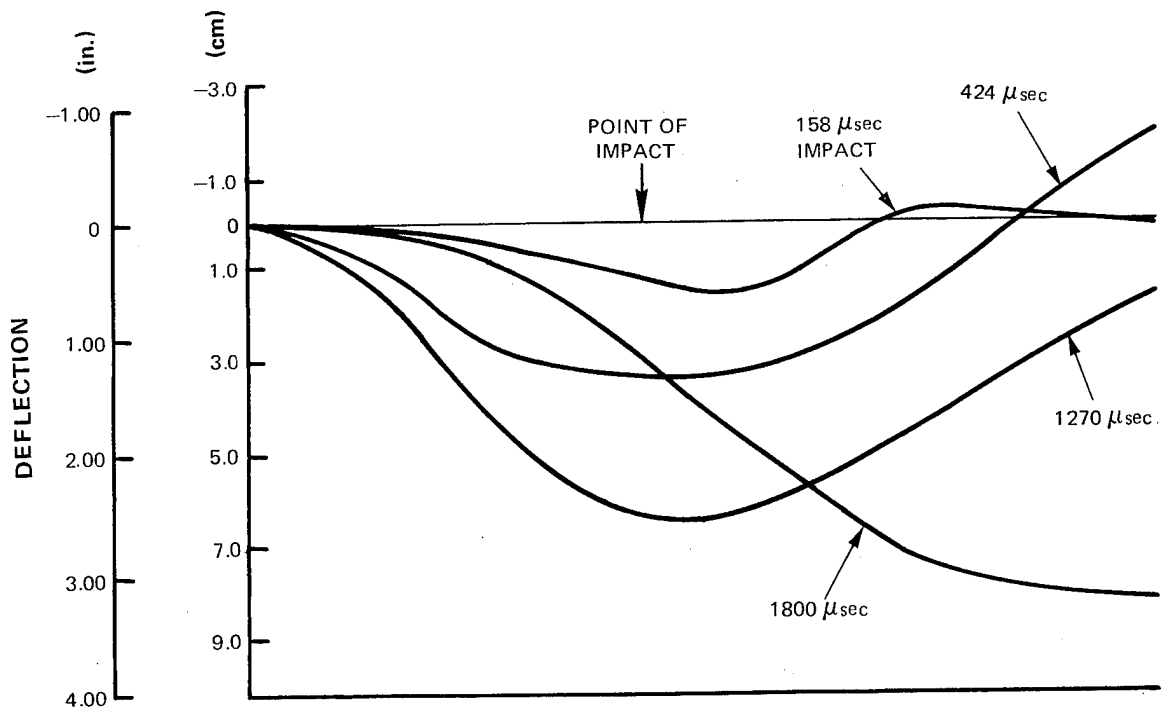
Figure 55   Deflection as a Function of Time for a Cantilevered $[(\pm 45)_2 \mid 0_{12} \mid (\mp 45)_2]_T$ Modmor II/PR-286 Composite Beam Impacted by 2.54 cm Diameter Gelatin at 152 m/sec
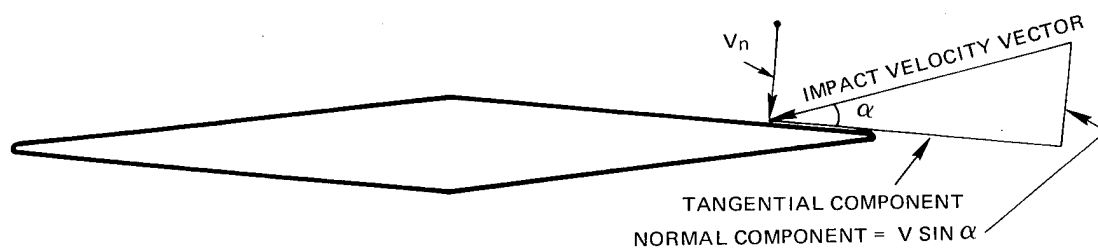
Figure 56   Resolution of Impacting Projectile Velocity Into Tangential and Normal Components

100
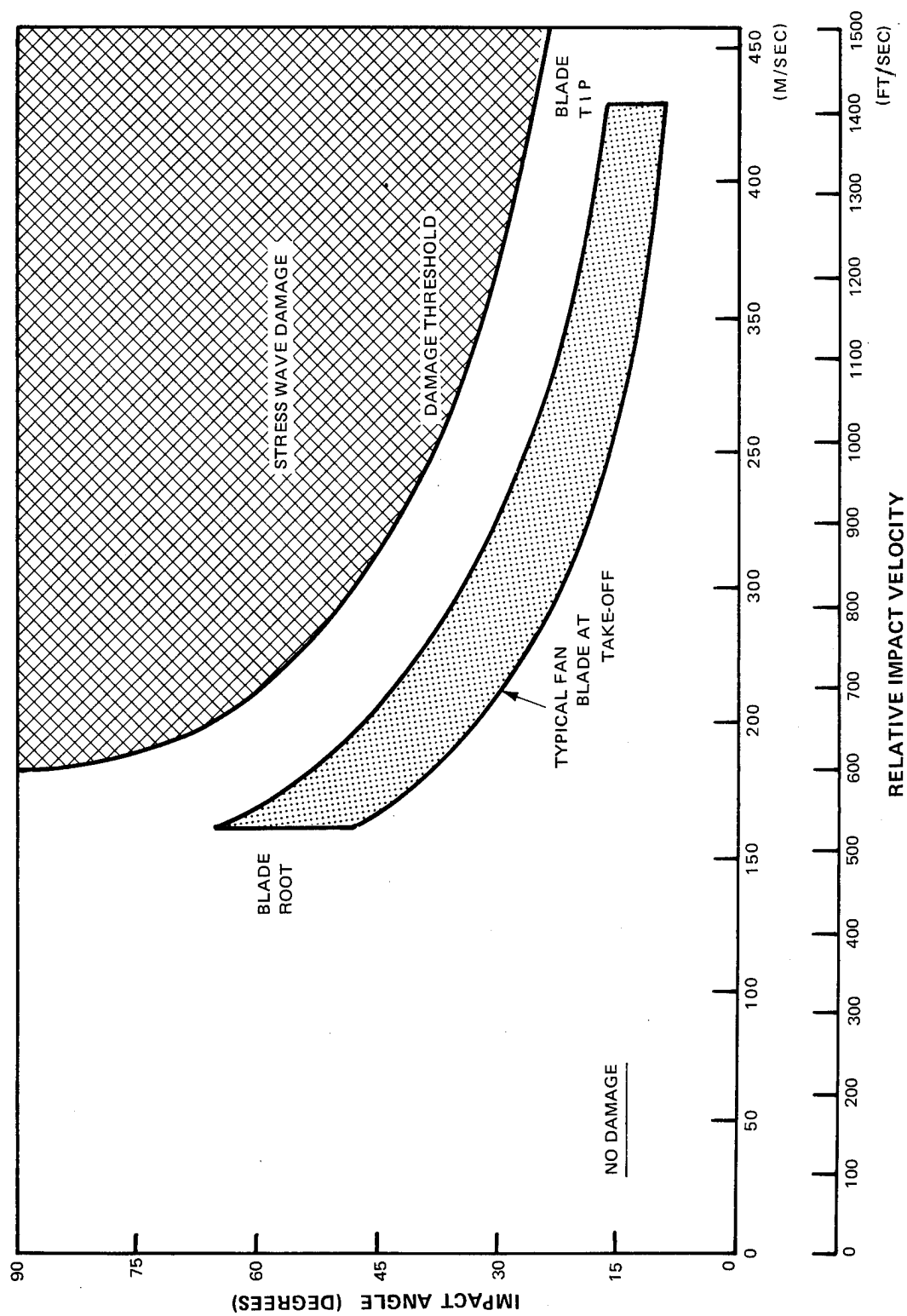
Figure 57   Damage Threshold as a Function of Relative Velocity and Impact Angle
for Gelatin Projectiles
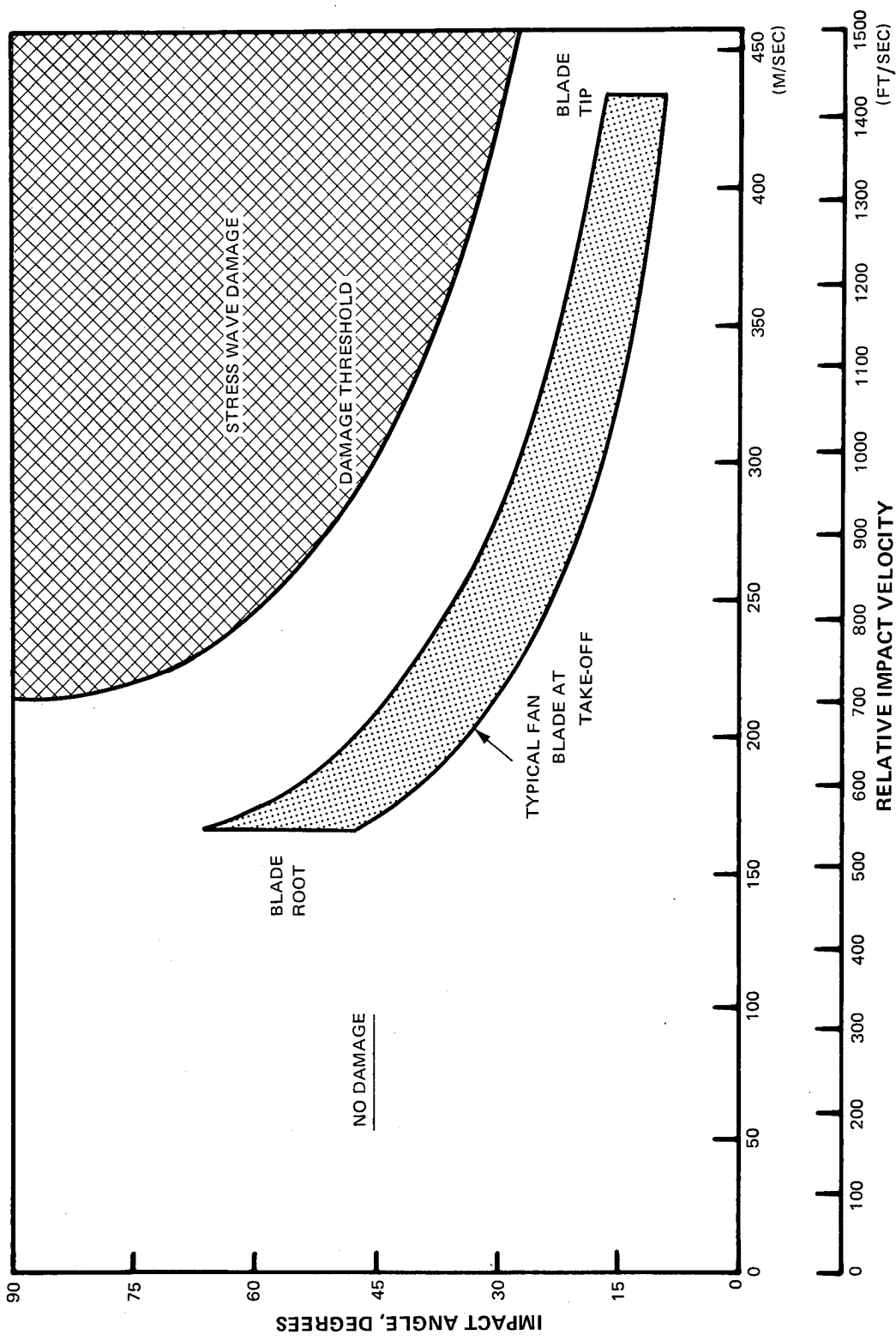
Figure 58   Damage Threshold as a Function of Relative Velocity and Impact Angle
for Ice Projectiles
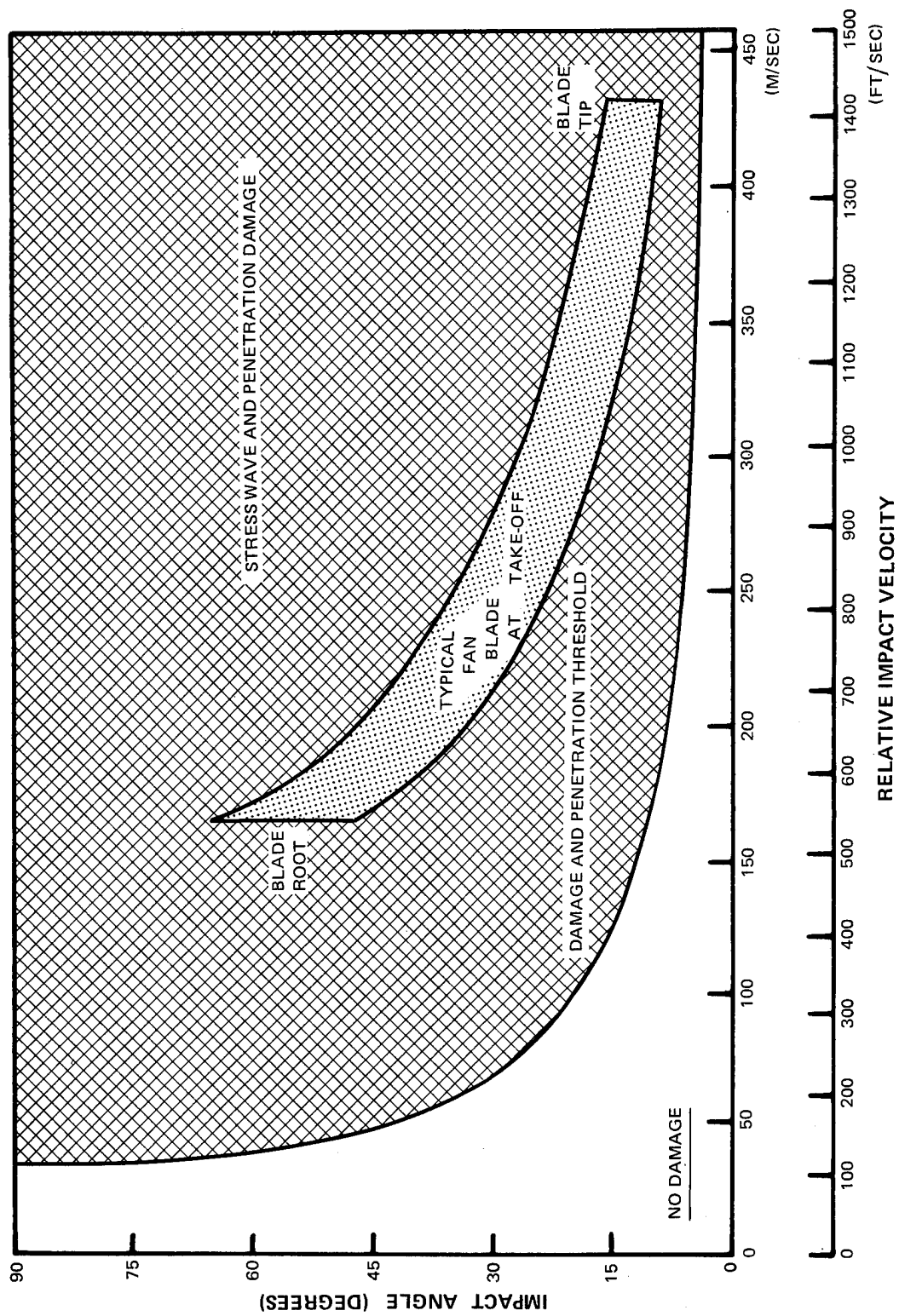
Figure 59   Damage Threshold as a Function of Relative Velocity and Impact Angle for Steel Projectiles

103

TABLE I

PR-286 COMPOSITES — UNIDIRECTIONAL COMPOSITE DATA

Fiber	Modmor II	Modmor II	Modmor II	Modmor I	T-75-S	Boron	S-Glass	PRD-49-1	S-Glass/T-75-S	PRD-49-1/T-75-S
Ave. Composite Density-g/cc	1.51	1.56	1.47	1.61	1.60	2.09	1.98	1.37	1.76	1.45
Ave. Void Content	1.0	1.4	1.2	1.7	0.3	1.1	0.8	1.9	1.0	
Ave. Fiber Vol. - %	55	65	47	53	59	55	59	63	{31(S-Glass) / 22(T-75-S)}	{~39 (PRD-49-1) / ~17(T-75-S)}
Longitudinal Tensile Strength $GN/m^2(10^3 psi)$	1.11(161)** / 1.01(146)*	1.01(149) / .99(143)	.90(130)* / .67(97)*	.89(129) / 1.01(146)	1.06(154) / 0.98(142)	1.53(222) / 1.41(205)	1.53(222) / 1.49(216)	1.17(170) / 1.06(154)	0.74(107) / 0.74(107)	.72(104) / .70(101)
Longtiudinal Tensile Modulus $GN/m^2(10^6 psi)$	130(18.9)** / 135(19.6)*	138(20.1) / 136(19.7)	125(18.2)* / 105(15.2)*	216(31.3) / 226(32.8)	270(39.2) / 263(38.2)	217(31.5) / 227(32.9)	49.6(7.2) / 50.3(7.3)	91.0(13.2) / 94.5(13.7)	134(19.5) / 135(19.6)	124 (18.0) / 123 (17.8)
Transverse Tensile Strength $MN/m^2(10^3 psi)$	40.0(5.8) / 41.4(6.0)	43.4(6.3) / 38.6(5.6)	51.0(7.4) / 50.3(7.3)	34.5(5.0) / 35.2(5.1)	31.0(4.5) / 26.2(3.8)	64.1(9.3) / 49.6(7.2)	96.5(14) / 82.7(12)	25.5(3.7) / 16.5(2.4)	38.6(5.6) / 42.1(6.1)	15.0(2.2) / 19.6(2.8)
Transverse Tensile Modulus $GN/m^2(10^6 psi)$	10.1 (1.46) / 9.24(1.34)	10.5(1.52) / 9.86 (1.43)	9.79(1.42) / 8.76(1.27)	6.96(1.01) / 6.69(0.97)	5.31(0.77) / 5.65(0.82)	29.0(4.20) / 26.2(3.80)	22.1(3.21) / 22.6(3.28)	6.27(0.91) / 5.93(0.86)	14.5(2.10) / 14.1(2.05)	5.92(.86) / 5.72(.83)
Beam Shear Strength (L/D = 4:1) $MN/m^2 (10^3 psi)$	71.0(10.3) / 64.8(9.4)	79.3(11.5) / 82.7(12.0)	83.4(12.1) / 81.4(11.8)	57.9(8.4) / 56.5(8.2)	53.8(7.8) / 53.8(7.8)	105(15.3) / 101(14.7)	96.5(14.0) / 86.9(12.6)	47.6(6.9) / 46.9(6.8)	22.8(3.3) / 22.1(3.2)	31.0(4.5) / 31.0(4.5)
Charpy Impact Strength joules (ft-lbs)	8.1(6.0) / 9.5(7.0)	5.4 (4.0) / 3.9 (2.9)	3.3(2.4) / 3.1(2.3)	3.3(2.4) / 3.7(2.7)	4.1(3.0) / 4.1(3.0)	11.5(8.5) / 11.5(8.5)	47.5(35.0) / 47.5(35.0)	17.6(13.0) / 17.6(13.0)	17.5(12.9) / 16.4(12.1)	10.6(7.8) / 11.7(8.6)
Torsion Rod Shear Strength $MN/m^2(10^3 psi)$	69.0(10.0) / 74.5(10.8)	69.6(10.1) / 91.7(13.3)	78.6(11.3) / 78.6(11.3)	49.6(7.2) / 46.9(6.8)	50.3(7.3) / 48.3(7.0)	88.3(12.8) / 91.0(13.2)	115.1(16.7) / 118(17.1)	34.5(5.0) / 27.6(4.0)	24.8(3.6) / 24.8(3.6)	22.8(3.3) / 25.5(3.7)
Shear Modulus $GN/m^2(10^6 psi)$	4.55(0.660) / 4.69(0.680)	5.25 (0.762) / 5.76(0.835)	4.27 (.620) / 4.77 (.697)	4.41(0.640) / 4.41(0.640)	3.32(0.481) / 3.11(0.451)	6.59(0.956) / 7.10(1.03)	5.72(0.830) / 6.21(0.900)	1.84(0.267) / 1.80(0.261)	4.73(.686) / 5.25(.762)	2.41(0.349) / 2.72(0.395)

*Average of 2 tests from one panel
**Average of 5 tests from one panel

TABLE II

MODMOR II/P13N COMPOSITES – UNIDIRECTIONAL COMPOSITE DATA

Composite Density -g/cc	1.56
Void Content	2.0
Ave. Fiber. Vol. - %	64
Longitudinal Tensile Strength $GN/m^2(10^3 psi)$	1.23(179) 1.29(187)
Longitudinal Tensile Modulus $GN/m^2(10^6 psi)$	148(21.4) 143(20.8)
Transverse Tensile Strength $MN/m^2(10^3 psi)$	29.6(4.3) 17.2(2.5)
Transverse Tensile Modulus $GN/m^2(10^6 psi)$	9.79(1.42) 9.52(1.38)
Beam Shear Strength (L/D = 4:1) $MN/m^2(10^3 psi)$	71.0(10.3) 81.4(11.8)
Charpy Impact Strength joules (ft-lbs)	8.5(6.3) 8.9(6.6)
Torsion Rod Shear Strength $MN/m^2(10^3 psi)$	31.0(4.5) 31.0(4.5)
Shear Modulus $GN/m^2(10^6 psi)$	3.86(0.56) 4.00(0.58)

TABLE III

MODMOR II/PR-286 MULTIDIRECTIONAL COMPOSITE DATA

Layup	Longitudinal Tensile Strength		Longitudinal Tensile Modulus		Transverse Tensile Strength		Transverse Tensile Modulus		Longitudinal Charpy Impact Strength	
	(MN/m^2)	$(10^3\ psi)$	(GN/m^2)	$(10^6\ psi)$	(MN/m^2)	$(10^3\ psi)$	(GN/m^2)	$(10^6\ psi)$	(joules)	(ft-lbs)
±45	104	15.1	16.8	2.44	—	—	—	—	12.5	9.2
	105	15.2	17.4	2.52	—	—	—	—	11.1	8.2
±30	458	66.4	51.7	7.5	71.7	10.4	11.7	1.69	9.4	6.9
	472	68.5	44.1	6.4	73.1	10.6	12.0	1.74	8.8	6.5
±45,0,±45	672	97.5	86.5	12.6	95.8	13.9	17.4	2.53	5.8	4.3
	696	101.0	86.5	12.6	77.2	11.2	18.7	2.71	5.8	4.3
±30,0,±30	651	94.5	98.7	14.3	46.9	6.8	12.5	1.81	4.7	3.5
	842	122.0	101.0	14.7	47.6	6.9	13.7	1.98	5.7	4.2
±72,±36,0,±36,±72	272	39.4	51.7	7.5	—	—	—	—	2.8	2.1
	314	46.3	49.6	7.2	—	—	—	—	4.1	3.0
Unidirectional	1,100**	161**	130**	18.9**	40.0	5.8	10.1	1.46	8.1	6.0
	1,010*	146*	135*	19.6*	41.4	6.0	9.24	1.34	9.5	7.0

*Average of two tests from one panel
**Average of five tests from one panel

TABLE IV

BALLISTIC IMPACT RESULTS FROM TASK I, PART A, "EFFECT OF PROJECTILE CHARACTERISTICS"

Projectile Type	Diameter (cm)	Specimen Number	Velocity (m/sec)	Mass (g)	Impact Energy (joules)	Extent of Damage[1] (%)	Visual Observations
Steel	0.64	976-3	51.5	1.06	1.4	5	Slight front face indentation; small back face protrusion and crack
		980-1	65.8	1.06	2.3	8	Slight front face indentation; small back face protrusion and crack
		980-2	95.4	1.06	4.8	7	Near penetration; light visible through splitting in back face
		976-4	97.5	1.06	5.0	4	Major front face indentation; back face protrusion and cracking
		980-3	122*	1.06	7.9	6	Near penetration; light visible through splitting in back face
		976-5	130	1.06	9.0	6	Near penetration, back face split nearly open
Steel	1.19	985-2	24	6.88	2.0	3	Very slight front face indentation; very slight back face protrusion
		981-5	33	6.88	3.7	5	Slight front face indentation; small back face protrusion and crack
		983-1	59	6.88	12.0	37	Near penetration; light visible through delamination and splitting in back face
		985-5	63	6.88	13.8	17	Near penetration; light visible through delamination and splitting in back face
		983-2	82	6.88	23.0	28	Penetration; extensive back face delamination and cracking
		982-3	100	6.88	34.2	24	Penetration; extensive back face delamination and cracking
Gelatin	1.27	984-4	161	1.08	14.0	0	No visible damage
		980-4	166	1.08	14.9	0	No visible damage
		984-5	208	1.08	23.4	33	Delamination in back face ±45° plies visible at both edges, at or near interface with unidirectional plies
		980-5	218	1.08	25.6	23	Delamination in back face ±45° plies visible along one edge, at or near interface with unidirectional plies
		976-2	274	1.08	38.3	52	Slight delamination and cracking at front and back faces; delamination in back face ±45° plies visible for approximately 9 cm along both edges, at or near interface with unidirectional plies
		981-1	283	1.08	43.2	37	Projectile beginning to penetrate: broken fibers, cracks and delamination in front and back faces, with split and broken unidirectional plies visible and slightly protruding at back face, and 2 x 4 cm portion of back ±45° plies torn off
Gelatin	2.54	985-4	64	8.55	17.5	0	No visible damage
		984-1	65	8.65	18.4	0	No visible damage
		982-2	68	8.62	19.9	0	No visible damage
		984-2	107	8.52	49.0	89	Delamination in unidirectional plies, near interface with back face ±45° plies, extends from tip to within 2.5 cm of gripped end. Nine cm segment of back face ±45° plies separated from specimen tip
		984-3	147	8.62	93.4	76	Flexural failure: multiple delaminations and complete fracture of specimen behind point of impact
		1025-1	154	8.77	104	89	Flexural failure: back face ±45° plies separated from specimen; multiple delaminations in unidirectional plies, with ply fractures behind impact point and at gripped end

TABLE IV (Cont'd)

Projectile Type	Diameter (cm)	Specimen Number	Velocity (m/sec)	Mass (g)	Impact Energy (joules)	Extent of Damage[1] (%)	Visual Observations
Ice	1.27	976-1	213	0.94	21.3	7	No visible damage
		981-2	226	0.99	25.2	0	No visible damage
		982-4	274	0.99	37.1	20	Delamination visible at one edge in back face ±45° plies, at or near interface between back face ±45° plies and unidirectional plies; slight back face crack
		981-3	279	0.99	38.5	9	Several cracks in back face
		982-5	306	0.99	46.4	12	Delamination and cracking in back face behind impact point
		981-4	317	0.99	49.7	31	Delamination visible at edges in back face ±45° plies, near the unidirectional plies; delamination and cracking of back face
Ice	2.54	983-3	64	7.95	16.1	0	No visible damage
		985-1	65	7.95	16.6	0	No visible damage
		983-4	106	7.95	44.7	0	No visible damage
		982-1	111	7.95	49.2	0	No visible damage
		985-3	145	7.95	83.3	74	Flexural failure: multiple delaminations and complete fracture of specimen behind point of impact; some penetration
		983-5	154	7.95	94.6	100	Multiple delaminations and fiber fractures behind point of impact; tip segment of back face ±45° plies separated from specimen

*Estimated from Calibration curve
[1] Area Fraction of Impacted Specimen Transmitting Less Than 20% of Signal

TABLE V

BALLISTIC IMPACT RESULTS FROM TASK 1, PART B, "EFFECT OF COMPOSITE PROPERTIES"

Projectile Type	Fiber*	Layup	Specimen Number	Velocity (m/sec)	Mass (g)	Impact Energy (joules)	Extent of Damage*** (%)	Visual Observations
1.27 cm Diameter Ice	Modmor I	$[O_{20}]_T$	1015-1	260	0.99	33.1	42	Specimen split longitudinally into 3 segments; multiple longitudinal inplane cracks and depression of surface visible at front face impact point; multiple interlaminar delamination noted in split region, extending from near grips to tip.
			1015-2	284**	0.99	39.9**	42	Specimen split longitudinally into 2 segments; several longitudinal inplane cracks and some depression of surface visible at front face impact point; interlaminar delamination noted near impact point.
	T-75-S	$[O_{18}]_T$	1005-1	260	0.99	33.1	32	Specimen split longitudinally into 2 segments; multiple longitudinal inplane cracks visible at front face impact point, plus some depression of surface; interlaminar delamination noted in split region, extending from tip to near grips.
		$[O_{18}]_T$	1017-1	293	0.99	42.5	49	Specimen split longitudinally into 2 segments; longitudinal inplane cracks, transverse cracks, interlaminar separations and depression of the surface at front face impact point.
	Modmor II	$[O_{20}]_T$	1002-1	262	0.99	33.6	16	Specimen split longitudinally into 2 segments; larger segment cracked longitudinally down entire length.
			1002-2	269**	0.99	35.8***	0.6	Cracked longitudinally down entire length.
	Modmor II/PI3N	$[O_{18}]_T$	1028-1	280	0.99	38.4	49	Specimen cracked longitudinally down entire length; surface depression and 3 smaller longitudinal cracks visible at front face impact point; protrusion and 1 longitudinal crack visible behind impact on back face.
			1028-2	281	0.99	39.1	26	Specimen cracked longitudinally from tip to within 4 cm of clamped end; additional smaller longitudinal cracks near point of impact.
	PRD-49-1	$[O_{20}]_T$	992-1	262	0.99	33.6	10	Multiple longitudinal inplane cracks; depression of front face at impact point.
			992-2	280**	0.99	38.8**	10	Longitudinal inplane crack extends from tip to within 2 cm of clamped end; additonal longitudinal cracks visible near impact point

* Matrix is PR-286 epoxy unless otherwise noted.
** Examination of specimen impacted face indicates ice ball break-up may have commenced prior to impact.
*** Area fraction of impacted specimen transmitting less than 20% of signal.

TABLE V (Cont'd)

Projectile Type	Fiber*	Layup	Specimen Number	Velocity (m/sec)	Mass (g)	Impact Energy (joules)	Extent of Damage**** (%)	Visual Observations
1.27 cm Diameter Ice	Boron	$[O_{23}]_T$	1001-1	258	0.99	32.6	1.2	Single longitudinal inplane crack extending from tip to 2.4 cm from grip end.
			1001-2	280	0.99	38.8	0.5	Single longitudinal inplane crack extending from tip to 5.5 cm from grip end.
	S-Glass	$[O_{27}]_T$	999-1	262	0.99	33.6	0.6	Single longitudinal inplane crack extending from tip to 3.1 cm from grip end.
			999-2	270	0.99	36.1	0.1	Single longitudinal inplane crack extending from tip to 3 cm from grip end.
	PRD-49-1	$[(\pm45)_4|O_8]_S$	1064-1	271**	0.99	36.4**	18	Slight indentation at front face; slight protrusion and internal delamination visible at back face.
	PRD-49-1	$[(\pm45)_4|O_8]_S$	1064-2	262	0.99	36.6	34	Indentation and cracking at front face; slight protrusion and internal delamination visible through back face, and as edge cracks at interface between unidirectional and back face ±45° plies.
	Boron	$[(\pm45)_2|O_6]_S$	1003-1	282	0.99	39.4	5.1	Some cracking and lifting of back face ±45° plies.
	Boron	$[(\pm45)_2|O_6]_S$	1003-2	284	0.99	39.9	6.8	Some cracking and lifting of back face ±45° plies.
	S-Glass	$[(\pm45)_3|O_6|\overline{O}]_S$	1034-1	283	0.99	38.3	0	No visible damage.
	S-Glass	$[(\pm45)_3|O_6|\overline{O}]_S$	1034-2	297**	0.99	43.4**	0	No visible damage
	Titanium-6Al-4V		#1	277	0.99	38.0	0	No visible damage
	Titanium-6Al-4V		#2	278	0.99	38.2	0	No visible damage.
	Titanium-6Al-4V		#8	289	0.99	41.3	0	No visible damage.

* Matrix is PR-286 epoxy unless otherwise noted.
** Examination of specimen impacted face indicates ice ball break-up may have commenced prior to impact.
*** Area fraction of impacted specimen transmitting less than 20% of signal.

110

TABLE VI

BALLISTIC IMPACT RESULTS FROM TASK I, PART C,
"EFFECT OF PLY CONFIGURATION, FIBER CONTENT, AND THICKNESS"
WITH MODMOR II/PR-286 GRAPHITE-EPOXY

Projectile Type	Mass (g)	Velocity (m/sec)	Impact Energy (joules)	Specimen Number	Fiber Volume (%)	Layup	Extent of Damage (%)*	Visual Observations
1.27 cm Diameter Ice	0.99	280	38.4	1044-1	47	$[0_8]_T$	1.1	Single longitudinal inplane crack extends from tip through impact point, to within 3.5 cm of grip end.
	0.99	263	33.9	1044-2	47	$[0_8]_T$	1.1	Single longitudinal inplane crack extends through point of impact to both ends.
	0.99	275	37.1	1041-1	65	$[0_{10}]_T$	1.1	Single longitudinal inplane crack extends from tip, through point of impact, to within 4 cm of grip end.
	0.99	275	37.1	1041-2	65	$[0_{10}]_T$	16	Single longitudinal inplane crack extends from tip, through point of impact, to within 1.2 cm of grip end; two shorter longitudinal cracks near point of impact.
	0.99	288	40.6	1007-1	57	$[(\pm30)_5]_s$	12.5	Two intersecting cracks at +30° and -30° to specimen longitudinal direction in back face behind impact point.
	0.99	294	42.8	1007-2	57	$[(\pm30)_5]_s$	16	Two intersecting cracks at +30° and -30° to specimen longitudinal direction in back face behind point of impact
	0.99	302**	44.7**	1033-1	57	$[(\pm45)_5]_T$	0.5	No visible damage.
	0.99	277 est.	39.4 est.	1033-2	57	$[(\pm45)_5]_T$	0	No visible damage.
	0.99	299***	43.8**	1009-1	57	$[(\pm30)_2 \vert 0_6]_s$	4.8	Back face crack to 30° to specimen longitudinal direction.
	0.99	268**	35.6**	1009-2	57	$[(\pm30)_2 \vert 0_6]_s$	1.4	No visible damage.
	0.99	274**	36.8**	1010-1	57	$[(0\vert+30\vert-30\vert0)_2]_s$	1.0	Small longitudinal crack in back face.
	0.99	282	39.4	1010-2	57	$[(0+30\vert0\vert-30)_2]_s$	0.1	No visible damage.
	0.99	273**	36.5***	1008-1	57	$[(\pm45)_2 \vert 0_6]_s$	2.7	Slight crack at 45° on back face.
	0.99	280	38.8	1008-2	57	$[(\pm45)_2 \vert 0_6]_s$	30	Two cracks at 45° on back face; delaminations visible in back face ±45° plies along edges, at or near interface with unidirectional plies.
	0.99	267**	34.9**	1012-2	57	Pseudo-isotropic	0	No visible damage.
	0.99	282	39.4	1012-2	57	Pseudo-isotropic	0.1	No visible damage.
	0.99	268**	35.2**	1011-1	57	$[(\pm45)_4 \vert 0_{12}]_s$	0	No visible damage.
	0.99	282	39.4	1011-2	57	$[(\pm45)_4 \vert 0_{12}]_s$	4.2	No visible damage.

* Area fraction of impacted specimen transmitting less than 20% of signal.
** Examination of strobe photograph and or lacquer pattern on specimen impacted face indicates ice ball break-up may have commenced prior to impact.

TABLE VII

BALLISTIC IMPACT RESULTS FROM TASK 1, PART D, "MATERIALS IMPACT IMPROVEMENT EVALUATION"

Projectile Type	Mass (g)	Velocity (m/sec)	Impact Energy (joules)	Specimen Number	Fiber	Layup	Extent of Damage (%)*	Visual Observations
1.27 cm Diameter Ice	0.99	276	37.7	1038-1	PRD,T-75-S	$[O_{20}]_T$	29	Specimen split into 2 segments; additional longitudinal inplane cracks and indentation visible on front face near point of impact
	0.99	274	37.1	1038-2	PRD,T-75-S	$[O_{20}]_T$	2.9	One complete longitudinal inplane split plus indentation and smaller longitudinal cracks near point of impact.
	0.99	289**	41.4**	1048-1	PRD,T-75-S	$[O_{20}]_T$	24	Two longitudinal inplane cracks extending nearly full length, plus indentation and smaller longitudinal cracks near point of impact.
	0.99	289	41.4	1063-1	S-Glass T-75-S	$[O_{14}]_T$	10	Single longitudinal crack extending from tip to within 3 cm of grip end, plus 4 smaller longitudinal cracks visible on front face near point of impact.
	0.99	296**	43.4**	1063-2	S-Glass T-75-S	$[O_{14}]_T$	22	Single longitudinal crack extending nearly full length, plus some indentation and smaller cracks near point of impact.

* Area fraction of impacted specimen transmitting less than 20% of signal.
** Examination of strobe photograph and/or lacquer pattern on specimen impacted face indicates ice ball break up may have commenced prior to impact

TABLE VIII

INITIAL PEAK IMPACT STRAIN RESULTS FROM TASK I, PART A, "EFFECT OF PROJECTILE CHARACTERISTICS"

| Specimen | Material | Layup | Projectile Characteristics | | Impact Strains (%)[a] | | | | | | | | | |
			Type	Velocity (m/sec)	Gage Number 1 / Orientation 0°	2 0°	3 0°	4 0°	5 0°	6 0°	7 90°	8 90°	9 45°	10 135°
976-3	Modmor II/PR-286	$[(\pm45)_2|0_{12}|(\mp45)_2]_r$	Steel	51.5	—	-.518[d]	—	-.069[d]	.059[d]	—	-.433[d]	-.132[d]	-.150[d]	-.174[d]
976-4	Modmor II/PR-286	$[(\pm45)_2|0_{12}|(\mp45)_2]_r$	Steel	97.5	—	—	—	-.014[d]	.037[d]	-.032[d]	-.311[d]	-.340[d]	-.063[d]	-.370[d]
976-5	Modmor II/PR-286	$[(\pm45)_2|0_{12}|(\mp45)_2]_r$	Steel	130	—	-.916[d]	—	—	.046[d]	—	-.473[d]	-.177[d]	-.103[d]	-.172[d]
985-2[b]	Modmor II/PR-286	$[(\pm45)_2|0_{12}|(\mp45)_2]_r$	Steel	24	—	—	.072	-.111	-.177	.090	-.073	-.234	-.089	-.153
985-5[b]	Modmor II/PR-286	$[(\pm45)_2|0_{12}|(\mp45)_2]_r$	Steel	63	—	-1.15	-.359	—	-.790	.126	—	-.170	-.106	-.070
982-3[b]	Modmor II/PR-286	$[(\pm45)_2|0_{12}|(\mp45)_2]_r$	Steel	100	—	-1.30	-1.44	—	-.099	.090	—	.783	-.662	—
976-1	Modmor II/PR-286	$[(\pm45)_2|0_{12}|(\mp45)_2]_r$	Ice	213[c]	.633	-.154	-.198	.263	-.101	-.166	.420	.254	.240	.252
982-4[b]	Modmor II/PR-286	$[(\pm45)_2|0_{12}|(\mp45)_2]_r$	Ice	274	—	.610	-.144	-.285	-.284	.179	1.10	-.437	-.354	—
982-5[b]	Modmor II/PR-286	$[(\pm45)_2|0_{12}|(\mp45)_2]_r$	Ice	306	—	-.630	-.251	-.426	-.284	.180	.364	-.624	—	—
982-1[b]	Modmor II/PR-286	$[(\pm45)_2|0_{12}|(\mp45)_2]_r$	Ice	111	.555	-.180	-.144	-.126	.071	.144	.365	-.312	-.189	-.278
984-4[b]	Modmor II/PR-286	$[(\pm45)_2|0_{12}|(\mp45)_2]_r$	Gelatin	161	.392	-.198	—	-.269	.283	.261	-.229	-.453	-.263	-.349
984-5[b]	Modmor II/PR-286	$[(\pm45)_2|0_{12}|(\mp45)_2]_r$	Gelatin	208	—	—	-.018	-.474	-.283	.269	.112	—	-.094	-.362
976-2	Modmor II/PR-286	$[(\pm45)_2|0_{12}|(\mp45)_2]_r$	Gelatin	274	—	—	—	-.823[d]	-.552[d]	-.150	—	1.44[d]	—	.648
982-2[b]	Modmor II/PR-286	$[(\pm45)_2|0_{12}|(\mp45)_2]_r$	Gelatin	68	.356	-.108	-.108	-.109	-.227	.090	.256	-.243	-.162	-.098

Projectile Characteristics — Diameter (cm):
- 976-3: .64
- 976-4: .64
- 976-5: .64
- 985-2[b]: 1.19
- 985-5[b]: 1.19
- 982-3[b]: 1.19
- 976-1: 1.27
- 982-4[b]: 1.27
- 982-5[b]: 1.27
- 982-1[b]: 2.54
- 984-4[b]: 1.27
- 984-5[b]: 1.27
- 976-2: 1.27
- 982-2[b]: 2.54

a. Initial peak amplitude strains measured from oscilloscope playbacks of tape recordings unless otherwise noted.
b. Strain gages are Micro-Measurements EA-06-125AC-350.
c. Estimated from calibration curve.
d. Strain measured from oscillograph photographs of tape playbacks.
e. Indicated strains were in excess of the ±1.5% strain range of the Micro-Measurements WD-DY-125AD-350 strain gages.

TABLE IX

INITIAL PEAK STRAIN RESULTS FROM TASK I, PARTS B, C AND D

Specimen	Material	Layup	Projectile Type	Impact Energy Joules	Damage Extent (%)	Gage Number*** Orientation	Impact Strains (%)*							
							1 0°	2 0°	3 0°	4 0°	5 0°	6 0°	7 90°	8 90°
Part B, "Effect of Composite Material Variables"														
1015-2	Modmor II/PR-286	[O₂₀]T	ICE	39.9**	42		--	--	--	--	--	--	-1.41	-.446
1017-1	T-75-S/PR-286	[O₁₈]T	ICE	42.5	49		1.23	.998	-.258	-.428	-.250	--	--	--
1002-2	Modmor II/PR-286	[O₂₀]T	ICE	35.8**	0.6		.464	-.285	.375	.250	-.285	-.142	.535	-.633
1028-2	Modmor II/P-13N	[O₁₈]T	ICE	39.1	26		.660	.624	-.339	-.321	.134	-.232	--	-1.19
992-2	PRD-49-1/PR-286	[O₂₀]T	ICE	38.8**	10		--	.232	--	--	-.508	-.277	--	-1.43
1001-1	Boron/PR-286	[O₂₃]T	ICE	32.6	1.2		--	--	--	-.285	-.142	--	-.232	-.384
999-2	S-Glass/PR-286	[O₂₇]T	ICE	36.1	0.1		1.48	-.508	-.633	-.570	.357	.178	--	--
Ti-6-4 #8	Titanium		ICE	41.3	0		--	-.303	-.446	.339	--	--	.553	-.303
Part C, "Effect of Ply Configuration and Thickness"														
1007-2	Modmor II/PR-286	[(±30)₅]S	ICE	42.8	16		--	--	--	-.250	.125	--	--	-.624
1033-2	Modmor II/PR-286	[(±45)₅]S	ICE	39.4 est.	0		.526	.570	.356	.285	-.285	--	.258	-.157
1009-2	Modmor II/PR-286	[(±30)₂ b₆]S	ICE	35.6**	1.4		.294	.232	.232	-.178	-.250	--	.499	-.258
1010-2	Modmor II/PR-286	[(0±30 b±30 b₂]S	ICE	39.4	0.1		.490	.454	-.178	-.178	-.285	--	.784	-.552
1012-2	Modmor II/PR-286	Pseudo-isotropic	ICE	39.4	0.1		.588	.660	.401	-.544	-.580	--	.552	.410
1011-2	Modmor II/PR-286	[(±45)₄ 0₁₂]S	ICE	39.4	4.2		.526	.428	-.187	-.303	-.196	--	.588	-.187
Part D, "Materials Impact Improvement Evaluation"														
1038-1	PRD, T-75-S/PR-286	[(O₂₀]T	ICE	37.7	29		--	--	--	--	--	--	--	-1.20
1063-1	S-Glass, T-75-S/PR-286	[O₁₄]T	ICE	41.4	10		.740	.668	--	-.206	--	--	--	--

* Initial peak amplitude strains measured from oscilloscope playbacks of tape recordings
** Ice-ball break-up may have commenced prior to impact
*** For location of strain gages refer to Figure 10.

114

TABLE X

PERCENT FREQUENCY CHANGE RESULTS AFTER IMPACT
FROM TASK I, PART A, "EFFECT OF PROJECTILE CHARACTERISTICS"
(All Specimens Are $[(\pm45)_2|0_{12}|\mp45)_2]_T$ Modmor II/PR-286)

Projectile/ Specimen	Impact Energy (Joules)	Extent of Damage	Percent Frequency Change****		
			First Bending	Second Bending	First Torsion
0.64 cm Steel					
976-3	1.4	5%	-16	-12.	*
980-1	2.3	8%	- 5	0	*
980-2	4.8	7%NP**	- 2	0	-4
976-4	5.0	4%	-14	- 9	-4
980-3	7.9	6%NP	0	- 2	-3
976-5	9.0	6%NP	-15	-11	-3
1.19 cm Steel					
985-2	2.0	3%	+ 1	- 1	+2
981-5	3.7	5%	- 4	- 4	*
983-1	12.0	37%NP	- 5	- 6	-27
985-5	13.8	17%NP	0	- 7	*
983-2	23.0	28%P***	- 5	- 7	*
982-3	34.2	24%P	- 5	- 4	-11
1.27 cm Ice					
976-1	21.3	7%	-17	-11	*
981-2	25.2	0%	- 3	- 4	*
982-4	37.1	20%	- 2	- 2	-9
981-3	38.5	9%	- 3	- 4	*
982-5	46.4	12%	- 1	- 2	-5
981-4	49.7	31%	- 3	+ 9	*
2.54 cm Ice					
983-3	16.1	0%	- 1	+10	0
985-1	16.6	0%	+ 1	0	0
983-4	44.7	0%	- 1	- 1	0
982-1	49.2	0%	0	0	0
985-3	83.3	74%	N.A.[1]	N.A.	N.A.
983-5	94.6	100%	N.A.	N.A.	N.A.

TABLE X (Cont'd)

Projectile/ Specimen	Impact Energy (Joules)	Extent of Damage	Percent Frequency Change****		
			First Bending	Second Bending	First Torsion
1.27 cm Gelatin					
984-4	14.0	0%	+ 2	0	0
980-4	14.9	0%	0	0	0
984-5	23.4	33%	0	- 1	-12
980-5	25.6	23%	---	+ 1	-10
976-2	38.3	52%	-14	-11	*
981-1	43.2	37%	- 9	- 6	*
2.54 cm Gelatin					
985-4	17.5	0%	+ 1	+ 1	*
984-1	18.4	0%	+ 4	+ 3	+2
982-2	19.9	0%	0	+ 1	*
984-2	49.0	89%	N.A.	N.A.	N.A
984-3	93.4	76%	N.A.	N.A.	N.A.
1025-1	104	89%	N.A.	N.A.	N.A.

---

*   Specimen Did Not Excite In First Torsion

**   Near Penetration

***   Penetration

****Natural Cantilever Bending Frequencies With 2.5 cm (1.0 in) Gripped. Torsion Determined With 95.7 Gram Weight Attached To Free End. Post Impact Frequencies Compensated By -11% In First And Second Bending And -3% In First Torsion.

1   Specimen Unsuitable For Frequency Testing After Impact

TABLE XI

PERCENT FREQUENCY CHANGE RESULTS AFTER IMPACT
FROM TASK I, PART B, "EFFECT OF COMPOSITE PROPERTIES"
(All Impacts With 1.27 cm Diameter Ice)

Fiber Type*	Layup	Specimen	Impact Energy (Joules)	Damage Extent	Percent Frequency Change[2]		
					First Bending	Second Bending	First Torsion
Modmor I	$[0_{20}]_T$	1015-1	33.1	42%	N.A.[1]	N.A.	N.A.
		1015-2	39.9**	42%	N.A.	N.A.	N.A.
T-75-S	$[0_{18}]_T$	1005-1	33.1	32%	N.A.	N.A.	N.A.
		1017-1	42.5	49%	N.A.	N.A.	N.A.
Modmor II	$[0_{20}]_T$	1002-1	33.6	16%	N.A.	N.A.	N.A.
		1002-2	35.8**	0.6%	-2	0	***
Mod II/P13N	$[0_{18}]_T$	1028-1	38.4	49%	N.A.	N.A.	N.A.
		1028-2	39.1	26%	+4	+1	***
PRD-49-1	$[0_{20}]_T$	992-1	33.6	10%	+1	+3	***
		992-2	38.8**	10%	-2	+2	***
Boron	$[0_{23}]_T$	1001-1	32.6	1.2%	+2	0	***
		1001-2	38.8	0.5%	+3	0	***
S-Glass	$[0_{27}]_T$	999-1	33.6	0.6%	+5	+4	***
		999-2	36.1	0.1%	+4	+4	***
PRD-49-1	$[(\pm45)_4 \mid 0_8]_S$	1064-1	36.4**	18%	+4	+2	***
		1064-2	36.6	34%	+4	+4	***
Boron	$[(\pm45)_2 \, 0_6]_S$	1003-1	39.4	5.1%	+3	+2	0
		1003-2	39.9	6.8%	+2	+2	0
S-Glass	$[(\pm45)_3 \, 0_6 \overline{0}]_S$	1034-1	38.3	0%	+2	+4	***
		1034-2	43.4**	0%	+5	+3	***

----

*   Resin Is 3M Company PR-286 Unless Otherwise Indicated.

**   Ice Ball Break-Up May Have Commenced Prior To Impact

***   Specimen Did Not Excite in Torsion

[1]   Post-Impacted Specimen Unsuitable For Impact Testing

[2]   Natural Cantilever Bending Frequencies With 2.5 cm (1.0 in) Gripped. Torsion Determined With 95.7 Gram Weight Attached To Free End.

TABLE XII

PERCENT FREQUENCY CHANGE RESULTS AFTER IMPACT FROM TASK I, PART C, "EFFECT OF PLY CONFIGURATION, FIBER CONTENT, AND THICKNESS" WITH MODMOR II/PR-286
(All Impacts With 1.27 cm Diameter Ice)

Specimen	Fiber Volume Fraction	Layup	Impact Energy (Joules)	Extent of Damage	Percent Frequency Change[***]		
					First Bending	Second Bending	First Torsion
1044-1	0.47	$[10_8]_T$	38.4	1.1%	+3	+4	*
1044-2	0.47	$[0_8]_T$	33.9	1.1%	+2	+3	*
1041-1	0.65	$[0_{10}]_T$	37.1	1.1%	-36	+4	*
1041-2	0.65	$[0_{10}]_T$	37.1	16%	+2	+2	*
1007-1	0.57	$[(\pm30)_5]_S$	40.6	12.5%	+4	+3	+3
1007-2	0.57		42.8	16%	+1	+4	+1
1033-1	0.57	$[(\pm45)_5]_T$	44.7**	0.5%	+2	+3	*
1033-2	0.57		39.4	0%	+2	+4	*
1009-1	0.57	$[(\pm30)_2\,0_6]_S$	43.8**	4.8%	+3	+7	+4
1009-2	0.57		35.6**	1.4%	+2	+4	+3
1010-1	0.57	$[(0\!+\!30\,0\!+\!30\,0)_2]_S$	36.8**	1.0%	0	+4	+3
1010-2	0.57		39.4	0.1%	+1	-18	+3
1008-1	0.57	$[(\pm45)_2\,0_6]_S$	36.5**	2.7%	+4	+3	+2
1008-2	0.57		38.8	30%	+4	+4	-3
1012-1	0.57	Pseudo-isotropic	34.9**	0%	+4	+4	+3
1012-2	0.57		39.4	0.1%	+3	-12	+2
1011-1	0.57	$[(\pm45)_4\,0_{12}]_S$	35.2**	0%	+4	+1	*
1011-2	0.57		39.4	4.2%	-4	+3	*

*   Specimen Did Not Excite In First Torsion

**   Ice Ball Break-Up May Have Commenced Prior To Impact

*** Natural Cantilever Bending Frequencies With 2.5cm (1.0 in) Gripped. Torsion Determined With 95.7 Gram Weight Attached To Free End.

TABLE XIII

PERCENT FREQUENCY CHANGE RESULSTS AFTER IMPACT
FROM TASK I, PART D, "MATERIALS IMPACT IMPROVEMENT
EVALUATION"
(All Impacts With 1.27 cm Diameter Ice)

Specimen	Fibers*	Layup	Impact Energy (Joules)	Extent of Damage	Percent Frequency Change[2]		
					First Bending	Second Bending	First Torsion
1038-1	PRD, T-75-S	$[0_{20}]_T$	37.7	29%	N.A.[1]	N.A.	N.A.
1038-2			37.1	29%	N.A.	N.A.	N.A.
1048-1			41.4**	24%	+1	+2	-3
1063-1	S-Glass, T-75-S	$[0_{14}]_T$	41.4	10%	+4	+4	***
1063-2			43.4**	22%	+4	+4	***

---

*   Resin Is 3M Company PR-286 Epoxy
**   Ice Ball Break-Up May Have Commenced Prior To Impact
***   Specimen Did Not Excite In Torsion
[1]   Post-Impacted Specimen Unsuitable For Frequency Testing
[2]   Natural Cantilever Bending Frequencies With 2.5 cm (1.0 in) Gripped. Torsion Determined With 95.7 Gram Weight Attached To Free End.

TABLE XIV

RESIDUAL TENSILE STRENGTH RESULTS
FROM TASK I, PART A, "EFFECT OF PROJECTILE CHARACTERISTICS"

Projectile/Specimen	Impact Energy (Joules)	Extent of Damage	Residual Tensile Strength (MN/m^2)	Fraction of Pre-Test*	Failure Location
No Impact					
1025-2	0	0%	724	>1.06	Tab Slipped
0.64 cm Steel					
976-3	1.4	5%	608	0.89	Gage
980-1	2.3	8%	441	0.65	Gage
980-2	4.8	7%NP**	448	0.66	Gage
976-4	5.0	4%	435	0.64	Gage
980-3	7.9	6%NP	505	0.74	Gage
976-5	9.0	6%NP	415	0.61	Gage
1.19 cm Steel					
985-2	2.0	3%	542	0.79	Gage
981-5	3.7	5%	406	0.59	Gage
983-1	12.0	37%NP	362	0.53	Gage
985-5	13.8	17%NP	352	0.51	Gage
983-2	23.0	28%P***	334	0.49	Gage
982.3	34.2	24%P	258	0.38	Gage
1.27 cm Ice					
976-1	21.3	7%	620	0.91	Gage
981-2	25.2	0%	595	0.87	Gage
982-4	37.1	20%	474	0.69	Gage
981-3	38.5	9%	520	0.76	Gage
982-5	46.4	12%	580	0.85	Gage
981-4	49.7	31%	417	0.61	Gage
2.54 cm Ice					
983-3	16.1	0%	566	0.83	Under Tab
985-1	16.6	0%	527	0.77	Under Tab
983-4	44.7	0%	561	0.82	Under Tab
982-1	49.2	0%	536	0.78	Under Tab
985-3	83.3	74%	0	0.0	Failed in Impact
983-5	94.6	100%	330	0.48	Gage

TABLE XIV (Cont'd)

Projectile/Specimen	Impact Energy (Joules)	Extent of Damage	Residual Tensile Strength (MN/m^2)	Fraction of Pre-Test*	Failure Location
1.27 cm Gelatin					
984-4	14.0	0%	665	0.97	Under Tab
980-4	14.9	0%	517	0.76	Under Tab
984-5	23.4	33%	407	0.60	Gage
980-5	25.6	23%	556	0.81	Gage
976-2	38.3	52%	380	0.56	Gage
981-1	43.2	37%	267	0.39	Gage
2.54 cm Gelatin					
985-4	17.5	0%	627	0.92	Gage
984-1	18.4	.0%	645	0.94	At Tab
982-2	19.9	0%	579	0.84	Under Tab
984-2	49.0	89%	427	0.62	Under Tab
984-3	93.4	76%	0	0.0	Failed in Impact
1025-1	104	89%	118	0.17	Gage

* Based Upon Average Longitudinal Tensile Strength of 682 MN/m^2 (99.2 Ksi) Reported for $[(\pm45) \mid 0_{12} \mid (\mp45)]_T$ Modmor II/PR-286 In Table III.

**Near Penetration

***Penetration

TABLE XV

RESIDUAL TENSILE STRENGTH RESULTS
FROM TASK I, PART B, "EFFECT OF COMPOSITE PROPERTIES"
(All Impacts With 1.27 cm Diameter Ice)

Fiber Type*	Layup	Specimen	Impact Energy (Joules)	Extent of Damage	Residual Tensile Strength (MN/m^2)	Fraction of Pre-Test***	Failure Location
Modmor I	$[0_{20}]_T$	1015-1	33.1	42%	No Test	–	Split
		1015-2	39.9**	42%	No Test	–	Split
T-75-S	$[0_{18}]_T$	1005-1	33.1	32%	No Test	–	Split
		1017-1	42.5	49%	No Test	–	Split
Modmor II	$[0_{20}]_T$	1002-1	33.6	16%	No Test	–	Split Under
		1002-2	35.8**	0.6%	675	0.67	Tab
Modmor II/P13N	$[0_{18}]_T$	1028-1	38.4	49%	No Test	–	Split
		1028-2	39.1	26%	1070	0.83	Gage
PRD-49-1	$[0_{20}]_T$	992-1	33.6	10%	765	0.69	Under Tabs
		992-2	38.8**	10%	846	0.76	Under Tabs
Boron	$[0_{23}]_T$	1001-1	32.6	1.2%	1000	0.68	Under Tabs
		1001-2	38.8	0.5%	1210	0.82	At Tab
S-Glass	$[0_{27}]_T$	999-1	33.6	0.6%	>1130	>0.75	Did Not Fail
		999-2	36.1	0.1%	>1280	>0.85	Did Not Fail
PRD-49-1	$[(\pm45)_4|0_8]_s$	1064-1	36.4**	18%	690	(2)	Gage
		1064-2	36.6	34%	616	(2)	Gage
Boron	$[(\pm45)_2|0_6]_s$	1003-1	39.4	5.1%	861	0.92 [1]	At Tab
		1003-2	39.9	6.8%	909	0.97 [1]	At Tab
S-Glass	$[(\pm45)_3|0_6|\bar{0}]_s$	1034-1	38.3	0%	771	(2)	Gage
		1034-2	43.4**	0%	875	(2)	Gage

*Resin Is 3M Company PR-286 Epoxy Unless Otherwise Indicated

** Ice Ball Break-up May Have Commenced Prior To Impact

***Based Upon Average Longitudinal Tensile Strengths Reported In Tables I and III.

(1) Based Upon An Estimated $[(\pm45)_2|0_6]_s$ Tensile Strength 937 MN/M^2 (136 KSI)

(2) No Base Line Tensile Strength Available

TABLE XVI

RESIDUAL TENSILE STRENGTH RESULTS
FROM TASK 1, PART C, "EFFECT OF PLY CONFIGURATION,
FIBER CONTENT, AND THICKNESS" WITH MODMOR II/PR-286
GRAPHITE-EPOXY

(All Impacts With 1.27 cm Diameter Ice)

Specimen	Fiber Volume (%)	Layup	Impact Energy (Joules)	Extent of Damage	Residual Tensile Strength (MN/m^2)	Fraction of Pre-Test*	Failure Location
1044-1	47	$[0_8]_T$	38.4	1.1%	608	0.77	Gage & Tab
1044-2	47	$[0_8]_T$	33.9	1.1%	690	0.88	Gage & Under Tab
1041-1	65	$[0_{10}]_T$	37.1	1.1%	>1010	>1.00	Did Not Fail
1041-2	65	$[0_{10}]_T$	37.1	16%	957	0.95	Under Tabs
1007-1	57	$[(\pm30)_5]_S$	40.6	12.5%	174	0.37	Gage
1007-2	57		42.8	16%	244	0.53	Under Tab
1033-1	57	$[(\pm45)_5]_T$	44.7**	0.5%	163	1.55	At Tab
1033-2	57		39.4	0%	154	1.47	Gage
1009-1	57	$[(\pm30)_2|0_6]_S$	43.8**	4.8%	498	0.67	Gage
1009-2	57		35.6**	1.4%	690	0.93	Gage
1010-1	57	$[(0+30b|30b)_2]_S$	36.8**	1.0%	536	0.72	At Tab
1010-2	57		39.4	0.1%	639	0.86	Under Tab

TABLE XVI (Cont'd)

Specimen	Fiber Volume (%)	Layup	Impact Energy (Joules)	Extent of Damage	Residual Tensile Strength (MN/m^2)	Fraction of Pre-Test*	Failure Location
1008-1	57	$[(\pm45)_2|0_6]S$	36.5**	2.7%	643	0.94	At Tab
1008-2	57		38.8	30%	558	0.82	Gage
1012-1	57	Pseudo-isotropic	34.9**	0%	320	1.09	Gage
1012-2	57		39.4	0.1%	340	1.15	Under Tab
1011-1	57	$[(\pm45)_4|0_{12}]S$	35.2**	0%	***	***	***
1011-2	57		39.4	4.2%	***	***	***

*Based Upon Average Longitudinal Tensile Strengths Reported in Tables I and III.

**Ice Ball Break-up May Have Commenced Prior To Impact

***Insufficient Gripping Area To Fail Specimens In Tension

TABLE XVII

RESIDUAL TENSILE STRENGTH RESULTS FROM TASK I, PART D, "MATERIALS IMPACT IMPROVEMENT EVALUATION"
(All Impacts With 1.27 cm Diameter Ice)

Specimen	Fibers*	Layup	Impact Energy (Joules)	Extent of Damage	Residual Tensile Strength (MN/m^2)	Fraction of Pre-Test***	Failure Location
1038-1	PRD,T-75-S	$[0_{20}]_T$	37.7	29%	No Test	—	Split
1038-2			37.1	29%	No Test	—	Split
1048-1			41.4**	24%	660	0.93	Gage
1063-1	S-Glass,T-75-S	$[0_{14}]_T$	41.4	10%	985	1.34	Shear Failure
1063-2			43.4**	22%	>765	>1.04	Tab Slipped

*   Resin Is 3M Company PR-286 Epoxy
**   Ice Ball Break-Up May Have Commenced Prior To Impact
*** Based Upon Average Tensile Strengths Given in Table I.

TABLE XVIII

BALLISTIC IMPACT RESULTS FROM TASK II, PART A. "EFFECT OF PLY CONFIGURATION" (All Impacts with 1.27 cm Diameter Gelatin)

Test Specimen	Material	Ply Configuration	Projectile Velocity (m/sec)	Impact Location	Ultrasonic Material Removal (%)	Damage Extent (%)	Visual Observations
NAS-13	Modmor II/PR-286	$0°, \pm 45°$	296	$15°$ - LE	0.4	1.2	A 1.2 cm long by 0.3 cm deep segment removed from leading edge.
NAS-11	Modmor II/PR-286	$0°, \pm 45°$	274*	$15°$ - LE	0.1	1.1	A 0.7 cm long by 0.4 cm deep segment removed from leading edge.
NAS-2	Modmor II/PR-286	$0°, \pm 45°$	260	$15°$ - QC	0	0	No visible damage.
NAS-3	Modmor II/PR-286	$0°, \pm 45°$	283	$15°$ - QC	0	0	No visible damage.
NAS-41	Modmor II/PR-286	$0°, 90°$	266	$15°$ - LE	0	0	No visible damage.
NAS-42	Modmor II/PR-286	$0°, 90°$	291	$15°$ - LE	0	0	No visible damage.
NAS-43	Modmor II/PR-286	$0°, 90°$	273	$15°$ - QC	0	0	No visible damage.
NAS-44	Modmor II/PR-286	$0°, 90°$	292	$15°$ - QC	0	0	No visible damage.
NAS-100	Ti-6Al-4V	--	294	$15°$ - LE	0	0	No visible damage.
NAS-107	Ti-6Al-4V	--	262	$15°$ - LE	0	0	No visible damage.

*Velocity estimated from calibration curve.

TABLE XIX

BALLISTIC IMPACT RESULTS FROM TASK II, PART B, "EFFECT OF PROJECTILE CHARACTERISTICS, AND IMPACT LOCATION AND ANGLE"

Test Specimen	Material	Configuration	Projectile			Impact Location	Ultrasonic		Visual Observation
			Type	Dia. (cm)	Velocity (m/sec)		Material Removal (%)	Damage Extent (%)	
NAS-15	Modmor II/PR-286	0°, ±45°	Ice	1.27	274*	0° - LE	0	0	No visible damage.
NAS-16	Modmor II/PR-286	0°, ±45°	Ice	1.27	278	0° - LE	0	0	No visible damage.
NAS-17	Modmor II/PR-286	0°, ±45°	Steel	0.64	274*	0° - LE	0.6	3.3	Leading edge penetrated to depth of 1.6 cm in chordwise direction.
NAS-18	Modmor II/PR-286	0°, ±45°	Steel	0.64	274*	0° - LE	0	2.6	Glancing impact. A 0.3 cm square portion of leading edge removed with fiber breakage and delamination visible along back side.
NAS-24	Modmor II/PR-286	0°, ±45°	Gelatin	1.27	272	0° - LE	0	0	No visible damage.
NAS-25	Modmor II/PR-286	0°, ±45°	Gelatin	1.27	264	0° - LE	0	0	No visible damage.
NAS-26	Modmor II/PR-286	0°, ±45°	Ice	1.27	274*	15° - LE	0.4	2.6	A 1.2 cm long by 0.5 cm deep segment removed from leading edge. Delamination along back side.
NAS-27	Modmor II/PR-286	0°, ±45°	Ice	1.27	277	15° - LE	0	0.6	Delamination and fiber breakage on back side of leading edge.
NAS-30	Modmor II/PR-286	0°, ±45°	Steel	0.64	274*	15° - LE	0.1	0.6	Leading edge penetrated to depth of 0.7 cm in chordwise direction.
NAS-34	Modmor II/PR-286	0°, ±45°	Ice	1.27	285	30° - LE	1.3	4.3	A 3.3 cm long by 0.7 cm deep segment removed from leading edge. Delamination on back side.
NAS-35	Modmor II/PR-286	0°, ±45°	Ice	1.27	269	30° - LE	0.7	4.9	A 1.0 cm square segment of leading edge removed. Delamination on back side.
NAS-37	Modmor II/PR-286	0°, ±45°	Steel	0.64	274*	30° - LE	0.1	0.8	A 0.7 cm square segment of leading edge removed.

TABLE XIX (Cont'd)

Test Specimen	Material	Configuration	Projectile				Ultrasonic		Visual Observation
			Type	Dia. (cm)	Velocity (m/sec)	Impact Location	Material Removal (%)	Damage Extent (%)	
NAS-39	Modmor II/PR-286	0°, ±45°	Steel	0.64	274*	30° - LE	0.6	1.0	Leading edge penetrated to depth of 1.0 cm in chordwise direction.
NAS-40	Modmor II/PR-286	0°, ±45°	Gelatin	1.27	282	30° - LE	1.1	5.6	A 1.5 cm long by 0.9 cm deep segment removed from leading edge. Delamination on back side.
NAS-45	Modmor II/PR-286	0°, ±45°	Gelatin	1.27	292	30° - LE	1.3	6.0	2 cm wide by 1 cm deep portion of leading edge removed.
NAS-4	Modmor II/PR-285	0°, ±45°	Ice	1.27	274*	15° - QC	N.A.	N.A.	Ice failed to impact in proper location.
NAS-7	Modmor II/PR-286	0°, ±45°	Ice	1.27	283	15° - QC	0	0-	No visible damage.
NAS-8	Modmor II/PR-286	0°, ±45°	Steel	0.64	274*	15° - QC	0.4	4.9	A 0.5 cm wide by 0.9 cm chordwise hole at quarter chord location. Lifting and delamination of back face plies.
NAS-9	Modmor II/PR-286	0°, ±45°	Steel	0.64	274*	15° - QC	0.9	8.1	Leading edge intact. A 0.5 cm wide hole extends chordwise between 1.0 cm and 2.5 cm from leading edge. Delamination and ply lifting at back face.
NAS-28	Modmor II/PR-286	0°, ±45°	Steel	0.64	274*	15° - QC	0.4	5.6	A 0.6 cm wide hole extends chordwise between 1.5 cm and 2.6 cm from leading edge. Delamination and ply lifting at back face.
NAS-101	Ti-6Al-4V	- - -	Ice	1.27	268	0° - LE	0	0	No visible damage.
NAS-103	Ti 6Al-4V	- - -	Ice	1.27	271	0° - LE	0	0	No visible damage.
NAS-104	Ti-6Al-4V	- - -	Steel	0.64	274*	0° - LE	0	0.8	Leading edge indented and creased 0.7 cm back from edge on impacted side. Back side reveals 0.3 cm crack perpendicular to leading edge.
NAS-105	Ti-6Al-4V	- - -	Steel	0.64	274*	0° - LE	0	0.5	Leading edge indented and creased 0.8 cm back from leading edge on impacted side. Back side crack extends 0.4 cm perpendicular to edge.

TABLE XIX (Cont'd)

Test Specimen	Material	Configuration	Projectile Type	Dia. (cm)	Velocity (m/sec)	Impact Location	Ultrasonic Material Removal (%)	Damage Extent (%)	Visual Observation
NAS-108	Ti-6Al-4V	– –	Gelatin	1.27	279	0° - LE	0	0	No visible damage.
NAS-109	Ti-6Al-4V	– –	Gelatin	1.27	263	0° - LE	0	0	No visible damage.
NAS-110	Ti-6Al-4V	– –	Ice	1.27	274*	15° - LE	0	0	No visible damage.
NAS-111	Ti-6Al-4V	– –	Ice	1.27	280	15° - LE	0	0	No visible damage.
NAS-112	Ti-6Al-4V	– –	Steel	0.64	274*	15° - LE	0	0.4	Crease extends from 0.1 to 1.1 cm from leading edge, visible as protrusion at back side.
NAS-113	Ti-6Al-4V	– –	Steel	0.64	274*	15° - LE	0	1.8	Leading edge severely indented and torn. Crease extends 1.2 cm perpendicular to edge.
NAS-102	Ti-6Al-4V	– –	Ice	1.27	279	15° - QC	0	0	No visible damage.
NAS-106	Ti-6Al-4V	– –	Ice	1.27	286	15° - QC	0	0	No visible damage.
NAS-114	Ti-6Al-4V	– –	Steel	0.64	274*	15° - QC	0	0.3	Crease extending from 0.7 cm to 1.5 cm perpendicular to leading edge.
NAS-115	Ti-6Al-4V	– –	Steel	0.64	274*	15° - QC	0	0.1	Small crease extending from 1.8 cm to 2.3 cm perpendicular to leading edge.
NAS-118	Ti-6Al-4V	– –	Gelatin	1.27	292	15° - QC	0	0	No visible damage.
NAS-119	Ti-6Al-4V	– –	Gelatin	1.27	289	15° - QC	0	0	No visible damage.

*Velocity estimated from calibration curve.

TABLE XX

INITIAL PEAK STRAIN RESULTS FROM TASK II INSTRUMENTED IMPACT SPECIMENS

Specimen	Material	Ply Configuration	Projectile Type*	Impact Location	Ultrasonic Extent of Damage	Initial Peak Strains (%)**			
					Gage Number: Orientation:	1 90°	2 90°	3 90°	4 0°
NAS-108	Ti-6Al-4V	-----	Gelatin	0° - LE	0%	0.008	-0.008	-0.024	-0.008
- 24	Modmor II/PR-286	0, ±45	Gelatin	0° - LE	0%	0.018	0.006	-0.004	-0.021
- 15	Modmor II/PR-286	0, ±45	Ice	0° - LE	0%	0.032	0.022	0.012	0.020
- 18	Modmor II/PR-286	0, ±45	Steel	0° - LE	2.6%	0.960	0.200	0.240	0.120
-107	Ti-6Al-4V	-----	Gelatin	15° - LE	0%	0.320	0.128	-0.176	-0.136
- 13	Modmor II/PR-286	0, ±45	Gelatin	15° - LE	1.2%	0.672	0.240	-0.272	0.192
- 41	Modmor II/PR-286	0, 90	Gelatin	15° - LE	0%	0.512	0.192	0.272	0.176
- 26	Modmor II/PR-286	0, ±45	Ice	15° - LE	2.6%	0.600	0.208	0.256	0.014
- 28	Modmor II/PR-286	0, ±45	Steel	15° - LE	5.6%	+ OFF SCALE	- OFF SCALE	+ OFF SCALE	0.240
- 40	Modmor II/PR-286	0, ±45	Gelatin	30° - LE	5.6%	1.120	0.352	-0.360	0.208
- 34	Modmor II/PR-286	0, ±45	Ice	30° - LE	4.3%	0.440	0.208	0.208	0.160
- 37	Modmor II/PR-286	0, ±45	Steel	30° - LE	0.8%	-0.160	-0.040	0.040	-0.040
-118	Ti-6Al-4V	0, ±45	Gelatin	15° - QC	0%	-0.048	0.024	0.064	0.048
- 2	Modmor II/PR-286	0, ±45	Gelatin	15° - QC	0%	-0.102	0.064	0.160	0.048
- 43	Modmor II/PR-286	0, 90	Gelatin	15° - QC	0%	-0.088	0.052	-0.104	0.048
- 4	Modmor II/PR-286	0, ±45	Ice	15° - QC	N.A.	0.112	0.088	0.256	0.064
- 8	Modmor II/PR-286	0, ±45	Steel	15° - QC	4.9%	+OFF SCALE	0.560	-0.232	0.136

* Projectile masses: gelatin 1.08 g; ice 0.99 g; steel 1.06 g. Projectile diameters (spherical): gelatin and ice 1.27 cm; steel 0.64 cm. Projectile velocities approximately 274 m/sec (900 fps) all impacts.

** Initial (0 to 500 μ sec) Peak Amplitude Strains measured from on line oscilloscope photographs.

TABLE XXI

BALLISTIC IMPACT RESULTS FROM TASK II, PART A,
"EFFECT OF PLY CONFIGURATION"
(All Impacts with 1.27 cm Diameter Gelatin)

Test Specimen	Material	Ply Configuration	Projectile Velocity (m/sec)	Impact Location	Ultrasonic Material Removal (%)	Ultrasonic Damage Extent (%)	First Bending	Second Bending	First Torsion
							Per Cent Frequency Change		
NAS-13	Modmor II/PR-286	0°, ±45°	296	15° - LE	0.4	1.2	+2	+2	0
NAS-11	Modmor II/PR-286	0°, ±45°	274*	15° - LE	0.1	1.1	+1	+3	-4
NAS- 2	Modmor II/PR-286	0°, ±45°	260	15° - QC	0	0	-1	-1	+2
NAS- 3	Modmor II/PR-286	0°, ±45°	283	15° - QC	0	0	+1	0	0
NAS-41	Modmor II/PR-286	0°, 90°	266	15° - LE	0	0	-1	-1	0
NAS-42	Modmor II/PR-286	0°, 90°	291	15° - LE	0	0	+1	+2	0
NAS-43	Modmor II/PR-286	0°, 90°	273	15° - QC	0	0	0	+1	0
NAS-44	Modmor II/PR-286	0°, 90°	292	15° - QC	0	0	0	0	0
NAS-100	Ti-6Al-4V	------	294	15° - LE	0	0	-1	-2	-4
NAS-107	Ti-6Al-4V	------	262	15° - LE	0	0	0	0	0

*Velocity estimated from calibration curve.

131

TABLE XXII
BALLISTIC IMPACT RESULTS FROM TASK II, PART B,
"EFFECT OF PROJECTILE CHARACTERISTICS, AND IMPACT LOCATION AND ANGLE"

Test Specimen	Material	Configuration	Projectile Type	Dia (cm)	Velocity (m/sec)	Impact Location	Ultrasonic Material Removal (%)	Ultrasonic Damage Extent (%)	First Bending	Second Bending	First Torsion
NAS-15	Modmor II/PR-286	0°, ±45°	Ice	1.27	274*	0° - LE	0	0	-1	-5	-2
NAS-16	Modmor II/PR-286	0°, ±45°	Ice	1.27	278	0° - LE	0	0	+1	-5	+4
NAS-17	Modmor II/PR-286	0°, ±45°	Steel	0.64	274*	0° - LE	0.6	3.3	+1	0	-2
NAS-18	Modmor II/PR-286	0°, ±45°	Steel	0.64	274*	0° - LE	0	2.6	+2	-1	-2
NAS-24	Modmor II/PR-286	0°, ±45°	Gelatin	1.27	272	0° - LE	0	0	0	+1	0
NAS-25	Modmor II/PR-286	0°, ±45°	Gelatin	1.27	264	0° - LE	0	0	+1	+1	+6
NAS-26	Modmor II/PR-286	0°, ±45°	Ice	1.27	274*	15° - LE	0.4	2.6	-1	-1	-2
NAS-27	Modmor II/PR-286	0°, ±45°	Ice	1.27	277	15° - LE	0	0.6	0	+1	+2
NAS-30	Modmor II/PR-286	0°, ±45°	Steel	0.64	274*	15° - LE	0.1	0.6	0	+1	+2
NAS-34	Modmor II/PR-286	0°, ±45°	Ice	1.27	285	30° - LE	1.3	4.3	-1	-1	0
NAS-35	Modmor II/PR-286	0°, ±45°	Ice	1.27	269	30° - LE	0.7	4.9	-2	-5	0
NAS-37	Modmor II/PR-286	0°, ±45°	Steel	0.64	274*	30° - LE	0.1	0.8	+1	+1	-2
NAS-39	Modmor II/PR-286	0°, ±45°	Steel	0.64	274*	30° - LE	0.6	1.0	-1	+2	-2
NAS-40	Modmor II/PR-286	0°, ±45°	Gelatin	1.27	282	30° - LE	1.1	5.6	0	0	-3
NAS-45	Modmor II/PR-286	0°, ±45°	Gelatin	1.27	292	30° - LE	1.3	6.0	0	0	0
NAS-4	Modmor II/PR-285	0°, ±45°	Ice	1.27	274*	15° - QC	***	***	+2	+1	+2
NAS-7	Modmor II/PR-286	0°, ±45°	Ice	1.27	283	15° - QC	0	0	+2	+3	+7
NAS-8	Modmor II/PR-286	0°, ±45°	Steel	0.64	274*	15° - QC	0.4	4.9	+2	-2	+3
NAS-9	Modmor II/PR-286	0°, ±45°	Steel	0.64	274*	15° - QC	0.9	8.1	+2	-1	+2
NAS-28	Modmor II/PR-286	0°, ±45°	Steel	0.64	274*	15° - QC	0.4	5.6	+2	-1	-5
NAS-101	Ti-6Al-4V	------	Ice	1.27	268	0° - LE	0	0	-1	-1	0
NAS-103	Ti-6Al-4V	------	Ice	1.27	271	0° - LE	0	0	0	-1	0
NAS-104	Ti-6Al-4V	------	Steel	0.64	274*	0° - LE	0	0.8	-1	0	+1
NAS-105	Ti-6Al-4V	------	Steel	0.64	274*	0° - LE	0	0.5	-1	-1	-2
NAS-108	Ti-6Al-4V	------	Gelatin	1.27	279	0° - LE	0	0	0	0	**
NAS-109	Ti-6Al-4V	------	Gelatin	1.27	263	0° - LE	0	0	0	-1	0
NAS-110	Ti-6Al-4V	------	Ice	1.27	274*	15° - LE	0	0	-2	-1	**
NAS-111	Ti-6Al-4V	------	Ice	1.27	280	15° - LE	0	0	0	-1	0
NAS-112	Ti-6Al-4V	------	Steel	0.64	274*	15° - LE	0	0.4	0	0	0
NAS-113	Ti-6Al-4V	------	Steel	0.64	274*	15° - LE	0	1.8	-5	-6	0
NAS-102	Ti-6Al-4V	------	Ice	1.27	279	15° - QC	0	0	0	-1	**
NAS-106	Ti-6Al-4V	------	Ice	1.27	286	15° - QC	0	0	0	-1	+4
NAS-114	Ti-6Al-4V	------	Steel	0.64	274*	15° - QC	0	0.3	-3	+2	+6
NAS-115	Ti-6Al-4V	------	Steel	0.64	274*	15° - QC	0	0.1	+3	-4	**
NAS-118	Ti-6Al-4V	------	Gelatin	1.27	292	15° - QC	0	0	-1	0	**
NAS-119	Ti-6Al-4V	------	Gelatin	1.27	289	15° - QC	0	0	0	-2	**

*Velocity estimated from calibration curve.
**Specimen did not excite in torsion.
***Projectile failed to impact specimen in proper location.

TABLE XXIII

TASK II ROTATING ARM IMPACT TESTING – PART C EFFECT OF APPLIED STRESS AND PROTECTION SCHEME

Specimen NAS	Material	Leading Edge Shield	Projectile Type	Projectile Diameter (cm)	Angle And Location	Relative Velocity* (m/sec)	Temp (°K)	Visual Inspection
(1) EFFECT OF LEADING EDGE SHIELD								
31	MII/286	No	Steel	0.64	15°-LE	275	344	Hit just behind leading edge. Hole 0.5 cm wide extends chordwise from 0.5 cm to 2.3 cm from leading edge. Delamination visible at impact and back faces.
22	MII/286	Yes	Steel	0.64	15°-LE	274	344	Direct hit on leading edge penetrated 0.8 cm deep into leading edge insert. No visible damage to composite or debonding of sheath visible near point of impact.
29	MII/286	Yes	Steel	0.64	15°-LE	274,274	344	Two separate glancing impacts at midchord. Gashes 1.1 cm long and 1.3 cm long on impact face. Loss of ±45° plies and delamination visible at midchord on back face.
49	MII/286	No	Ice	1.27	30°-LE	275	353	A 1.3 cm wide by 0.4 cm deep triangular piece removed from leading edge, delamination at back face. Smaller secondary impact closer to root apparently from debris.
47	MII/286	Yes	Ice	1.27	30°-LE	273	317	No visible damage due to impact.
6	MII/286	Yes	Ice	1.27	30°-LE	275	361	A 2.0 cm wide segment of leading edge foil bent back into insert. No visible damage to composite.
21	MII/286	No	Gelatin	1.27	30°-LE	274	349	A 2.0 cm wide by 0.9 cm deep segment removed from leading edge, with delamination visible 0.4 cm and 1.5 cm along leading edge beyond removed segment.
46	MII/286	Yes	Gelatin	1.27	30°-LE	275	349	No visible damage due to impact.
50	MII/286	Yes	Gelatin	1.27	30°-LE	275	356	No visible damage to specimen. Slight sheath debond along edge behind impact.
101	Ti-6Al-4V	–	Steel	0.64	15°-LE	254	336	Direct hit on leading edge 0.5 cm wide by 0.2 cm semicircular duct in leading edge.
103	Ti-6Al-4V	–	Steel	0.64	15°-LE	274	336	Three 0.2 cm longitudinal cracks located at 0.3 cm, 0.5 cm, and 0.7 cm chordwise from edge on back face. 0.3 cm wide indentation extends 1.3 cm chordwise from leading edge on impact face.
(2) EFFECT OF MASS								
10	MII/286	Yes	Steel	0.64	15°-LE	400	416	No impact. Sheath debonded due to high temperature.
5	MII/286	Yes	Steel	1.27	15°-LE	275	349	0.7 cm wide by 0.2 cm deep semicircular dent in leading edge.
36	MII/286	Yes	Ice	2.54	30°-LE	274	361	Leading edge bent 0.4 cm towards back face at point of impact.
48	MII/286	Yes	Ice	2.54	30°-LE	274	349	Leading edge bent 0.4 cm towards back face at point of impact.
33	MII/286	Yes	Gelatin	2.54	30°-LE	275	353	Leading edge bent 0.1 cm towards back face at point of impact. Rebound impact with projectile caused delamination and partial removal of 1 cm wide by 6 cm long portion of trailing edge tip.
38	MII/286	Yes	Gelatin	2.54	30°-LE	275	361	Leading edge bent plus partial sheath debond near root, and extensive specimen delamination on back face.
(3) EFFECT OF VELOCITY								
32	MII/286	No	Ice	2.54	15°-LE	398	408	4.8 cm wide (max.) by 2.2 cm deep segment of leading edge removed.
12	MII/286	Yes	Ice	2.54	15°-LE	411	394	Entire leading edge insert removed. Delamination on back face.
109	Ti-6Al-4V	–	Ice	2.54	15°-LE	402	416	2 cm wide semicircular dent in leading edge.

* Velocity at location of impact 8.89 cm (3.5 inches) from tip.

TABLE XXIV

MAXIMUM IMPACT LOAD AND CONTACT TIME CALCULATIONS FOR
TASK I, PART A, BALLISTIC IMPACTS

Projectile	Diameter (cm)	Velocity (m/sec)	Maximum Impact Load (N x 10³)			Contact Time (μsec)			Bending Damage Observed
			Momentum Impulse	Modified Hertz	Hertz	Momentum Impulse	Modified Hertz	Hertz	
Steel	0.64	61	N.A.	1281	2060	N.A.	23	26	No
	0.64	92	N.A.	N.A.	3340	N.A.	N.A.	24	No
	0.64	122	N.A.	N.A.	4720	N.A.	N.A.	23	No
Steel	1.19	30	N.A.	1053*	3580	N.A.	338	60	No
	1.19	61	N.A.	N.A.	8220	N.A.	N.A.	52	No
	1.19	92	N.A.	N.A.	13400	N.A.	N.A.	48	No
Gelatin	1.27	152	2.47	5.49	7.56	103	74	80	No
	1.27	214	4.31	8.14	11.3	78	70	74	No
	1.27	274	6.89	10.9	15.3	64	70	71	No
Gelatin	2.54	61	1.26	3.82*	9.87	630	506**	195	No
	2.54	107	3.65	7.34*	19.7	378	413+**	174	Yes
	2.54	152	7.21	11.0*	30.2	250	519+**	162	Yes
Ice	1.27	214	4.18	8.12	11.1	76	65	69	No
	1.27	274	6.45	10.9	15.1	62	64	66	No
	1.27	305	7.83	12.3	17.1	58	64	64	No
Ice	2.54	61	1.16	3.92*	9.92	620	439**	177	No
	2.54	107	3.36	7.43*	19.4	372	419***	158	No
	2.54	152	6.94	11.2*	29.8	270	409**	147	Yes

* Maximum load from among two or more discrete impacts.

** Total contact time for two or more impacts; the plus sign indicates projectile still in contact at program termination time = 1800μsec.

TABLE XXV

MAXIMUM IMPACT COMPRESSIVE STRESSES

Projectile	Diameter (cm)	Impact Velocity (m/sec)	Maximum Compressive Stress			Penetration Threshold Achieved
			Inertial (MN/m²)	Cook (MN/m²)	Hertz (MN/m²)	
Steel	0.64	61	N.A.	2040	2540	Yes
	0.64	92	N.A.	N.A.	3000	Yes
	0.64	122	N.A.	N.A.	3360	Yes
Steel	1.19	30	N.A.	1680	1930	Yes
	1.19	61	N.A.	N.A.	2550	Yes
	1.19	92	N.A.	N.A.	3000	Yes
Gelatin	1.27	152	19.5	117	138	No
	1.27	214	34.0	134	152	No
	1.27	274	54.4	148	174	Yes
Gelatin	2.54	61	2.50	65.6	91.7	No
	2.54	107	7.17	81.4	119	No
	2.54	152	14.2	93.1	138	No
Ice	1.27	214	33.0	150	168	No
	1.27	274	50.9	166	185	No
	1.27	305	61.8	173	193	No
Ice	2.54	61	2.28	74.5	101	No
	2.54	107	6.63	92.4	127	No
	2.54	152	13.7	105	146	No

TABLE XXVI

NORMAL VELOCITY COMPONENTS IN TASK II IMPACTS

Projectile	Normal Velocity (m/sec)			Damage Threshold (m/sec)	Penetration Threshold (m/sec)
	15°@274m/sec	15°@400m/sec	30°@274m/sec		
Steel	71	– –	137	<52	<52
Gelatin	71	– –	137	>166	274
Ice	71	108	137	213-226	– –

DISTRIBUTION LIST

Addressee	Number of Copies	Addressee	Number of Copies
1. NASA-Lewis Research Center 21000 Brookpark Rd. Cleveland, OH 44135 Attn: Contract Section B, MS 500-313	1	8. NASA-Flight Research Center P. O. Box 273 Edwards, CA 93523 Attn: Library	1
N.T. Musial, MS-500-113	1	9. NASA-Goddard Space Flight	
Technology Utilization		Center	
Office, MS 3-19	1	Greenbelt, MD 20771	
AFSC Liaison Office, MS 501-3	1	Attn: Library	1
AAMRDL Office, MS 500-317	1		
Library, MS 60-3	2	10. Jet Propulsion Laboratory	
Report Control Office, MS 5-5	1	4800 Oak Grove Dr.	
B. Lubarsky (Dr.), MS 3-3	1	Pasadena, CA 91103	
G. M. Ault, MS 3-5	1	Attn: Library	1
S. S. Manson, MS 49-1	1		
R. H. Kemp, MS 49-3	1	11. Advanced Research Projects	
R. H. Johns, MS 49-3	25	Agency	
N. T. Saunders, MS 105-1	1	Washington, DC 20525	
T. Culko, MS 49-3	1	Attn: Library	1
D. C. Reemsnyder, MS 501-7	1		
C. C. Chamis, MS 49-3	1	12. Air Force Office of Scientific	
R. L. Lark, MS 49-3	1	Research Washington, DC 20333 Attn: Library	1
2. NASA Scientific and Technical Information Facility P. O. Box 33 College Park, MD 20740 Attn: Acquisitions Branch	10	13. Air Force Materials Laboratory Wright-Patterson Air Force Base, OH 45433 Attn: LLC/D. Stuber (Maj.)	1
		MBM/S Tsai (Dr.)	1
3. NASA-Office of Aeronautics and		J. D. Ray (LTN)	1
Space Technology		MBC/T. J. Reinhart	1
Washington, DC 20546		LC/W. J. Schulz	1
Attn: RW/G. C. Deutsch	1	MXE/J.Rhodehamel	1
RWM/J. J. Gangler	1	MBC/G. E. Husman	1
RWS/L. A. Harris (Dr.)	1	LLN/A. Hopkins	
RWS/T. V. Cooney	1	LC/G. P. Peterson	1
RWS/D. A. Gilstad	1	LNE/J. H. Weaver	1
RWS/N. J. Mayer	1		
4. NASA-Langley Research Center Hampton, VA 23365 Attn: Library		14. Air Force Aeronautical Propulsion Laboratory Wright-Patterson Air Force Base, OH 45433 Attn: TBP/T. Norbut	1
		CA/Heiser (Dr.)	1
5. NASA-George C. Marshall		TBP/L. J. Obery	1
Space Flight Center			
Huntsville, AL 35812		15. Air Force Flight Dynamics Laboratory	
Attn: Library	1	Wright-Patterson Air Force Base,	
		OH 45433	
6. NASA-Lyndon B. Johnson		Attn: C. D. Wallace (FBC)	1
Space Center		P. A. Parmley	1
Houston, TX 77001			
Attn: Library	1		
7. NASA-Ames Research Center Moffett Field, CA 94035 Attn: Library	1	16. Defense Metals Information Center Battelle Memorial Institute Columbus Laboratories 505 King Ave. Columbus, OH 43201	1

136

DISTRIBUTION LIST (Cont'd)

Addressee	Number of Copies	Addressee	Number of Copies
17. Department of the Army U.S. Army Material Command Washington, DC 20315 Attn: AMCRD-RC	1	29. National Science Foundation Engineering Division 1800 G St., NW Washington, DC 20540 Attn: Library	1
18. Department of the Army U. S. Army Aviation Materials Laboratory Fort Eustis, VA 23604 Attn: Library	1	30. U. S. Naval Ordnance Laboratory White Oak Silver Spring, MD 20910 Attn: F. R. Barnet	1
19. Department of the Army U. S. Army Aviation Systems Command P. O. Box 209 St. Louis, MO 63166 Attn: Library	1	31. General Dynamics Convair Aerospace Division Ft. Worth Operation P. O. Box 748 Ft. Worth, TX 76101 Attn: C. W. Rogers	1
20. U. S. Army Materials and Mechanics Research Center Watertown Arsenal Watertown, MA 02192 Attn: Library	1	32. General Dynamics Convair Aerospace Division P. O. Box 80847 San Diego, CA 92138 Attn: J. E. Ashton (Dr.)	1
21. Department of the Army Watervliet Arsenal Watervliet, NY 12189 Attn: Library	1	33. Materials Sciences Corp. 1777 Walton Rd. Blue Bell, PA 19422 Attn: B. W. Rosen (Dr.)	1
22. Department of the Army Plastics Technical Evaluation Center Picatinny Arsenal Dover, NJ 07801 Attn: H. E. Pebly, Jr.	1	34. E. I. duPont deNemours and Co., Inc. 1007 Market St. Wilmington, DE 19898 Attn: C. H. Zweben (Dr.) Bldg. 262, Rm. 433	1
23. Department of the Navy Office of Naval Research Washington, DC 20360 Attn: Library	1	35. E. I. duPont deNemours and Co., Inc. Experimental Station Wilmington, DE 19898 Attn: E. A. Merriman (Dr.)	1
24. Director Naval Research Laboratory Washington, DC 20390	1	36. General Technologies Corp. 1821 Michael Faraday Dr. Reston, VA 22070 Attn: R. G. Shaver (Dr.) Vice Pres., Engineering	1
25. Commander Naval Air Systems Command Washington, DC 20360	1	37. McDonnell-Douglas Astronautics Co. 5301 Bolsa Ave. Huntington Beach, CA 92647 Attn: R. W. Seibold, A3-253 L. B. Greszczuk	1 1
26. Commander Naval Ordnance Systems Command Washington, DC 20360	1	38. Union Carbide Corp. Carbon Products Division P. O. Box 6116 Cleveland, OH 44101 Attn: J. C. Bowman, Director Research and Advanced Technology	1
27. Department of the Navy U. S. Naval Ship R&D Laboratory Annapolis, MD 21402 Attn: Library	1		
28. Naval Ship Systems Command Code 03423 Washington, DC 20360 Attn: C. H. Pohler	1		

DISTRIBUTION LIST (Cont'd)

Addressee	Number of Copies
39. Structural Composites Industries, Inc. 6344 North Irwindale Ave. Azusa, CA 91702 Attn: E. E. Morris Vice President	1
40. The Garrett Corp. AiResearch Manufacturing Co. 402 South 36th St. Phoenix, AZ 85034 Attn: J. G. Schnell	1
41. Fiber Science, Inc. 245 East 157th St. Gardena, CA 90248 Attn: L. J. Ashton	1
42. United Aircraft Research Laboratories United Aircraft Corp. East Hartford, CT 06108 Attn: M. DeCrescente (Dr.)	1
43. Hamilton Standard Division United Aircraft Corp. Windsor Locks, CT 06096 Attn: W. Percival	1
44. General Electric Co. Aircraft Engine Group Evendale, OH 45215 Attn: C. A. Steinhagen M. Grandy C. Salemme	1 1 1
45. General Electric Co. Lynn River Works 1000 Western Ave. Mail Drop 34505 Lynn, MA 01910 Attn: F. Erich	1
46. General Electric Co. Corporate Research and Development Center 1 River Rd. Schnectady, NY Attn: S. Levy	1
47. TRW, Inc. 23555 Euclid Ave. Cleveland, OH Attn: W. E. Winters	1
48. Bell Aerospace Division of Textron Buffalo, NY 14240 Attn: Library	1

Addressee	Number of Copies
49. Massachusetts Institute of Technology Department of Civil Engineering Cambridge, MA 02139 Attn: F. J. McGarry (Prof.)	1
50. Illinois Institute of Technology 10 West 32nd St. Chicago, IL 60616 Attn: L. J. Broutman (Prof.)	1
51. Purdue University West Lafayette, IN Attn: C. T. Sun (Prof.)	1
52. Drexel University Philadelphia, PA Attn: P. C. Chou (Prof.)	1
53. Northwestern University Evanston, IL Attn: J. D. Achenbach (Prof.)	1
54. Hercules, Inc. Wilmington, DE 19899 Attn: G. C. Kuebler	1
55. Brooklyn Polytechnic Institute Brooklyn, NY Attn: A. E. Armenakas (Prof.)	1
56. University of Florida Gainesville, FL Attn: G. Nevill (Prof.) R. L. Sierakowski (Prof.)	1 1
57. George Washington University St. Louis, MO 63130 Attn: E. M. Wu (Prof.)	1
58. University of California, Los Angeles School of Engineering and Applied Science Los Angeles, CA 90024 Attn: B. S. Dong (Prof.)	1
59. Grumman Aerospace Corp. S. Oyster Bay Rd. Bethpage, Long Island, NY 11714 Attn: R. N. Hadcock	1
60. North American Aviation Division Rockwell, Inc. International Airport Los Angeles, CA 90009 Attn: L. M. Lockman (Dr.)	1

DISTRIBUTION LIST (Cont'd)

Addressee	Number of Copies
61. Hughes Aircraft Co. Aerospace Group Culver City, CA 90230 Attn: R. W. Jones, (Dr.) Mail Stop D132	1
62. Avco Space Systems Division Lowell Industrial Park Lowell, MA 01851 Attn: T. L. Moore	1
63. Lockheed-Georgia Co. Marietta, GA 30060 Attn: W. G. Juveric	1
64. Goodyear Aerospace Corp. 1210 Massilon Rd. Akron, OH 44315 Attn: G. L. Jeppesen	1
65. Vertol Division The Boeing Co. Philadelphia, PA 19142 Attn: R. A. Pinckney	1
66. Whittaker Corp. Research and Development Center 3540 Aero Ct. San Diego, CA 92123 Attn: R. K. Berg (Dr.)	1
67. Southwest Research Institute 8500 Culebra Rd. San Antonio, TX 78284 Attn: G. C. Grimes	1
68. IITRI 10 West 35th St. Chicago, IL 60616 Attn: I. M. Daniel (Dr.)	1
69. Lawrence Livermore Laboratory University of California P. O. Box 808, L-421 Livermore, CA 94550 Attn: T. T. Chiao	1
70. Boeing Aerospace Co. P. O. Box 3999 Seattle, WA 98124 Attn: J. T. Hoggatt, MS 47-01	1
71. Martin-Marietta Corp. Denver, CO Attn: A. Holston	1
72. Battelle Memorial Institute 505 King Ave. Columbus, OH 43201 Attn: L. E. Hulbert (Dr.)	1

Addressee	Number of Copies
73. Babcock and Wilcox Co. Advanced Composites Department P. O. Box 419 Alliance, OH 44601 Attn: R. C. Young	1
74. National Bureau of Standards Engineering Mechanics Section Washington, DC 20234 Attn: R. Mitchell (Dr.)	1
75. University of Dayton Research Institute Dayton, OH 45409 Attn: F. K. Bogner (Dr.)	1
76. University of Illinois Department of Theoretical and Applied Mechanics Urbana, IL Attn: H. T. Corten (Prof.)	1
77. Detroit Diesel-Allison Division General Motors Corp. Indianapolis, IN Attn: M. Herman (Dr.)	1
78. Sikorsky Aircraft Division United Aircraft Corp. Stratford, CT 06602 Attn: M. Salkind (Dr.)	1
79. Princeton University Department of Aerospace and Mechanical Sciences Forrestal Campus Princeton, NJ 08540 Attn: F. C. Moon (Dr.)	1
80. Aluminum Company of Aermica 1200 Ring Building Washington, DC 20036 Attn: G. B. Barthold	1